



Title	Synthesis, Characterization and Materials Design of Molecule-Incorporated Carbon-Based Materials
Author(s)	謝, 維
Citation	北海道大学. 博士(総合化学) 甲第12034号
Issue Date	2015-09-25
DOI	10.14943/doctoral.k12034
Doc URL	http://hdl.handle.net/2115/59996
Type	theses (doctoral)
File Information	Wei_Xie.pdf



[Instructions for use](#)

**Synthesis, characterization and materials
design of molecule-incorporated
carbon-based materials**



Thesis

Submitted to the Graduate School of Chemical Sciences and Engineering

Hokkaido University

In Fulfillment of the Requirement

For the Degree of Doctor of Chemical Science and Engineering

Xie Wei

July, 2015

Content

Chapter 1. General introduction	1
1.1 Carbon materials	1
1.2 Diamond-like carbon (DLC).....	4
1.3 Carbon doped hexagonal boron nitride nanosheet	6
1.4 Objectives of this study.....	8
1.4.1 The synthesis of novel DLC incorporating molecules	8
1.4.2 Study of carbon doping effects to h-BN by theoretical calculation.....	10
1.5 Outline of this thesis	10
Reference	12
Chapter 2. Diamond-like carbon doped with highly π-conjugated molecules synthesized by plasma assisted CVD	15
2.1 Introduction.....	15
2.2 Experimental details.....	16
2.3 Results and discussion	19
2.3.1 The concentration of the plasma glow	19
2.3.2 UV absorption of the sample.....	21
2.3.3 Raman spectra	25
2.4 Conclusions.....	30
Reference	32
Chapter 3. Colorful carbon nanopopcorns formed by co-depositing C_{60} with diamond-like carbon followed by reaction with water vapor	35
3.1 Introduction.....	35
3.2 Experimental and theoretical details	37

3.2.1 Experimental section.....	37
3.2.2 Calculation details.....	40
3.3 Results and Discussion.....	41
3.3.1 The iridescence color of C ₆₀ -DLC co-deposited film.....	41
3.3.2 Optical characterization	43
3.3.3 Nano structure	49
3.3.4 FTIR and Raman analysis	52
3.3.5 The reaction simulations between C ₆₀ -DLC film and water	58
3.3.6 Thermal stability	61
3.4 Conclusion	62
Reference	63
Chapter 4. Design of carbon-doped hexagonal boron nitride nanosheets by density functional theory	67
4.1 Introduction.....	67
4.2 Calculation details.....	68
4.3 Results and discussions.....	70
4.3.1 Graphene and hexagonal boron nitride monolayers (h-BN)	70
4.3.2 Mono-layer Carbon doped hexagonal BN nanosheet.....	72
4.3.3 Double-layered carbon doped structure	88
4.4 Conclusions.....	106
References.....	108
Chapter 5. Overall summaries and prospect	113

Chapter 1. General introduction

1.1 Carbon materials

Carbon materials, as one of the most potential materials, have been studied for a long time. It has been developed for many applications which are now widely used in our daily life of many different fields. In steel industry, coke, one form of the carbon, is greatly used in the reduction of iron ore. In energy field, graphite is used to control the nuclear reaction in the power plant. In aerospace field, graphite fiber is found as devices in rocket, missile and the other vehicles. In rubber and plastic industry, hydrocarbons from fossil and crude oil are used as important feedstock. Recently, carbon-based semiconductors including organic semiconductors and carbon nanotubes have been developed for electric devices and solar cells, because there is a possibility to tune their band structures to meet the requests from new applications.

The Carbon materials have been developed for applications in many different fields. One of the reasons is the carbon has many kind of allotropes which have different properties. Because of the chemical flexibility to take sp , sp^2 and sp^3 configurations, the carbon is capable to form many different allotropes. Well-known forms of carbon allotropes include diamond, graphite, amorphous carbon, and so on. Even in recent decades, many new allotropes of carbon have still been discovered, such as buckminsterfullerene (carbon nanotube [1-6], carbon nanobuds [7-12]) and graphene [13-18]. Beside of these listed above, there are several other unusual allotropes which are not familiar with the general public, like glassy carbon[19-20], carbide-derived carbon[21-23], carbon nanofoam [24-26], lonsdaleite [27-28]. Some of these well-known allotropes are shown in **Figure 1.1**.

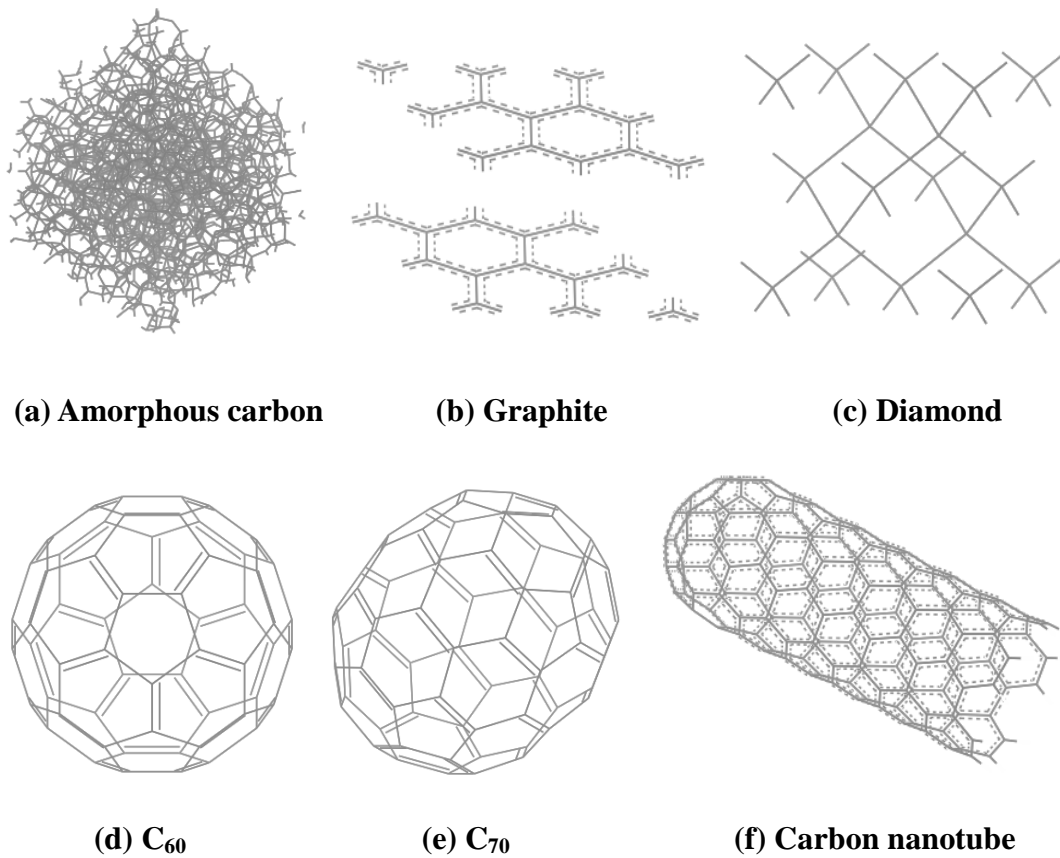


Figure 1.1 Some of the carbon allotropes

As shown in **Figure 1.1**, carbon allotropes have the three hybridization states of carbon atoms (sp , sp^2 and sp^3) with different dimensionality (0D, 1D, 2D, 3D). These allotropes have totally different physical and chemical properties. The one of the most typical example is diamond and graphite. For optical applications, diamond is highly transparent while the graphite is black and opaque. For mechanical applications, diamond is one of the hardest materials while graphite is one of the softest materials. For electrical applications, diamond is an insulator while graphite is a good conductor.

The carbon materials now gather great attentions from the academia and industry due to the various kinds of the carbon allotropes with the properties in a vast

range. The technological development have been driven by the need to create more high-quality products for applications than that can be offered at that time. Recently, a lot of attempts have been made for improving the carbon materials. Functional element doping is the one of the useful methods to adjust the properties of carbon materials. Boron and nitrogen are two of the most common dopants for carbon materials. In diamond, boron [29] and nitrogen [30] atom can greatly improve its electrical properties and this doped diamond can be used as electrodes (different doping materials also can be used to adjust the colors of diamond). In graphene, boron and nitrogen can open a band gap with a certain value. The boron and nitrogen doping carbon nanotubes also have been reported [31]. Metal dopants (Fe[32], Ag[33], Cu[34]) are also good choices for adjusting the properties of these carbon materials. Doping metal into amorphous carbon can greatly change its band structure to improve its electrical properties [32-34]. Metal doped CNT mixtures are used as catalysts for many reactions. Carbon nanotube can be used as an excellent support/based materials in catalyst system because of special distribution of electron density [1-6]. Doping of molecules to carbon materials, however, has not been studied well so far.

The development of synthetic technology is also a nice direction for improving the carbon materials. High Pressure High Temperature (HPHT) processes [35] have been used for diamond synthesis. Chemical vapor deposition (CVD) is also a popular method for diamond synthesis. CVD synthesis methods also can be used for other carbon allotropes synthesis by changing some parameters during the deposition. As one of CVD method, plasma-assisted CVD (PAVCD) [36] or plasma-enhanced CVD (PECVD) [37] is another synthetic technology for carbon materials. The produced plasma can supply various activated radical and free electron which enables the

synthesis to proceed via radical process. Combining with the ion / radical- controlling method, such as electric and magnetic fields, the materials with finely tuned nano-structure can be synthesized in principle. Diamond, graphene / graphite, and carbon nanotubes have been synthesized by using plasma method with radicals-controlled method. Besides the carbon materials synthesis, PACVD and PECVD also are widely used in other materials synthesis such as boron nitride. In my experiment, PACVD was chosen because it might be possible to synthesize well-defined carbon materials as our design.

Carbon source and hydrogen source were also important factors used to adjust structure and properties of carbon materials. CH_4 gas, combined with other secondary gas such as H_2 , Ar, Cl_2 , O_2 , was usually used for synthesizing diamonds with different properties. C_2H_4 or C_2H_2 are the popular choices which are used to synthesize sp^2 -carbon allotropes, like carbon nanotube, graphite, and graphene. However, it is not an absolute choice. It has been reported that carbon nanotube was synthesized by using CH_4 while diamond was synthesized by using C_2H_2 . CH_4 gas will be used in our experiment because it can produce plasma with only CH radical for the carbon source.

1.2 Diamond-like carbon (DLC)

Diamond-like carbon (DLC) is one of the fundamental carbon-based materials. As shown in the **Figure 1.2**, DLC is kind of carbon materials with both sp^2 and sp^3 hybridized carbons. DLC usually formed as amorphous. By combining with hydrogen atoms, it formed some well-known DLC materials, such as a-C:H, ta-C:H. Hydrogen atoms are a very important compositions to affect the features of DLC materials.

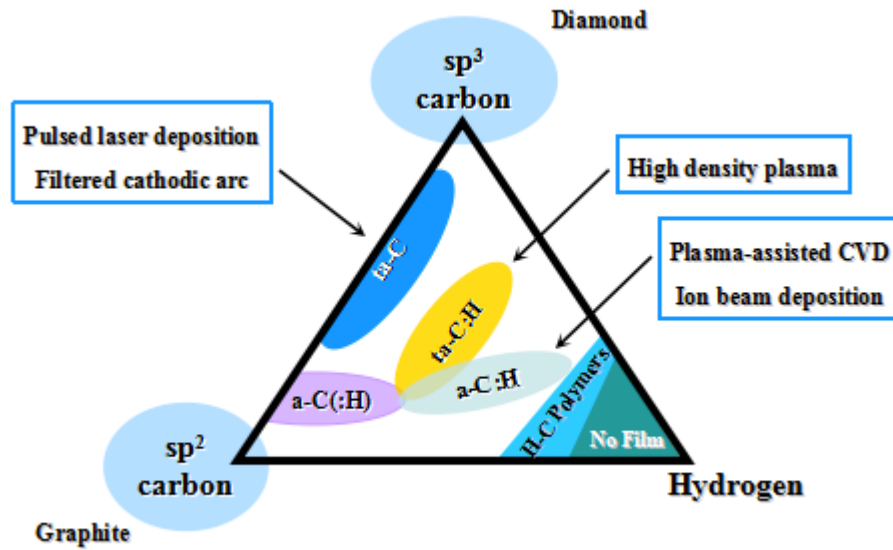


Figure 1.2 The different types of the diamond-like carbon and their synthesis

DLC has many interesting and useful properties [38-40] such as the high electrical resistance, extreme hardness, tribology and chemical robustness. These excellent properties make diamond-like carbon attract great attentions. Based on the properties, wide applications have been developed. The excellent tribology of the DLC can efficiently reduce the abrasive wear, which has lead to a coating film to protect the tools or machines including engines, weapons, drills, and hard-disks. DLC also has the very excellent bio-compatibility. It makes DLC used for medical industry. Implantable human heart pump with DLC coating in the interface of contacting blood can prolong the lifetime of the pump in service. Artificial joints were developed based on excellent physical proprieties and biocompatibility. The unique electronic properties of DLC can also be used in many medical treatment processes. With both sp^2 and sp^3 carbons, DLC has also been studied as a potential semiconductors. Since DLC is amorphous, it will be easier to control the nanostructure in the carbon

networks. If we can finely tune the nanostructure, new properties or features can be expected. I will describe the attempts in that direction by incorporating large organic molecules in DLC in Chapters 2 and 3.

1.3 Carbon doped hexagonal boron nitride nanosheet

Carbon doping into Boron nitride (BN) is another important direction for development of carbon based semiconductor materials with tunable band structures. BN materials, with the isoelectronic composition to carbon, have very similar crystal lattices to the carbon materials. As the carbon material, BN also have several different types based on the different crystalline forms. Firstly, the wurtzite BN (w-BN) is similar to the carbon material of lonsdaleite and w-BN is the hardest BN. Secondly, the sphalerite structure (cubic) boron nitride (c-BN or β -BN) is similar to the diamond. The last, hexagonal/graphitic boron nitride (h-BN or g -BN) is similar to the graphite or graphene, it is the most common and the softest BN material. Based on the different dimensionality from 1D to 3D, BN also can be shaped in the tubular form as carbon nanotubes. These structures are shown in **Figure 1.3**.

Hexagonal-BN also has very interesting properties such as high stability, high thermal conductivity[41]. The most matured application of the h-BN is developed as good lubricant which can be used in many extreme environments, and the fine-grained h-BN particles can be used in cosmetic[42]. Because of the high thermal stability, the h-BN is widely used in high temperature equipment as some parts. It has been proved that the two-dimensional h-BN is an excellent proton conductor[43].

et al.[47] but the detailed structure was not elucidated. Recently atomic arrangement was revealed by TEM observation by Ci [44] and segregation of graphene part and h-BN part in 10 nm scales was concluded. As for the h-CBN nanotubes, the group lead by Y. Bando has made an intensive research activities [48] and found that atomic scale mixing is possible in nanotubes fabricated by plasma-jet growth. The band gap can be narrowed down to ~1 eV from that of insulating BN nanotubes by alloying with carbon. However, the atomic arrangements have not been clarified so far. In the future, PAVCD and PECVD might be used as a possible way to finely tune the atomic compositions in h-CBN materials but it still need to be improved.

1.4 Objectives of this study

1.4.1 The synthesis of novel DLC incorporating molecules

According to the background discussed above, carbon materials still can be improved for a wider applications, based on its diverse nanostructures. As one of the well-known carbon materials, DLC have a many interesting properties. DLC contains both sp^2 and sp^3 carbon and DLC is amorphous. Containing the both sp^2 and sp^3 carbon means that properties of the DLC materials can be adjusted in a wide range from something resembling graphite to that of diamond to meet the any request from the new applications. The synthesis of well-defined nanostructures in DLC will be an important way to improve the properties of DLC. It is expected that the optical and electronic properties of DLC will be controlled if the nanoscale arrangement of sp^2 and sp^3 carbon atoms can be finely tuned in DLC. In this thesis, I would like to propose that incorporating organic semiconductor molecules with extended π -orbitals can be used to make well-defined nanostructures in DLC. I experimentally

examined this possibility by combining thermal deposition of organic semiconductor molecules with PACVD of DLC.

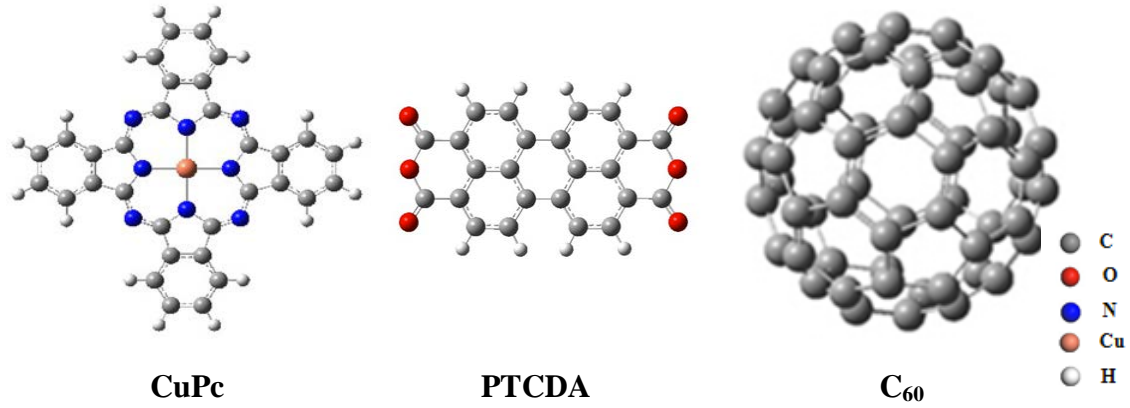


Figure 1.4 The molecular structures of CuPc, PTCDA, and C₆₀

As mentioned above, PACVD method is the advanced technique for synthesizing the DLC film, particular for a-C:H. However, in order to doping large organic semiconductor molecules into the DLC film, the synthesis needs to be improved and adjusted. This is because the plasma glow contains a large number of free electrons and ions which are in activated states. Doping the organic semiconductor molecules in the high energy environment will easily fail because the organic semiconductors are very sensitive to the electronic excitations and it may be decomposed. It was necessary to build a new equipment for PACVD combined with the thermal evaporation of organic semiconductor molecules. Also the plasma condition had to be adjusted. I tried the synthesis of DLC incorporated with three types of molecules: CuPc, PTCDA, and C₆₀ (**Figure 1.4**). The experiments with CuPc and PTCDA are described in Chapter 2, and those with C₆₀ is written in Chapter 3. The incorporation of C₆₀ made a new form of carbon that is named “carbon nano popcorn”.

1.4.2 Study of carbon doping effects to h-BN by theoretical calculation

I planned both of the experimental and theoretical investigations on the h-CBN materials. Experimental studies by finely controlled plasma CVD, which has not been reported by other researchers, is still underway because of the time shortage of PhD study period. In this thesis, I would like to present the theoretical part about how the electronic structures change by incorporating carbon atoms in h-BN. This subject has been studied by some groups in relation with graphene nanoribbons which has a finite bandgaps, but the structure variation in literatures is very limited and only monolayers have been studied. I considered that I can construct various “molecules” embedded in the insulating h-BN, which concept has not been studied in detail. In Chapter 4, I will describe the theoretical investigation of h-CBN systems in view of embedded “molecules”. The distinct difference of this study from previous reports is that double layers have not been calculated before the present work. I found interesting features of charge transfer complex formation and interlayer bonding with sp^3 configurations, as well as the sensitivity of electronic band structures to the structure of the embedded “molecules”.

1.5 Outline of this thesis

This thesis is composed of five chapters. Chapter 1 gives the general introduction about this study. Section 1.1 gives an overview of the properties of carbon materials. Section 1.2 introduced one of the fundamental carbon materials, DLC. The properties, features, and the recent researches of DLC have been

explained in this part. Section 1.3 introduced the feature of boron nitride and the effect of carbon as the dopant with a brief overview of the literature. Section 1.4 describes the motivation and aim of this study. Section 1.5 gives a general outline of our study.

Chapter 2 is focused on the development of the plasma-assisted CVD and the “doping” effect of the organic semiconductors, CuPc and PTCDA into the DLC film. Section 2.1 is the general background of diamond like carbon and the two “doped” molecules. Section 2.2 is the experimental part including the equipment and the experimental procedures. Section 2.3 is the result and discussion parts. Section 2.4 is the summary of this chapter.

Chapter 3 introduced the colorful DLC films formed by co-depositing C₆₀ with DLC which is synthesized by using plasma-assisted CVD. Section 3.1 gives general background of the colorful carbon materials and nanostructures in the DLC. Section 3.2 is the experimental detail parts for the synthesis of C₆₀-incorporated DLC film. Section 3.3 is the result and discussion with the details of analysis of the materials and mechanism. Section 3.4 is the summary of this chapter.

Chapter 4 described the density functional theory study of the hexagonal-CBN nanosheets. Section 4.1 is the introduction of the feature of the h-BN and the doping effect of the carbon. Section 4.2 is the calculation details part which introduced the key parameters of the simulations. Section 4.3 is the result and discussion. Section 4.4 is the summary of this chapter.

Chapter 5 describes the overall conclusion of my study as well as future prospect.

Reference

1. J. Wang, *Electroanalysis*, **2005**, 17, 7;
2. M. Meyyappan, L. Delzeit, A. Cassell, et al., *Plasma Sources Sci. Technol.*, **2003**, 12, 205.
3. L. Bokobza, *Polymer*, **2007**, 48, 4907.
4. E. T Thostenson, Z. Ren, and T. Chou, *Com. Sci. Tech.*, **2001**, 61, 1899.
5. L. Langer, V. Bayot, E. Grivei, et al., *Phys. Rev. Lett.*, **1996**, 76, 479.
6. S. J. Tans, A. R. M. Verschueren, and C. Dekker, *Nature*, **1998**, 393, 49.
7. H. Y. He, and B. C. Pan, *Phys. Chem. C*, **2009**, 113 (49), 20822.
8. M. He, E. Rikkinen, Z. Zhu, et al., *J. Phys. Chem., C*, **2010**, 114, 13540.
9. P. Zhao, P. J. Wang, Z. Zhang, et al., *Phys. B: Cond. Matt.*, **2010**, 405, 2097.
10. A. G. Nasibulin, P. V. Pikhitsa, H. Jiang, et al., *Nature Nanotechnology*, **2007**, 2, 156 .
11. X. Wu and X. C. Zeng, *ACS Nano*, **2008**, 2 , 1459.
12. J. Raula, M. Makowska, J. Lahtinen, et al., *Chem. Mater.*, **2010**, 22, 4347.
13. K. S. Novoselov, A. K. Geim, S. V. Morozov, et al., *Nature*, **2005**, 438, 197.
14. Y. B. Zhang, Y. W. Tan, H. L. Stormer, ea al., *Nature*, **2005**, 438, 201.
15. A. K. Geim, and K. S. Novoselov, *Nature Materials*, **2007**, 6, 183.
16. A. C. Ferrari, J. C. Meyer, V. Scardaci, et al., *Phys. Rev. Lett.*, **2006**, 97, 187401.
17. S. Stankovich, D. A. Dikin, G. H. B. Dommett, et al., *Nature*, **2006**, 442, 282.
18. A. K. Geim, *Science*, **2009**, 324, 1530.
19. F. R. McFeely, S. P. Kowalczyk, L. Ley, et al., *Phys. Rev. B*, **1974**, 9, 5268.
20. R. C. Engstrom, *Anal. Chem.*, **1982**, 54 , 2310.

21. J. Chmiola¹, C. Largeot, P. Taberna, et al., *Science*, **2010**, 328, 480.
22. Y. Gogotsi, A. Nikitin, H. H. Ye, et al., *Nature Materials*, **2003**, 2, 591.
23. Y. Korenblit, M. Rose, E. Kockrick, et al., *ACS Nano*, **2010**, 4, 1337.
24. A. V. Rode, E. G. Gamaly, A. G. Christy, et al, *Phys. Rev. B*, **2004**, 70, 054407.
25. A.V. Rode, R.G. Elliman, E.G. Gamaly, et al., *Applied Surface Science*, **2002**, 197-198, 644.
26. D. Aron, Z. Jagli i , A. Zorko, et al., *Phys. Rev. B*, **2006**, 74, 014438.
27. C. Frondel and U. B. Marvin, *Nature*, **1967**, 214, 587.
28. S. Q. Wang, and H. Q. Ye, *J. Phys.: Condens. Matter*, **2003**, 15, 197.
29. J. Iniesta, P. A. Michaud, M. Panizza, et al., *Electrochimica Acta*, **2001**, 46, 3573.
30. K. Okano, Sa. Koizumi, S. Ravi et al., *Nature*, **1996**, 381, 140.
31. L. J. Yang, S. J. Jiang, Y. Zhao, et al, *Angewandte Chemie*, **2011**, 123, 7270.
32. B. Wang, Y. Zhu, W. Ren, et al, *Phys. Rev. B*, **2007**, 75, 235415.
33. S.C.H. Kwok, W. Zhang, G.J. Wan, et al, *Diamond and Related Materials*, **2007**, 16, 1353.
34. M. Pyun, H. Choi, J. Park, et al., *Appl. Phys. Lett.*, **2008**, 93, 212907.
35. G. Sittas, H. Kanda, I. Kiflawi, et al., *Diamond and Related Materials*, **1996**, 5, 866.
36. T. Michler, M. Grischke, I. Traus, et al., *Diamond and Related Materials*, **1998**, 7, 459.
37. M Meyyappan, L. Delzeit, A. Cassell et al., *plasma Sources Sci. Technol.*, **2003**, 12, 205.
38. J. Robertson, *Surface and Coatings Technology*, **1992**, 50, 185.
39. A. Grill, *Diamond and Related Materials*, **1999**, 8, 428.

40. J. Robertson, Diamond and related materials, **1993**, 2, 984.
41. H. Ishida, S. Rimdusit, Thermochemica Acta, **1998**, 320, 177.
42. C. Sua, H. Tanga, G. Zhub, et al., Ceramics International, **2014**, 40, 4691.
43. H. F. Ma, T. Brugger, S. Berner, ChemPhysChem, **2010**, 11, 399.
44. L. J. Ci, L. Song, C. H. Jin, et al., Nature materials, **2010**, 9, 430.
45. T. Morishita, H. Okamoto, Y. Katagiri, Chem. Commun., **2015**, 51, 12068.
46. A. K. Geim, and K. S. Novoselov, Nature materials, **2007**, 6, 183.
47. M. Kawaguchi, T. Kawashima. T, Nakajima, Chem. Mater., **1996**, 8, 1197.
48. D. Golberg, Y. Bando, C. Tang, and C. Zhi, Advanced Materials, **2007**, 19, 2413.

Chapter 2. Diamond-like carbon incorporated with highly π -conjugated molecules synthesized by plasma assisted CVD

2.1 Introduction

As I introduced in chapter 1, plasma processes have been developed greatly for various materials synthesis and treatment, particularly for carbon-based materials. The plasma process supplied novel routes for production of new carbon materials. Because of the high melting point and insolubility of solid carbon-based materials, it is impossible to synthesize those materials from liquid or solution in ambient conditions. We have to use other methods such as high temperature high pressure (HTHP) or vapor -based methods (catalytic CVD for carbon nanotubes or graphene and plasma CVD for diamond-like carbon (DLC)). Recently, by using plasma method, several solid carbons have been successfully synthesized. Nano diamond films have been synthesized by plasma methods with different carbon source(CH_4/H_2 , CH_4/N_2 , alcohol/water vapor, and $\text{CH}_4/\text{H}_2/\text{CO}_2$) [1-9]. Single wall carbon nanotubes have been synthesized also by plasma-assisted CVD (PACVD) [10-11]. In the work described in this chapter, I intended to explore a new possibility of carbon-based solids, i.e. molecule-doped DLCs, by using the PACVD.

DLC, as one of the most important carbon-based materials, has been studied for many applications such as coating for optical, anti-abrasive, anti-corrosion and gas barrier properties [12-13]. All of these applications come from the excellent properties of DLC in tribology [14-18], optics [12, 19-20], electronics and electrochemistry [5, 6,

21-23], catalysis [24-26], and biological functions [27-28]. DLC can be synthesized by using the plasma CVD with hydrocarbon gas such as methane [14-15], ethylene [15], which are used as carbon and hydrogen sources. Plasma method supplies a simple way for coating process, which leads to large scale industrial applications.

DLC is composed of carbon and hydrogen with various ratios. The configuration of carbon also has flexibility in the ratio of sp^2/sp^3 carbon. Nano-structure also greatly affects the properties of DLC [12-13]. However only recently the microscopic structures has drawn attention and was characterized because of the request in the new applications, but the precise synthesis of the nanostructure in DLC had not yet been established.

In this chapter, I have studied the synthesis of nano-structures in DLC materials by using plasma process. I studied the co-deposition of large organic semiconductor molecules with extend π -electron systems during the fabrication of the DLC films using PACVD. The organic semiconductor molecules are copper phthalocyanine (CuPc, $C_{32}H_{16}N_8Cu$) and perylenetetecarboxylicdianhydride (PTCDA, $C_{24}H_8O_6$). My focus is in the reaction between extended π -electron systems of organic semiconductor molecules with the plasma [29]. Both PTCDA and CuPc are known as robust dye molecules. Recently they have received great attentions as organic semiconductors. The optical properties and Raman spectra of co-deposited DLC films were studied.

2.2 Experimental details

In the present experiment, a special arrangement was used for the plasma deposition in order to incorporate the large organic semiconductor molecules into the

DLC film without excessive decomposition. **Figure 2.1** exhibits the schematic drawing of the equipment used in the experiment. In the deposition chamber, a radio-frequency (RF) sputter gun equipped with a carbon target was set and used as the plasma source. A gas inlet was on the top of the chamber where the methane gas, which is used as the primary carbon and hydrogen source, was introduced into the chamber with the flow rate of 30 sccm. A pumping line with a bypass valve is connected between the gas inlet and vacuum pump. The sample holder is made of stainless steel and it was floated at -400 V from the ground level in order to attract the positive ions and synthesize sp^3 -carbon-rich DLC film [30]. The positive voltage will lead to the increase of sp^2 ratio in DLC while it would be full- sp^3 DLC materials with minus voltage [30].

Al_2O_3 (0001) was used as the substrate for our experiment with size of $5 \times 5 \times 0.43$ mm³. Before the deposition, the chamber was pumped down to the 10^{-4} Pa by using turbo molecular pump (TMP), and then, by adjusting the main valve, the pumping rate was reduced. By controlling the flow rate of methane gas introduced into chamber, the pressure of methane gas in the chamber was kept at 10 Pa, which is used as the deposition pressure. A Knudsen-cell (molecular evaporation source) was arranged just below the sample holder. The organic semiconductor molecules were put in the Knudsen-cell and were heated at appropriate temperatures. After the bias voltage (-400V) was applied to the substrate, the plasma was ignited for the deposition of DLC. The sample current was monitored and it was typically 1 mA during the deposition.

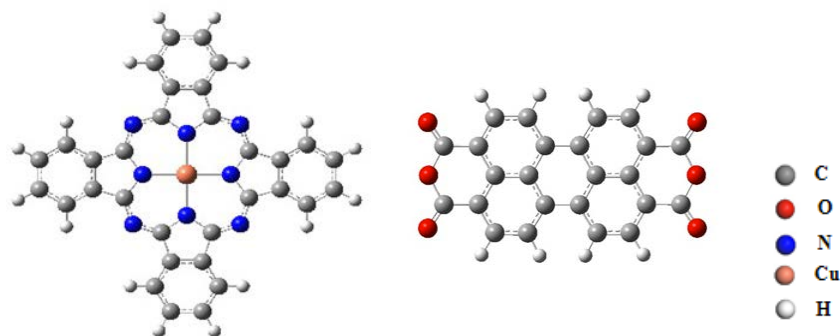
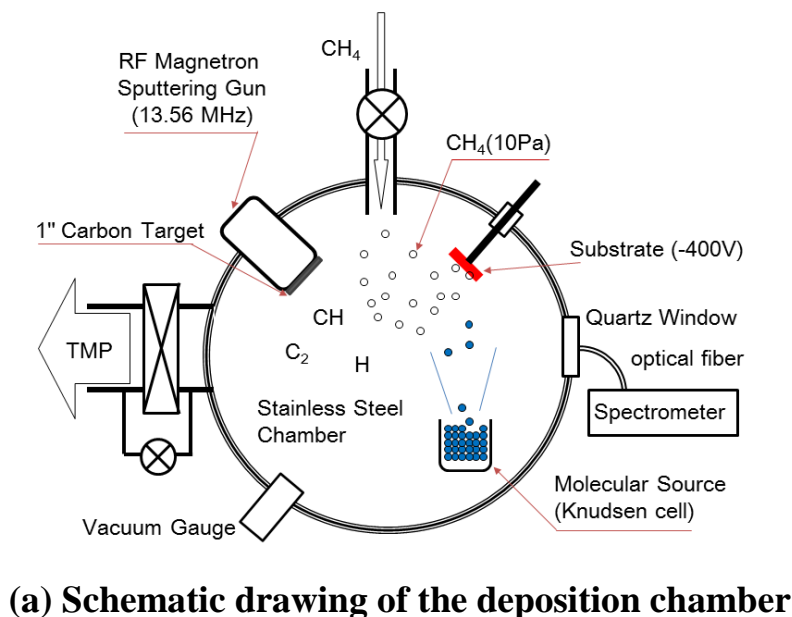


Figure 2.1 (a) Schematic drawing of the deposition chamber using plasma-assisted CVD equipped with the molecular source. Plasma glow was produced by a radio frequency magnetron sputtering gun with a graphitic carbon target. The sputtering gun was set not facing the substrate to avoid direct deposition of sputtered carbon and damage to the DLC film or the molecule source from the plasma ions. Methane was supplied as the plasma gas and primary C and H source. Organic semiconductor molecules were evaporated from a Knudsen cell facing the substrate. (b) The molecular structure of CuPc and PTCDA.

The produced plasma glow has a small size with a diameter of 5cm. The

plasma glow neither directly touches the substrate nor the organic molecules source as observed visually. After the plasma glow and the sample current had become stable, the molecular source was heated to a proper temperature which would not break their π -electron systems. (~ 250 °C to CuPc and ~ 200 °C to PTCDA) These organic molecules were doped with $\sim 10\%$ in DLC at these heating temperatures, as estimated from the deposition rate monitored by quartz crystal microbalance. In this experiment, the substrate temperature was not controlled. The substrate temperature slightly increased because of the attacking of plasma ion to the substrate. But the temperature did not exceed 60 °C during the deposition.

The optical emission spectra of the plasma were monitored by a fiber coupled spectrometer (Ocean Optics USB2000). Optical absorption spectra (Lambda 900, Lambda Physics) and Raman spectra (InVia, Renishaw, 20x \sim 50x objective lens and 532 or 785 nm excitation) were employed for characterization of the properties and the structure, respectively.

2.3 Results and discussions

2.3.1 The concentration of the plasma glow

First, I analyzed the composition of plasma glow by using optical emission spectra (OES). **Figure 2.2** exhibits the OES profiles of the plasma glow during the DLC deposition. Based on the spectra, I can observe four main peaks which were assigned for the emission components of CH ($A^2\Delta \rightarrow X^2\Pi$ at 430.7 nm, $B^2\Sigma \rightarrow X^2\Pi$ at 390.3 nm), H_α (657 nm) and H_β (486 nm) [31-34], respectively. The energy level transitions, extinction process and threshold energies of these plasma radicals species have listed in **Table 2.1**.

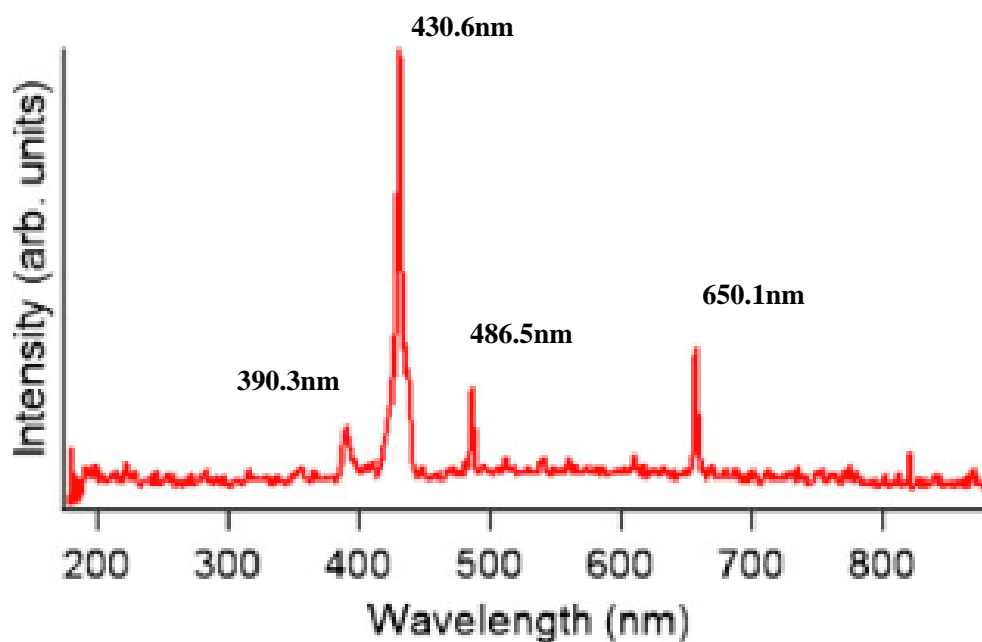


Figure 2.2 Optical emission spectrum during the deposition of pristine DLC using the present setup. The spectra with co-evaporation of CuPc or PTCDA were almost identical to the spectrum in this figure.

Table 2.1 Emission species in a C-H plasma produce with CH₄ gas [31-34]

Species	Wavelength (nm)	Energy level transitions	Extinction process	Threshold energies (eV)
CH	390.3	$B^2\Sigma \rightarrow X^2\Pi$	$CH+e^- \rightarrow CH^*+H_2+H+e^-$	13.4
CH	430.6	$A^2\Delta \rightarrow X^2\Pi$	$CH+e^- \rightarrow CH^*+H_2+H+e^-$	21.9
H _{α}	657.1	$3d^2D \rightarrow 2p^2P^0$	$CH_4+e^- \rightarrow CH_3+H^*+e^-$	17.25
H _{β}	486.5	$4d^2D \rightarrow 2p^2P^0$	$H_2+e^- \rightarrow H+H^*+e^-$	13.06

The plasma glow I used to deposit the DLC film contained mainly CH radical and H radical which are produced from CH₄ gas. Although the C₂ emission can be observed at the position of 516 nm, it is very weak which means the chemical

components in our plasma are governed by hydrogen-containing species which can be classified to typical C-H plasma. The carbon in the CH_4 gas is sp^3 carbon formed four σ bonds with four hydrogen atoms, which means the dissociation of CH_4 occurs from the cleavage of the CH bonds. This kind of dissociation leads to only CH radical and H radical. However in C_2 species gas (C_2H_2 , C_2H_4 [35]), it will produce a larger amounts of C-C radical in the plasma glow. Even being co-deposited with organic semiconductors molecules, the OES profiles did not have a significant change, which indicated that the concentration of the organic semiconductors molecules was very low. There would be no direct reaction among the heated semiconductor molecules. It also can be used to confirm that our plasma glow did not directly touch the Knudsen-cell (molecular source) to cause radical reactions during the deposition.

2.3.2 UV absorption of the sample

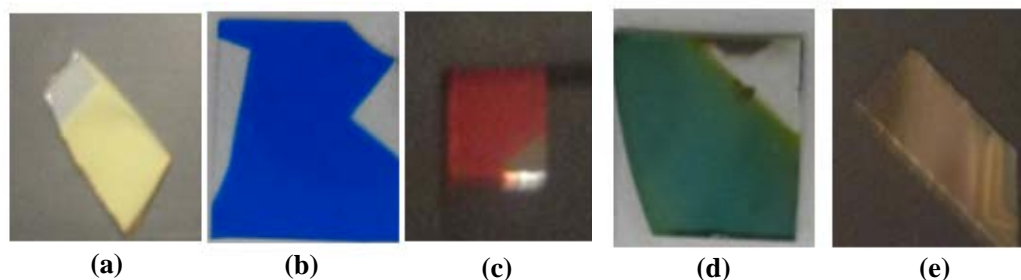


Figure 2.3 The pictures of the films. (a) Pristine DLC film, (b) Pristine CuPc film (c) Pristine PTCDA film. (d) CuPc-DLC film (e) a PTCDA-DLC co-deposited film.

After the deposition, all the fabricated samples have different colors from the doping materials as shown in **Figure 2.3** (Pristine CuPc film is blue and the pristine PTCDA film is red). UV-Vis optical absorption spectra were measured for characterization.

2.3.2.1 UV-Vis absorption spectrum of CuPc

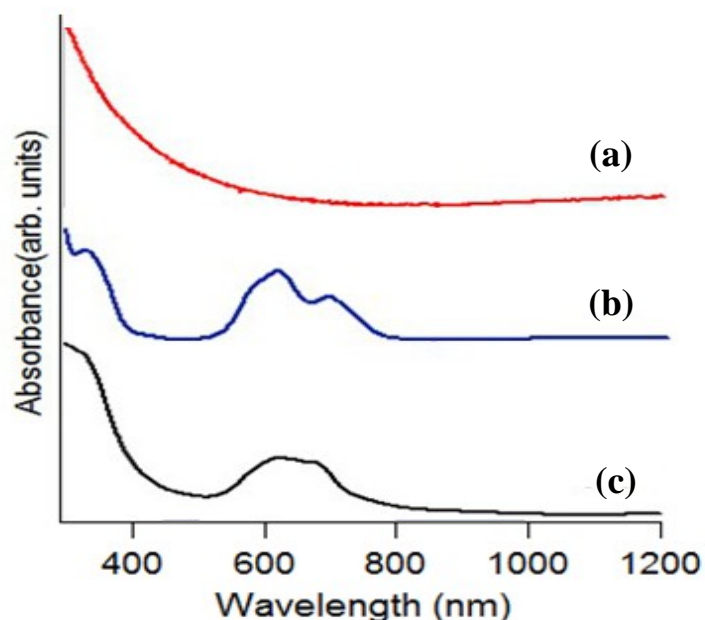


Figure 2.4 Optical absorption spectra of (a) a pristine DLC film, (b) a pristine CuPc film, and (c) CuPc-DLC film. The splitting in (b) comes from the Davydov splitting, which is caused by the interaction between optically excited molecules.

I first discuss the CuPc incorporation case. **Figure 2.4** shows the optical absorption spectra of (a) a pristine DLC film, (b) a DLC with a co-deposited CuPc film, and (c) a pristine CuPc film. The curve (a) of a pristine DLC film has a very smooth increase in the optical absorption spectra beginning at 500 nm, which reflected the amorphous nature of the materials with wide distribution of local HOMO-LUMO gaps. The curve (b) in **Figure 2.4** stands for the pristine CuPc film. Here, several absorption peaks can be observed which distributed in two ranges of the wavelength. A Soret band located at around 350 nm and a Q-band located at around

650 nm with significant Davydov splitting can be clearly observed in the Figure as reported [36].

Davydov splitting exist in the electronic spectra of crystal due to presence of more than one (interacting) equivalent molecular entity in the unit cell. In some kinds of molecules, such as CuPc [37], AlClPc/GaClPc [38] and the other organics[39-40], two or more monomers combined together to form a virtual dimer, especially in the excited states. The two monomers electronic orbitals (in this case excited states) combined and form a new orbital which contains the bonding orbital and anti-bonding orbital that are located at lower energy level and higher energy level, respectively. The energy level changes of molecular orbital directly affect the shift of the absorption peaks in in the electronic spectra (**Figure 2.5**).

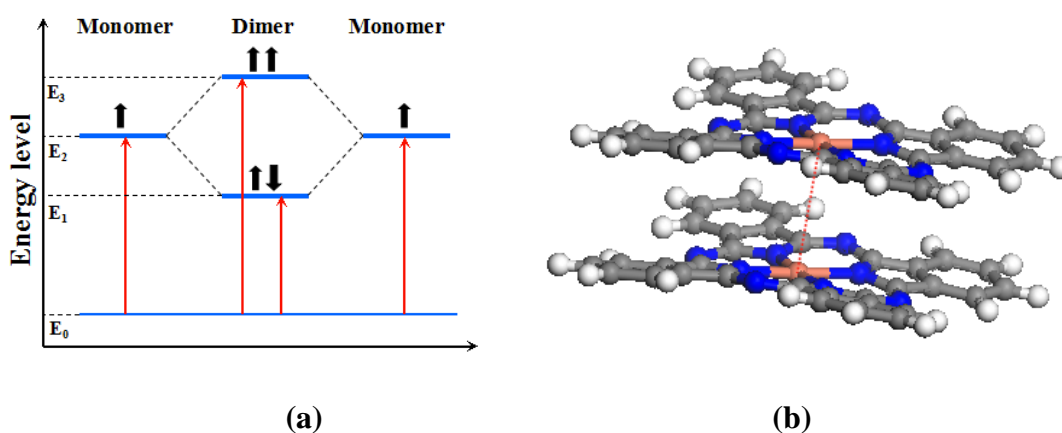


Figure 2.5 Davydov splitting (a) Transformation of energy level from monomer to dimer (b) One type of CuPc dimer [37]

The curve (c) in the **Figure 2.4** is the co-deposited film (CuPc-DLC film). I can see also two absorption peaks exist which also located same wavelength area to the curves (b). The similar optical absorption located in the same absorption areas

between pristine film (b) and the CuPc-DLC co-deposited film (c) suggests that the dopant of CuPc molecules have not been decomposed during the co-deposition. The Davydov splitting also can be confirmed in the co-deposited film but it became weak. Because Davydov splitting comes from the interaction between two equivalent molecules to form dimer in the excited states. The splitting width is determined by the geometry of two molecules. If the CuPc molecules are separately embedded in the matrix, they will show a single peak in optical absorption spectra. The less splitting of Q-band absorption shown in **Figure 2.4** (c) can be explained by this isolation effect or might-be partially decomposed CuPc. After co-deposition with

2.3.2.2 UV-Vis absorption spectrum of PTCDA

Perylenetetracarboxylicdianhydride (PTCDA) is also one of the well-known robust dye molecules. It shows a marked red color as in Figure 2.3 (c) . The optical absorption spectra of the samples are shown in **Figure 2.6**. Curve (a) is that of the pristine DLC film which is the same as the **Figure 2.4(a)**, (b) is that of the pristine PTCDA film, and (c) is that of the PTCDA-DLC co-deposited film.

By comparing curve (b) with (c) in the optical spectrum, we can find substantial difference, which indicates that the π -electron system in PTCDA have been substantially altered in the co-deposited film. It means that the PTCDA molecules have been decomposed with C-H plasma during the deposition. Nevertheless, it is not that PTCDA molecules were totally decomposed to atoms and made ordinary DLC, because the curves in **Figure 2.6** (a) and (c) are different. But it is hard to identify the structure of the fragments of PTCDA only based on these optical absorption spectra.

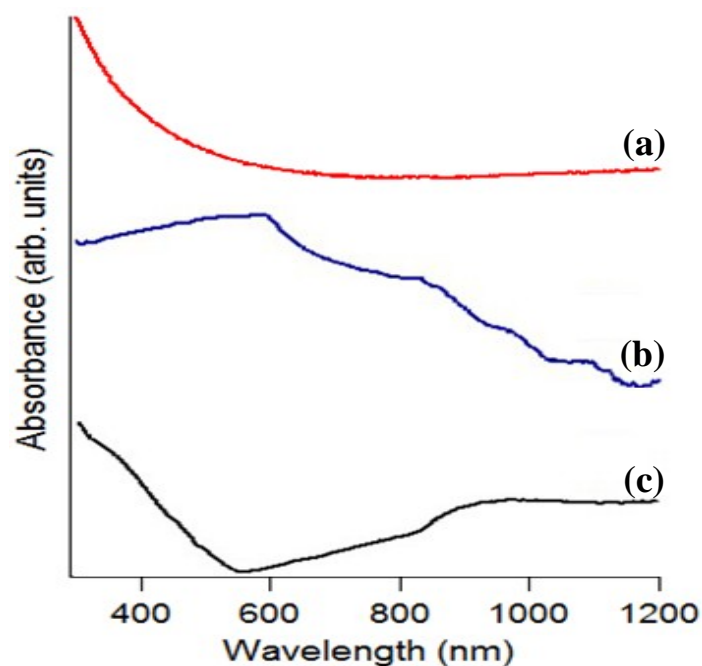


Figure 2.6 Optical absorption spectra of (a) pristine DLC film (same as **Figure 2.4** (a)), (b) pristine PTCDA film, and (c) PTCDA-DLC co-deposited film.

2.3.3 Raman spectra

2.3.3.1 Typical diamond-like carbon Raman spectrum

The analysis of optical absorption spectra proves that the co-deposited molecules have been intact (CuPc case) or have partly decomposed (PTCDA) during the deposition. I used Raman spectra to distinguish the decomposed bonds from the preserved bonds of these doping molecules. Firstly, pristine DLC film was characterized. The Raman spectra of the DLC were shown in **Figure 2.7** below.

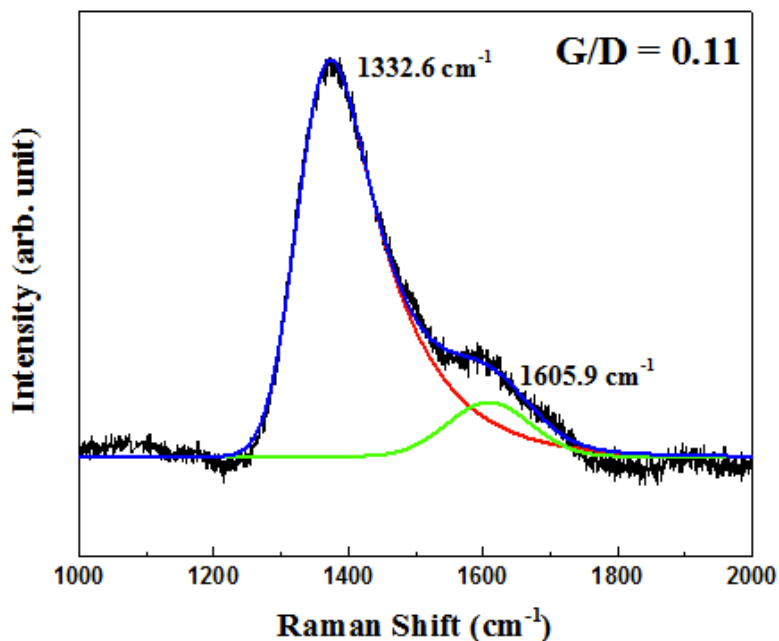


Figure 2.7 Raman spectra of the pristine DLC film. Black line is the raw data of DLC’s Raman spectra. Green line and red line are the G peak and D peak after Gaussian fitting, respectively.

A broad peak in the range from 1200cm^{-1} to the 1800cm^{-1} is assigned to typical DLC peak. This broad peak is due to characteristic structure of DLC. DLC is kind of carbon-based materials with sp^2 and sp^3 carbon. The two different C-C bonds vibrations lead to two different peaks which make one broad peak. After Gaussian fitting, this broad peak was separated into D and G peaks, they stand for the two different types carbon bonds vibrations which exist in the DLC. G peaks stand for the sp^2 carbon of π -bonds vibrations with the center of 1605.9 cm^{-1} while the D peak stands for the rest carbon bonds. By comparing the area of these two peaks, the small ratio of G/D with the value of 0.11 means our samples is sp^3 -rich carbon DLC. This is because of the effect from the minus voltage I biased on the substrate during the deposition. Adjusting the bias voltage can greatly affect the composition of DLC [29].

By using positive voltage, the synthesized DLC will obtain a large ratio of G/D with sp^2 -rich carbon, while the DLC will be sp^3 -rich by using negative voltage. This sp^3 -rich carbon DLC was used as the materials for co-deposited with PTCDA and CuPc organic semiconductors.

2.3.3.2 Raman spectra of CuPc

In the optical absorption spectra of CuPc (Section 2.3.2.1), I discussed the Davydov splitting which existed in the pristine CuPc film and explained that the less splitting observed in the CuPc-DLC co-deposited film may be due to the isolation effect. However, there is also a possibility that it comes from the structure partly destroyed of CuPc. In order to examine the possibilities, Raman spectra were employed to characterize the chemical bonds in the DLC film. The results of the Raman spectra for the several samples are shown in **Figure 2.8**.

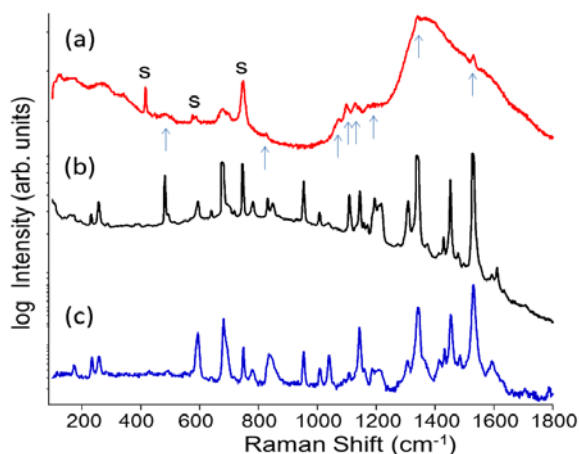


Figure 2.8 Raman spectra of (a) CuPc-DLC co-deposited film, (b) CuPc single crystal, and (c) pristine CuPc film fabricated by vacuum deposition. “s” in (a) denotes the signal from the substrate. The difference between (b) and (c) comes from the difference in the polytype of CuPc crystals.

I characterized three types of the CuPc-related samples, (a) the CuPc-DLC co-deposited film, (b) CuPc single crystal and (c) the pristine CuPc film fabricated by vacuum deposition. In the curve (a) of the **Figure 2.8**, a broad peak located at the range from 1000cm^{-1} to 1800cm^{-1} is the one typically observed in DLC. The center of the broad peak is located at approximately 1390cm^{-1} , which means that the formation of the co-deposited film is sp^3 -rich DLC (The same to the pristine DLC film). Furthermore, the D peak center shifts from 1330cm^{-1} to the 1390cm^{-1} , which indicates that the amount of sp^2 carbon in DLC slightly increased. This is because of effect from dopants CuPc which have the π -electron structure. Raman spectra of CuPc depend on the crystal structure polytypes. **Figures 2.8 (b) and (c)** shows Raman spectra of a deposited film and a needle-shaped single crystal, which are identified as typical polytypes of β -type (b) and α -type (c) [41]. In the curve (a) in **Figure 2.8**, the molecular fingerprint of CuPc can be identified as marked by the blue arrows. This is because that the vibrational structure of the extended π -conjugated molecules was not decomposed during the deposition. However some of the peaks broadened and shifted. This might indicate a minor change of the molecular structure, for example, dimer formation or peripheral hydrogen replacing by CH_3 radicals. In addition, there might be another reaction connecting CuPc to the DLC carbon network. These minor structure changes also can lead to the less Davydov splitting of the optical absorption Q-band shown in **Figure 2.4**.

2.3.3.3 Raman spectra of PTCDA

I discussed PTCDA molecules co-deposited into DLC film by using optical absorption spectra. The main π -electron structure has been decomposed during the

co-deposition, but I considered that there still have some fragments of the PTCDA left in co-deposited films. Raman spectra were employed to characterize the chemical bonds left in the films.

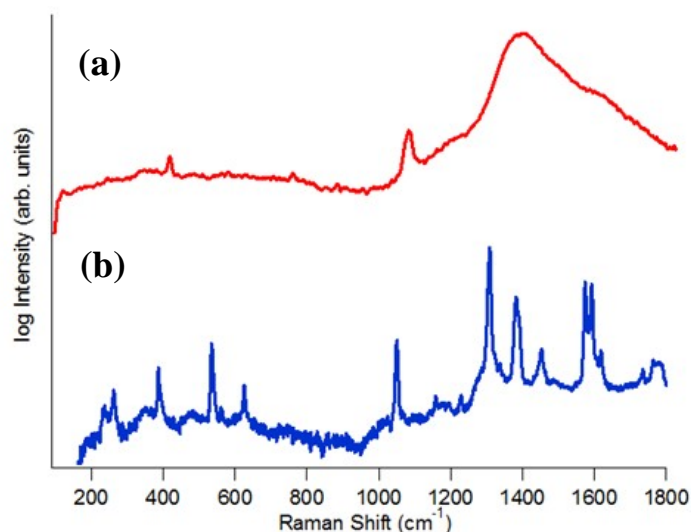


Figure 2.9 Raman spectra of (a) PTCDA-DLC co-deposited film and (b) pristine PTCDA film. The peak at 1080 cm^{-1} in (a) is considered to be of the same origin as the peak at 1060 cm^{-1} in (b), which is identified as C-O-C vibration. The peak at 420 cm^{-1} in (a) is the signal from the substrate.

Figure 2.9 exhibits the result of Raman spectra. **Figure 2.9(a)** is a Raman spectra PTCDA-DLC co-deposited film and the **(b)** is a pristine PTCDA film. A broad peak located in the range from 1200 cm^{-1} to 1800 cm^{-1} also indicated that the our co-deposited film is sp^3 -rich carbon materials. However, the ratio of sp^2/sp^3 in PTCDA-DLC co-deposited film slightly increased from the CuPc-DLC co-deposited film and the pristine DLC film because the main DLC peak shifted to a higher wave numbers. In the **Figure 2.9(a)**, one sharp peak can also be identified at the location of around 1080 nm , which does not belong to the DLC peaks. By comparing with the

Figure 2.9(b) of pristine PTCDA film, PTCDA also have a strong and sharp peak at around 1080 nm. By using quantum chemical computation with density functional theory method and comparing with reported PTCDA studies, this peak is assigned to the in-plane C-O-C bending vibration [42]. These analyses strongly suggest that C-O-C fragment survived during the co-deposition that means the C-O-C bonds did not react with C-H plasma. It is reasonable to consider that the decomposed main π -electron structure of PTCDA leads to the higher sp^2/sp^3 ratio than CuPc-DLC co-deposited film and pristine DLC film.

2.4 Conclusions

In this chapter, I studied the modification of DLC by co-depositing large organic molecules. Two of the organic semiconductor molecules, CuPc and PTCDA were used as “doping” materials for this experiment. I successfully synthesized novel carbon films by using plasma-assisted chemical vapor deposition (PACVD). First, the OES was employed to characterize the plasma I used for the experiment. The result of OES shows that C-H radical plasma was formed in the process which is the typical CH_4 gas plasma for DLC deposition. The co-deposited π -electron molecules did not change the composition of the plasma. Raman spectra show that our DLC film was composed of mostly sp^3 carbon. By incorporating π -electron molecules, the ratio of sp^2/sp^3 was slightly increased and it depended on the different types of dopant molecules. In the case of CuPc, the co-deposited film showed an optical absorption profile similar to the pristine molecular film, but still, minor changes were observed. However, in PTCDA case, a substantial destruction of the π -electron structure has been observed in the optical absorption spectra and Raman spectra results. Further

analysis based on the Raman spectrum, the carboxylic dianhydride (C-O-C) moiety remains intact during the plasma process in PTCDA-DLC co-deposited film.

Reference

1. F. Oshima, S. Staus, C. Ishii, D. Z. Pai and K. Terashima, *J. Phys. D*, **2012**, 45, 402003.
2. S. Stauss, H. Miyazoe, T. Shizuno, K. Saito, T. Sasaki and K. Terashima, *Jpn. J. Appl. Phys.*, **2010**, 49, 070213.
3. H. Kikuchi, S. Stauss, S. Nakahara, F. Matsubara, T. Tomai, T. Sasaki and K. Terashima, *J. Supercrit. Fluids*, **2010**, 55, 325.
4. C. Donnet, *Surf. Coating Tech.*, **1998**, 100-101, 180.
5. A. Sikora, A. Berkesse, O. Bourgeois, J. L. Garden, C. Guerret-piécourt, J. N. Rouzaud, A. S. Loir, F. Garrelie, and C. Donnet, *Solid State Sci.*, **2009**, 11, 1738.
6. B. Khadro, A. Sikora, A. S. Loir, A. Errachid, F. Garrelie, C. Donnet, and N. Jaffrezic-Renault, *Sens. Actuators B*, **2011**, 155, 120.
7. T. Ito, K. Katahira, Y. Shimizu, T. Sasaki, N. Koshizaki, and K. Terashima, *J. Mater. Chem.*, **2004**, 14, 1513.
8. R. A. Rudder, G. C. Hudson, J. B. Posthill, R. E. Thomas, R. C. Hendry, D. P. Malta, and R. J. Markunas, *Appl. Phys. Lett.*, **1992**, 60, 329.
9. J. Liskova, O. Babchenko, M. Varga, A. Kromka, D. Hadraba, Z. Svindrych, Z. Burdikova, and L. Bacakova, *Int J Nanomedicine*, **2015**, 10, 869.
10. G. F. Zhong, T. Iwasaki, and H. Kawarada, *Carbon*, **2006**, 44, 2009.
11. G. F. Zhong, T. Iwasaki, J. Robertson, and H. Kawarada, *J. Phys. Chem. B*, **2007**, 111, 1907.
12. A. Grill, *Diamond Relat. Mater.*, **1999**, 8, 428.
13. J. Robertson, *Mater. Sci. Eng. R*, **2002**, 37, 129.

14. A. A. Al-Azizi, O. Eryilmaz, A. Erdemir and S. H. Kim Langmuir, **2015**, 31, 1711.
15. A. Erdemir, O.L. Eryilmaz, I.B. Nilufer and G.R. Fenske, Diamond and Related Materials, **2000**, 9, 632.
16. A. Erdemir and C. Donnet, J. Phys. D, **2006**, 39, R311.
17. S. V. Hainsworth and N. J. Uhure, Int. Mater. Rev., **2007**, 52, 153.
18. A. R. Konicek, C. Jaye, M. A. Hamilton, W. G. Sawyer, D. A. Fischer, and R. W. Carpick, Tribology Lett., **2011**, 44, 99.
19. R. Intartaglia, K. Bagga, A. Genovese, A. Athanassiou, R. Cingolani, A. Diaspro, and F. Brandi, Phys. Chem. Chem. Phys., **2012**, 14, 15406.
20. M. Chhowalla, J. Robertson, C. W. Chen, S. R. P. Silva, C. A. Davis, G. A. J. Amaratunga, and W. I. Milne, J. Appl. Phys., **1997**, 81, 139.
21. M. Grischke, K. Bewilogua, K. Trojan, and H. Dimigen, Surf. Coatings Technol., **1995**, 739, 74.
22. K. S. Yoo, B. Miller, R. Kalish, and X. Shi, Electrochem. Solid-State Lett., **1999**, 2, 233.
23. A. Zeng, E. Liu, S. Zhang, S. N. Tan, L. X. Liu, and J. Gao, Mater. Sci. Forum, **2003**, 467, 437.
24. D. Su, N. I. Maksimova, G. Mestl, et al., Carbon, **2007**, 45, 2145.
25. N. Keller, N. I. Maksimova, V. V. Roddatis, et al., Angew. Chem., Int. Ed. Engl., **2002**, 41, 1885.
26. X. Liu, B. Frank, W. Zhang, T. P. Cotter, R. Schlogl, and D. S. Su, Angew. Chem., Int. Ed. Engl., **2011**, 50, 3318.
27. P. K. Chu, Nucl. Instrum. Methods Phys. Res., Sect. B, **2006**, 242, 1.

28. T. Saito, T. Hasebe, S. Yohena, Y. Matsuoka, A. Kamijo, K. Takahashi, and T. Suzuki, *Diamond Relat. Mater.*, **2005**, 14, 1116.
29. S. Chowdhury, M.T. Laugier, I.Z. Rahman, *Thin Solid Films*, **2004**, 468, 149.
30. T. Shimada, N. Muraya, J. Tomita, T. Yanase, and T. Nagahama, *J. Phys.: Conf. Ser.*, **2013**, 441, 012041.
31. A. Pastol and Y. Catherine, *J. Phys. D*, **1990**, 23, 799.
32. M. M. Larijani, F. Le Normand, and O. Crégut, *Appl. Surf. Sci.*, **2007**, 253, 4051.
33. K. Hanada, T. Nishiyama, T. Yoshitake, and K. Nagayama, *Diamond Relat. Mater.*, **2010**, 19, 899.
34. J. C. Richley, M. W. Kelly, M. N. Ashfold, and Y. A. Mankelevich, *J. Phys. Chem. A*, **2012**, 116, 9447.
35. A Granier, M Vervloet, K Aumaille and C Vallée, *Plasma Sources Sci. Technol.*, **2003**, 12, 89.
36. A. A. M. Farag, *Opt. Laser Technol.*, **2007**, 39, 728.
37. A. Rosa , E. J. Baerends, *Inorg. Chem.*, **1992**, 31, 4717.
38. A. Zawadzka, A. Karakas, P. P óciennik, J. Szatkowski, Z. ukasiak, A. Kapceoglu, Y. Ceylan, B. Sahraoui, *Dyes and Pigments*, **2015**, 112, 116.
39. W. S. Durfee , W. Storck , F. Willig , M. Von Frieling, *J. Am. Chem. Soc.*, **1987**, 109, 1297.
40. C. G. Heid, P. Ottiger, R. Leist, and S. Leutwyler, *J. Chem. Phys.*, **2011**, 135, 154311.
41. J. H. Sharp and M. Lardon, *J. Phys. Chem.*, **1968**, 72, 3230.
42. A. Y. Kobitski, R. Scholz, and D. R. T. Zahn, *J. Mol. Struct.: Theochem*, **2003**, 625, 39.

Chapter 3. Colorful carbon nanopopcorns formed by co-depositing C₆₀ with diamond-like carbon followed by reaction with water vapor

3.1 Introduction

Nanostructured carbon materials show many interesting properties especially in optics. Their synthesis is eagerly pursued from various routes [1-10]. Recently, optical carbon materials have gathered much attentions because of the increasing requirements from applications and emerging field of metamaterials [5-14]. However, up to now, only carbon nanotube ensembles has been reported to possess unique optical properties in the visible region. The carbon nanotube forest shows iridescence color. The properties are due to the high degree of orientation and self-organized periodicity of carbon nanotubes forests [15]. However, highly-oriented carbon nanotubes forest is hard to synthesize as a film which is used to coat other materials. On the other hand, diamond-like carbon (DLC) has been widely used in various fields as coating film.

As I mentioned in chapter 1, DLC, with a variety of combinations between the sp³ and sp² carbons, exhibits many interesting properties, such as a high electric resistivity, useful optical properties with extreme strength to power lasers and lubrication with extreme hardness in tribology [16-22]. Although various deposition techniques have been developed to obtain different types of DLC such as hydrogenated DLC (a-C:H) and hydrogen-free one (ta-C) [23-31], it has been

currently very difficult to control the microscopic and nanoscopic structures in the DLC. In Chapter 2 [27], we attempted the co-deposition of large organic molecules with the DLC and found that some molecules can be “doped” without decomposition. It is expected that the optical and electronic properties of DLC will be controlled if the nanoscale arrangement of sp² and sp³ carbon atoms can be finely tuned in DLC.

In this chapter, we studied the co-deposition of C₆₀ with the DLC by plasma-assisted chemical vapor deposition (PACVD). C₆₀ has many interesting properties [32-35] which are due to its extended π-electron system and a stable cage structure with high stability. It is of interest whether the cage structure of C₆₀ can survive during the co-deposition. C₆₀ molecules also can be used as carbon source for the carbon materials synthesis. Through C₆₀ ion beams, fragmentation occurs at high energy (400eV- 1kV)[36, 37], which leads to useful properties of the deposited films in tribology. Also it is noted that C₆₀ has a much lower density (1.7 g/cm³) than other carbon allotropes, e.g., 3.5 g/cm³ for diamond and 2.2 g/cm³ for graphite, which will induce a significant stress in the film when mixed. In the experiment, we used a moderate method to incorporate C₆₀ molecules by thermal evaporation in order to avoid breaking the cage structures of C₆₀ molecules. Surprisingly, after the deposition, we found that the obtained “C₆₀” - DLC mixture appears similar to ordinary DLC at first, but swelled by three times and showed strong iridescence after the samples being exposed to the atmosphere. This chapter will discuss this finding as well as its mechanism by thorough analyses including ellipsometry, Scanning Electron Microscopy (SEM), Transmission Electron Microscopy (TEM), Fourier-Transform Infrared (FTIR) and Raman spectroscopies along with the experiments using D₂O and quantum chemical simulations.

3.2 Experimental and theoretical details

3.2.1 Experimental section

In this chapter, “C₆₀-incorporated” DLC co-deposited films were synthesized by using plasma-assisted chemical vapor deposition (PACVD). I used the same vacuum chamber as in Chapter 2. In order to keep the cage structure of C₆₀ during the deposition, suitable adjusting of the equipment had been done to optimize the synthesis process. Some additional parts were equipped to upgrade vacuum chamber. The drawing of the equipment is shown in **Figure 3.1**. Methane gas (99.99%) is used as the carbon and hydrogen source for this experiment with the flow rate of 30 sccm. The pressure of methane gas is also kept at 10 Pa which is the designed experimental pressure. A stable plasma glow was produced by a radio-frequency magnetron sputtering gun (13.56MHz, 20W) equipped with a graphitic carbon plate target (Nilaco Inc., 99.98%, 1 inch diameter). The scattering ions reacted with methane gas and produced C-H plasma shining with blue glow. This plasma glow is typical C-H plasma that contains three kinds of species, CH radical, H_α, and H_β. We used the same plasma species for DLC deposition as the doping experiment of CuPc and PTCDA in chapter 2. Stainless steel was used for making the sample holder and a bias voltage of -400V from ground potential was applied to the samples holders in order to attract plasma radical to deposit on the substrate to form the sp³-carbon-rich DLC [38-40]. Ion current through the substrate was also monitored to estimate the deposition rate of the C-H plasma. The ion current was stable with the value of 600 μA when the substrate is biased -400V, whereas it was less than 10 μA without biasing.

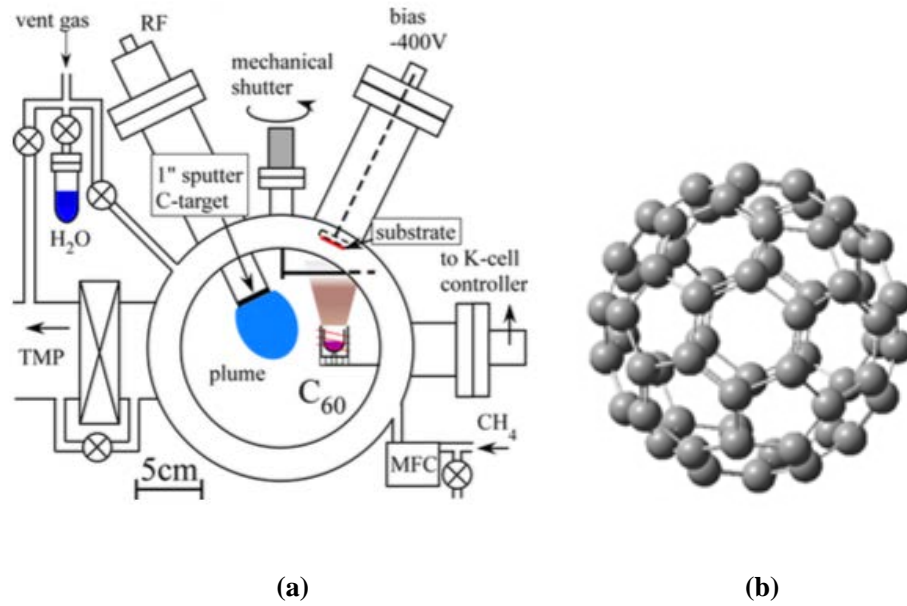


Figure 3.1 (a) Setup for C_{60} +DLC PACVD. The substrate was replaced by a quartz crystal microbalance when the deposition rate was examined. MFC and TMP stand for mass flow controller and turbo molecular pump, respectively. (b) The molecular structure of C_{60} .

In this vacuum chamber, all of the geometry of the samples holder, radio-frequency magnetron sputtering gun, and the molecular source of C_{60} for evaporation were finely and carefully arranged in order to avoid direct deposition from the sputtering gun and plasma-induced damage to the C_{60} source. The sputtering gun was set to avoid directly facing the substrate or the molecular source. It was designed to intend solely to produce stable C-H plasma. I pumped the chamber to 1×10^{-4} Pa prior to the experiment by using a turbo molecular pump.

Through Raman spectroscopy, Fourier-Transform Infrared spectroscopy (FTIR) and X-ray diffraction, the formation of a pure pristine DLC film was confirmed after deposition without molecular source C_{60} evaporation, which was the same as in

Chapter 2. Al₂O₃ (0001) and Si (001) were used as substrates in the experiment. Before these two substrate materials were used for the experiment, various pretreatments had been done to them. Al₂O₃(0001) was cut and heated at 1000 °C for 24h in air and the Si(001) was cleaned by using RCA method [41] and Cr (5nm thick) was deposited on it as the adhesion layer. C₆₀ powder (sublimation grade, Frontier Carbon, Inc.) was heated in a Knudsen-cell which was set directly facing to the samples holder. A moderate heating temperature of 280 °C was used to heat the C₆₀ source. This heating temperature was set to evaporate C₆₀ with a certain rate for the deposition. A mechanical shutter was set to cover the sample holder to precisely control the deposition time. The mechanical shutter completely closed at the beginning of the experiment. After the evaporation rate of C₆₀ source and C-H plasma both became stable, I opened the shutter and begin to synthesize the C₆₀-DLC mixture on the substrate. By using this precise control, the C₆₀ and DLC were perfectly co-deposited with uniformity in the direction of thickness.

During the deposition, the temperature of the substrate was not controlled and increased from room temperature, but it was below 60 °C. The deposition ratio of C₆₀ can be controlled by adjusting the heating temperature and its ratio to DLC was determined by depositing each material separately and measuring the thickness using a quartz crystal microbalance during the deposition, atomic force microscopy and cross sectional SEM afterwards. The ratio will be indicated in the units of equivalent thickness of each material. We examined the film with the composition between C₆₀: DLC = 0.8 : 100 to 2 : 100.

The strong iridescence, which was dependent on incident angles, hindered the correct estimation of the electronic properties (band gap etc.) of the material by

conventional UV-Vis transmission or reflection spectroscopy. We used an angle-resolved spectroscopic ellipsometry (J.A. Woollam M2000-U) to measure the refractive index and extinction coefficient of the films. The spectra were measured with the incident angle ranging from 50° to 75° with a 5° step.

SEM images were obtained using JIB-4600F/HKD (JEOL). The cross sections were prepared by FIB equipped with the SEM. Infrared spectra were obtained by an FTIR-6100 (JASCO). Raman spectra were measured using an InVia Reflex (Renishaw) with x 20 ~ x 50 objective lenses and 532 nm or 785 nm excitation. Thermal stability of the material was examined by heating the sample in air and in a quartz tube sealed under the vacuum of 1×10^{-2} Pa.

3.2.2 Calculation details

A computational method was used for analyzing the reaction of between water vapor and the co-deposited C₆₀-DLC film. All the simulations were carried out using the software of Gaussian 09w [42] and density functional theory (DFT) was employed with exchange-correlation energy functional B3LYP [43]. The electronic states were described by using the basis set of 6-311++G level [44].

The C₁₉H₁₃ radical was constructed by using Gauss View ver. 5.0. It was a model fragment of C₆₀ connected to surrounding DLC network and was used to see the reaction with water vapor. In the simulations, I put three water molecules close to the optimized structure of the C₁₉H₁₃ radical and simulate the whole process of the reaction. Frequency calculation was included in the theoretical work to make sure that all the optimized structures were stable without any imaginary frequencies. The further details will be discussed in the following sections.

3.3 Results and Discussion

3.3.1 The iridescence color of C_{60} -DLC co-deposited film

Figure 3.2 displays optical images of the C_{60} -DLC films (C_{60} : DLC ratio = 1.3 : 100 in nominal thickness of each material), and we can clearly observe the iridescence from these samples. The following results did not significantly change when the ratio was 0.8 ~ 2 : 100, although the interference colors with the given thickness was slightly different. When we change the deposition time, we can obtain samples with a variety of colors. The iridescence shows the tendency to change colors from blue to yellow, *i.e.*, red-shifted colors with the increasing deposition time, which means that we can obtain the colors as designed by controlling the thickness of the films.

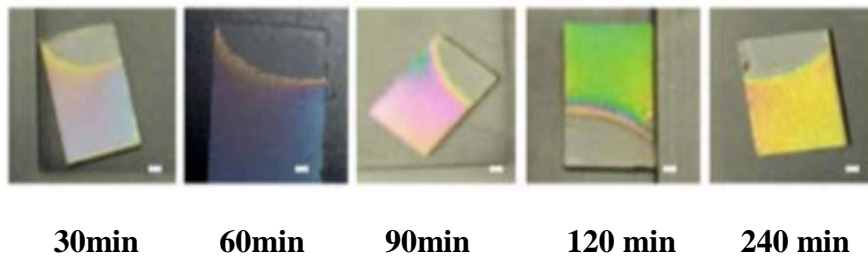


Figure 3.2 Photograph showing the different colors of the C_{60} -DLC film from different deposition time (30 min, 60 min, 90min, 120 min, and 240min, respectively)

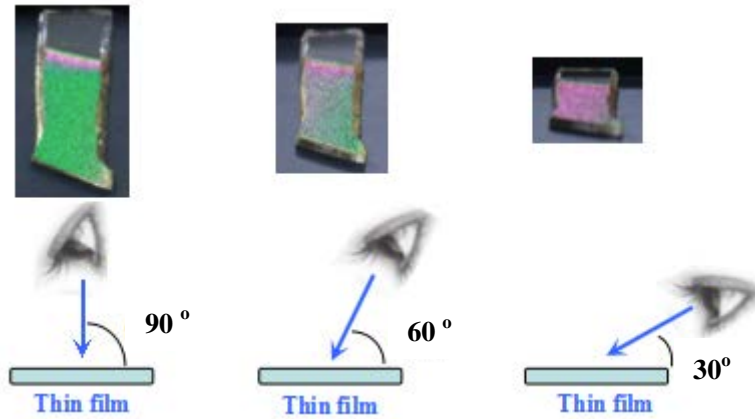


Figure 3.3 The angular dependence of the iridescence

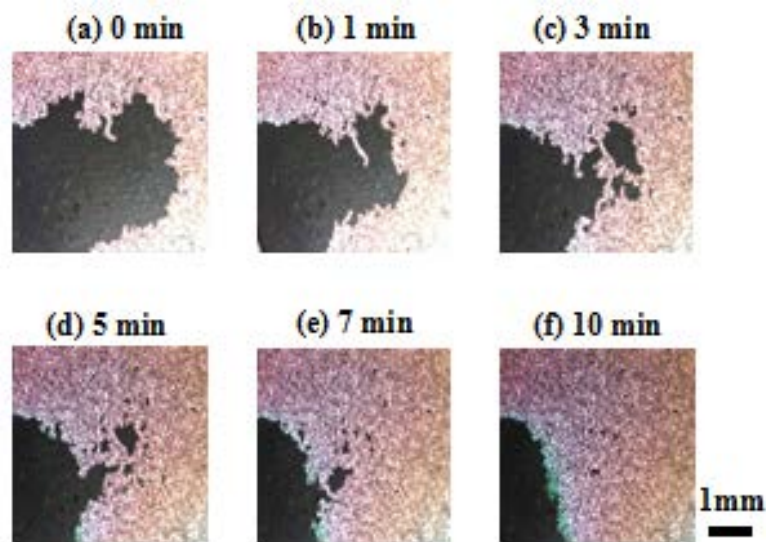


Figure 3.4 The optical microscope images showing the iridescence process (left to right: 10 min). Scale bar is 1mm.

The color changes by the view angle (**Figure 3.3**). We noticed that the iridescence of the samples did not appear when the sample was in the deposition chamber after PACVD. Surprisingly, we found that these colors appear after the samples were exposed to air. **Figure 3.4** shows pictures taken during the appearance of the iridescence. The samples were initially transparent as the pristine DLC films,

and then the iridescence appeared in some parts and spread quickly on the time scale of a few minutes. These changes were irreversible. The iridescence, once appeared, was very stable and it did not change after more than one year in air without any protective treatments. We scratched the film from the substrate and the film did not change the color. It means that the iridescence was not the interference related with the film-substrate interface.

In order to clarify the factors responsible for the color change (**Figure 3.4**), we intentionally introduced various gases (N₂, CH₄, H₂, O₂, CO₂, and H₂O) into the vacuum system for the venting. N₂, CH₄, H₂, O₂ and CO₂ gases were introduced from the vent valve to 1 atm, whereas H₂O vapor was supplied from a glass tube containing H₂O liquid (purified by repeating freeze- pump- melt procedure using liquid N₂ bath) through the vent valve with N₂. After keeping the sample in the chamber filled with those gases for 1 hour, the sample was taken out to ambient condition. The films showed iridescence after H₂O exposure, whereas other gases did not affect the transparency of the films. Nevertheless, the transparent films after the exposure to other gases gradually showed similar iridescence after keeping them under ambient condition.

3.3.2 Optical characterization

3.3.2.1 UV - Vis absorption spectra

This iridescence color on DLC film has not been reported. In order to explain this optical phenomenon, several optical characterization methods were employed in this research.

Firstly, UV-Vis spectra were used to characterize these films. **Figure 3.5** shows

UV-Vis spectra of C_{60} -DLC co-deposited films with different deposition time. The incident light was irradiated from the normal of the sample surface and transmission intensity at each wavelength was measured by Lambda 900 UV-Vis spectrometer. All the spectra show similar tendency as pristine DLC film with different intensity which is related with thickness of the film. However, interference structures are observed in the spectra, which makes consistent measurement was difficult because the iridescence color was strongly dependent on the slight change of the incident angle as shown in **Figure 3.3**.

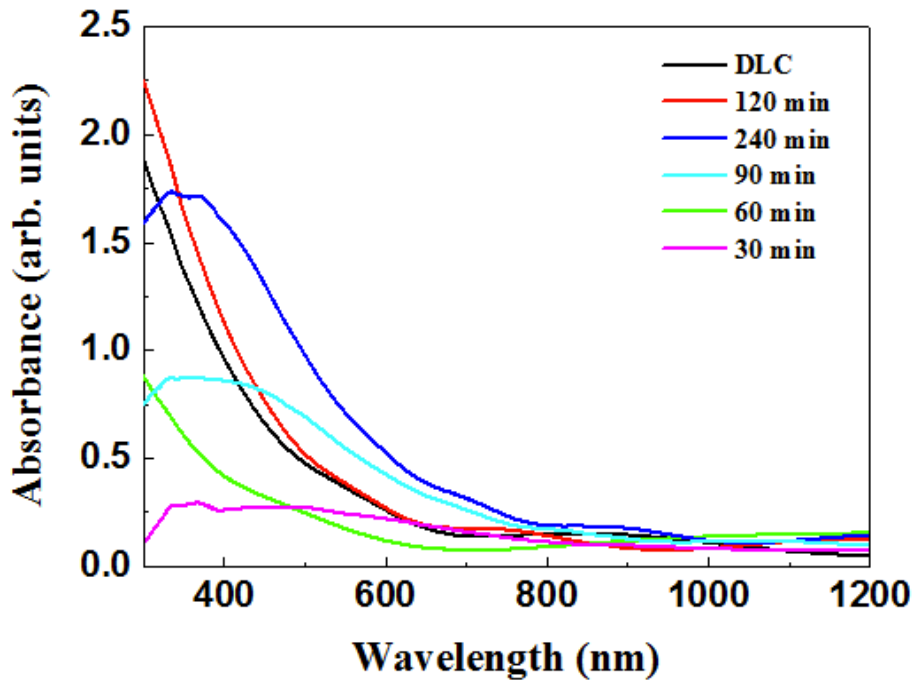


Figure 3.5 Optical absorption spectra of pristine DLC film (Black line) and C_{60} -DLC co-deposited film with different deposition time.

3.3.2.2 Angle-resolved spectroscopic ellipsometry

It is difficult to obtain more optical information except the thickness relationship of these samples by using UV-Vis spectra. Therefore we analyzed the

film by ellipsometry in order to obtain the quantitative optical parameters and information (refractive index and extinction coefficient) on the electronic structure. The samples were characterized by angle resolved spectroscopic ellipsometry (J.A. Woollam M2000-U) with the incident angle (θ) ranging from 50° to 75° with a 5° step in the wavelength range from 200 nm to 1700 nm.

Figure 3.6 (a) and **(b)** show the relationship of the amplitude ratio $\Psi (h\nu)$ and phase difference $\Delta (h\nu)$ to the wavelength of incident light. The amplitude ratio Ψ and phase difference Δ were the basic variable, which were used to construct the model and obtain the other optical constants [45]. The **Figure 3.6(c)** is the depolarization spectrum, which is also used as the one of the basic optical parameters in ellipsometry measurement. In **Figure 3.6**, the green dot lines are the experimental results characterized with different incident angle in the range from 50° to 70° with a 5° step and the red solid lines are the fitting curves [45]. The samples were treated as multilayer structure with many layers, but the best fit was obtained by assuming the three layer structure as shown in **Figure 3.7**. The top layer is the C₆₀-DLC co-deposited film with linearly graded optical constants. The C₆₀-DLC co-deposited film is successfully fit by the graded films.

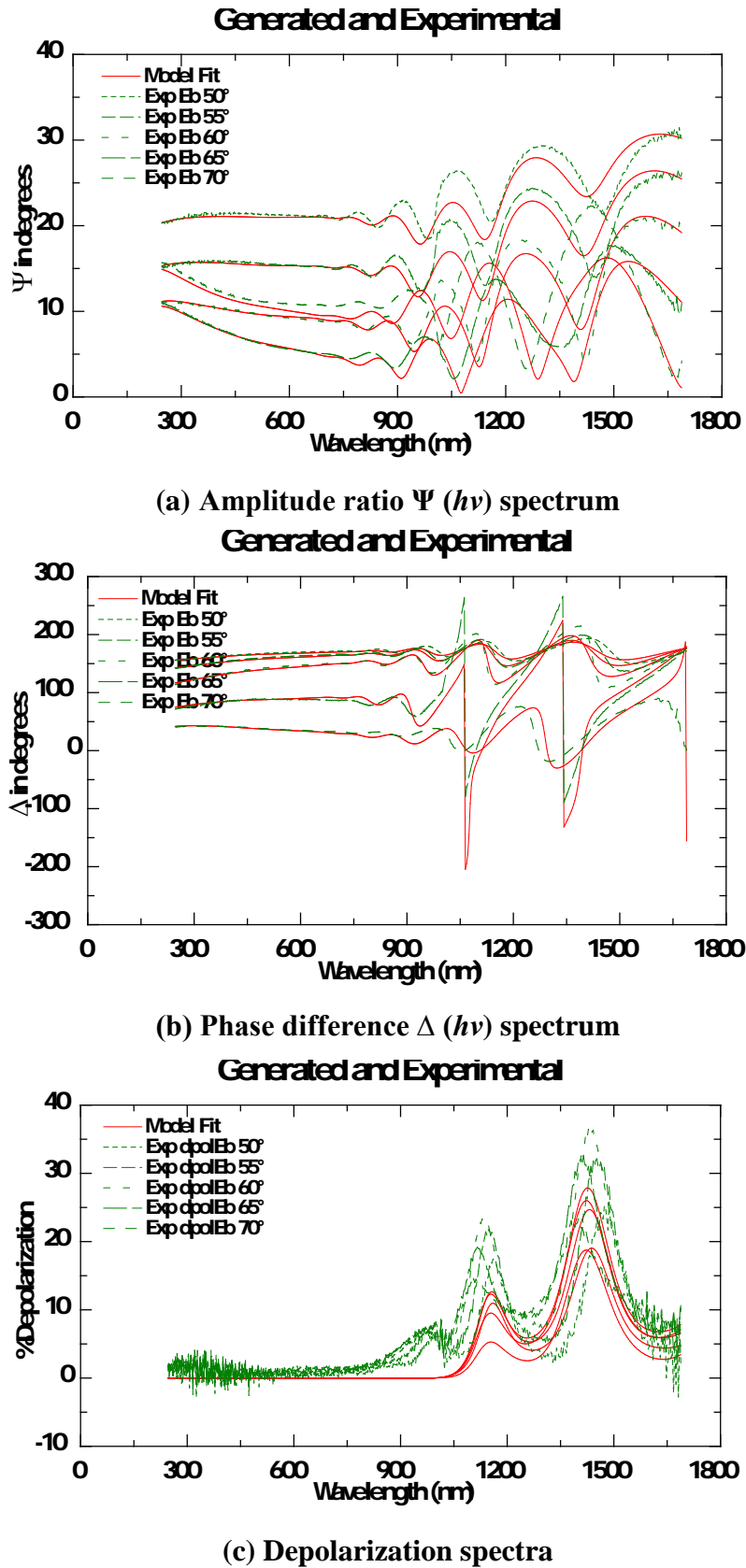


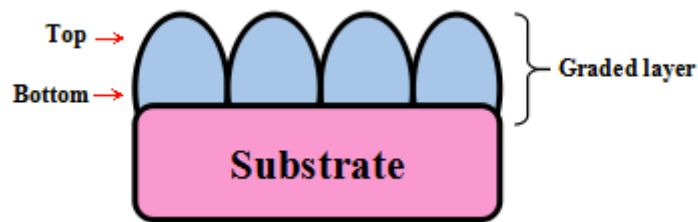
Figure 3.6 The basic variable measured by ellipsometry. (a) Amplitude ratio $\Psi (h\nu)$ spectrum, (b) Phase difference $\Delta (h\nu)$ spectrum, and (c) Depolarization spectra

Graded layer of general oscillator	892 nm
Cr layer	5nm
SiOx	0.4nm
Si substrate	

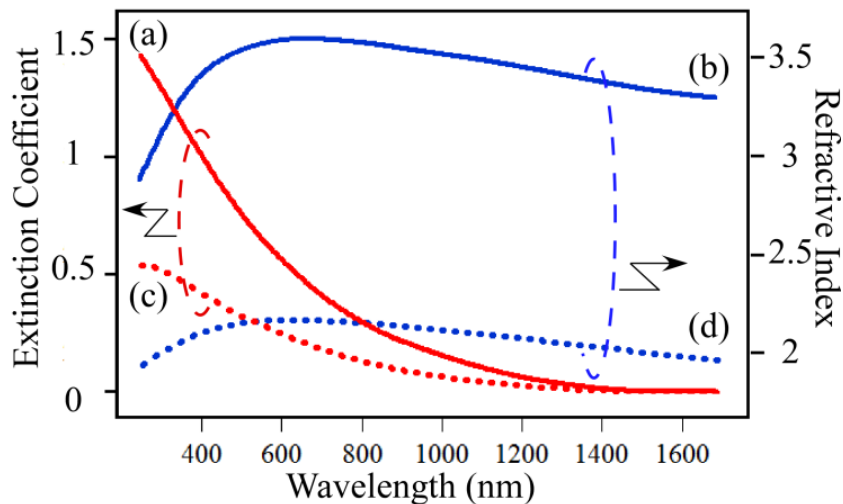
Figure 3.7 The model structure finally used to fit the ellipsometry result. The samples are treated as multilayer structure with many layers, but best fit was obtained by assuming the two layered structure. The top layer is the C_{60} -DLC co-deposited film with linearly grade optical constants.

Figure 3.8 shows the refractive index and extinction coefficient of a sample obtained from the model fitting using linearly graded optical constants only depending upon the height in the film (**Figure 3.6** and **Figure 3.7**). There are considerable differences in both the refractive index and extinction coefficient between the top and the bottom of the C_{60} -DLC film. It is probably due to the non-uniform thickness of the films as revealed by SEM images later. The material is densely distributed at the bottom (**Figure 3.8(A)**). We can naturally assume that the bottom part represent genuine material properties. The refractive index is about 3.6 (maximum value achieve at around 600nm) in the wavelength range from 200 nm to 1700 nm, while the extinction coefficient have a greater difference from about 1.4 to the 0.0 corresponding to the wavelength range from 200 nm to 1700 nm. This high refractive index with small extinction coefficient causes the strong interference within the film, which leads to the vivid color that is dependent on the film thickness. We

can discuss the band gap of the material from extinction coefficient. In curve (a) (Figure 3.8(B)), a significant absorption tail starts at 1200 nm ($\sim 1\text{eV}$), while it does not saturates even at 200 nm (6 eV). This broad tailing indicates that the film is composed of various components in microscopic scales, probably sp^2 and sp^3 clusters.



(A) Graded layer of our film



(B) Extinction coefficients (a)(c) and refractive index (b)(d)

Figure 3.8 (A) Structure of the film that account for the fitting (B) Extinction coefficients (a) (c) and refractive index (b)(d) of C_{60} -DLC co-deposited film obtained by fitting angle-resolved spectroscopic ellipsometry data. Curve (a) and (b) are the optical parameters which correspond to the bottom of the film while curve (c) and (d) correspond to the top.

3.3.3 Nano structure

The appearance of the color when exposed to the water-containing atmosphere was associated with the microscopic inhomogeneity of the film. A stylus profilometer analysis (Veeco DEKTAK 6M) resulted in a very rough surface with the lateral thickness difference much exceeding the nominal thickness of the film. We consider that this roughness also contributes to the strong iridescence colors. Since it has been reported that strong iridescence can be induced by nanostructures in the films by internal scattering [46-47], we examined the nanoscale structures in the films.

3.3.3.1 SEM images

Figure 3.9(a) shows a plan view SEM image of a sample showing iridescence. The surface showed wavy crazing. There were cracks of several tens of micrometers. It was not empty inside the crack. We obtained the cross sectional images by using Focused Ion Beam (FIB) etching. Carbon or tungsten coating layers were first deposited on the film surface to protect the film from the damage caused by the scattered ions during the preparation of the cross-section. **Figure 3.9(b)** and **(c)** shows the cross section image of the same sample shown in **Figure 3.9(a)**. In **Figure 3.9(b)**, it is noticed that the film thickness is not uniform, which is in agreement with the model used in the ellipsometry analysis (**Figure 3.7**, **Figure 3.8**). The magnified image **Figure 3.9(c)** shows that there were grain-like structures or “popcorn-like” structure with the size ranging from 10 to 100 nm. The structure with this size causes strong iridescence due to complicated internal scattering [46] as

known in some insects [47].

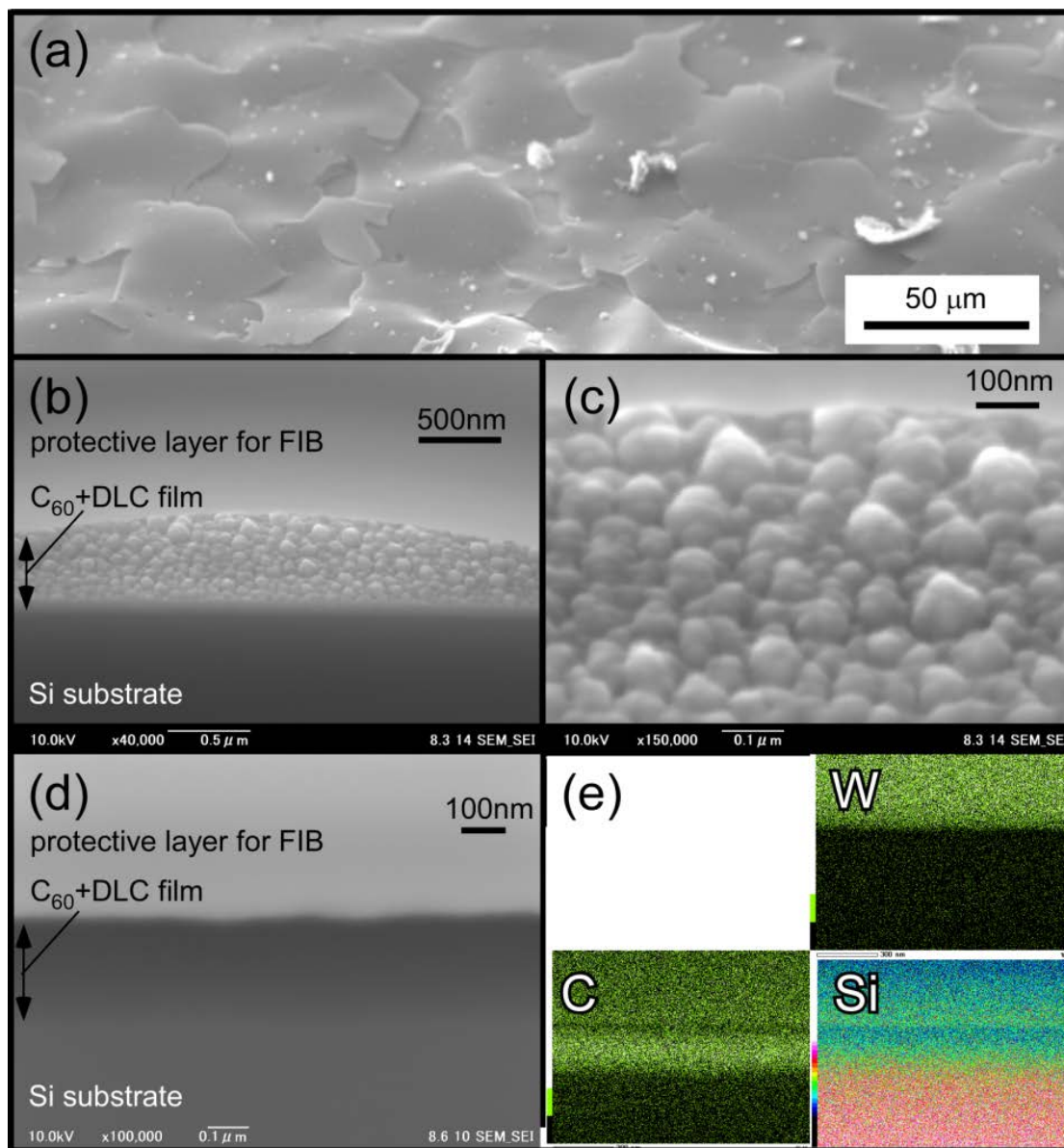


Figure 3.9(a) Plane view SEM image of a sample showing iridescence. (b)(c) Cross section SEM images prepared by FIB. (d) Cross section SEM image of the C_{60} +DLC film before showing iridescence. (e) EDS mapping of W, C, Si of the area shown in (d).

I also observed cross sectional SEM images of a sample before showing iridescence for comparing the nano-structure. The sample with less C₆₀ content (0.8:10) was vented with N₂ gas and was quickly introduced to FIB-SEM. A part of the sample already showed iridescence, but we could find a region with flat surface on the sample. **Figure 3.9(d)** shows the cross section SEM. There were no “popcorn-like” structures. **Figure 3.9(e)** shows EDS mapping of the same region as **Figure 3.9(d)**. It was confirmed that the structureless area was composed of carbon. It should be noted that the thickness of the co-deposited film before and after iridescence was very different. By normalizing with the deposition time (2 hours for **Figure 3.9 (a), (b), (c)** and 1.5 hours for **Figure 3.9 (d), (e)**), it was concluded that the thickness of the film expanded by more than twice.

3.3.3.2 The detail of “popcorn” nano-structure

From the SEM images in **Figure 3.9**, the “popcorn-like” nanostructures have been found in C₆₀-DLC co-deposited film after showing iridescence. By comparing the films before and after showing iridescence (**Figure 3.9(d), Figure 3.9(b)**), we noticed that the nano-structures are very important to this interesting optical property. In this section, The TEM was used for studying the “popcorn-like” nano-structure in details.

Figure 3.10 shows the TEM images of nano-structure on the substrate. **Figure 3.10(a)** shows the first arrays of the “popcorn-like” nano-structures are on the substrate, they expressed a certain degree of periodicity. **Figure 3.10(b)** shows the one of those nano-structures. Crystal order was not observed.

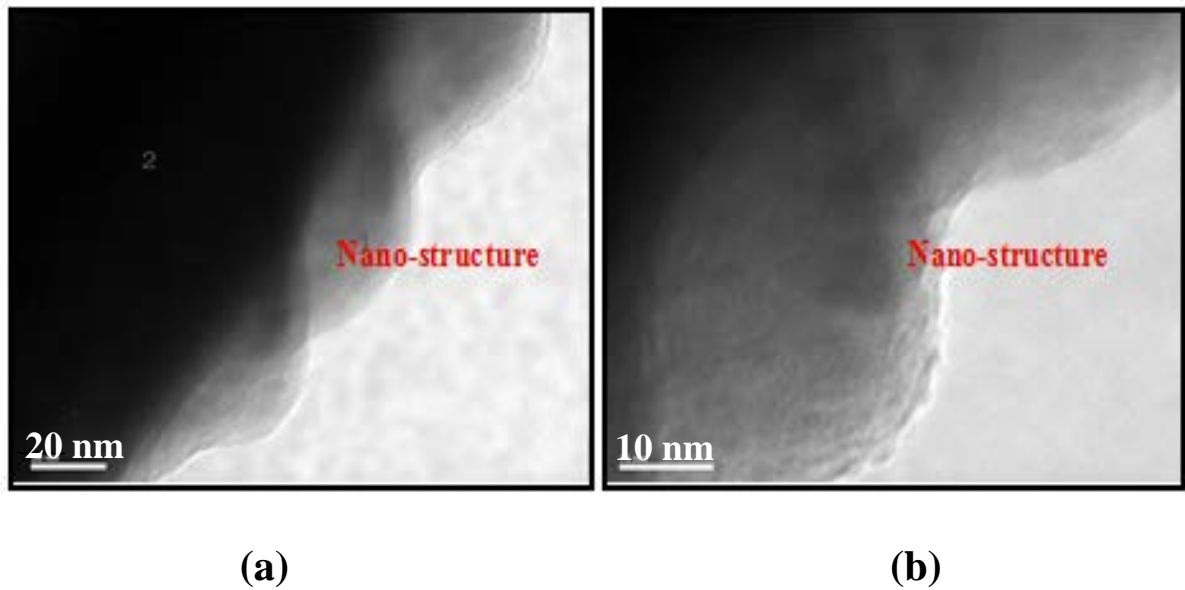


Figure 3.10 TEM images of the nano-structure with different length scale. (a) an array of the nano-structure on the substrate. (b) One of the nano-structure with the diameter about 50nm.

3.3.4 FTIR and Raman analysis

3.3.4.1 The concentration of the sp² and sp³ carbon

Information of the C₆₀-DLC co-deposited film on microscopic chemical structures was obtained from vibrational spectroscopy. **Figures 3.11 (a) and (b)** are the FTIR spectra of CH- stretching region of C₆₀-DLC co-deposited film and pristine DLC film, respectively. The multiple peaks of C₆₀-DLC co-deposited film and the pristine DLC film were deconvoluted into four individual absorbance peaks by Gaussian fitting. The individual peaks centered at 2870 cm⁻¹, 2921 cm⁻¹ and 2956 cm⁻¹ in C₆₀-DLC co-deposited film, and centered at 2871 cm⁻¹, 2917 cm⁻¹ and 2951 cm⁻¹ in the pristine DLC film, are assigned to the stretching vibration mode of the C-H bond of the aliphatic group which are related to sp³ carbons. The peaks around 2985 cm⁻¹

and 3002 cm^{-1} of the C_{60} -DLC co-deposited film and pristine DLC film, respectively, are assigned to the C-H bonds, but it is related to the sp^2 carbons [48-50]. The pristine DLC mostly contains sp^3 carbon with a small fraction of $0.028\text{ }sp^2$ carbon, and in C_{60} +DLC, the ratio of sp^2 had increased to 0.167 , which is also a small fraction compared to the rest ratio of sp^3 .

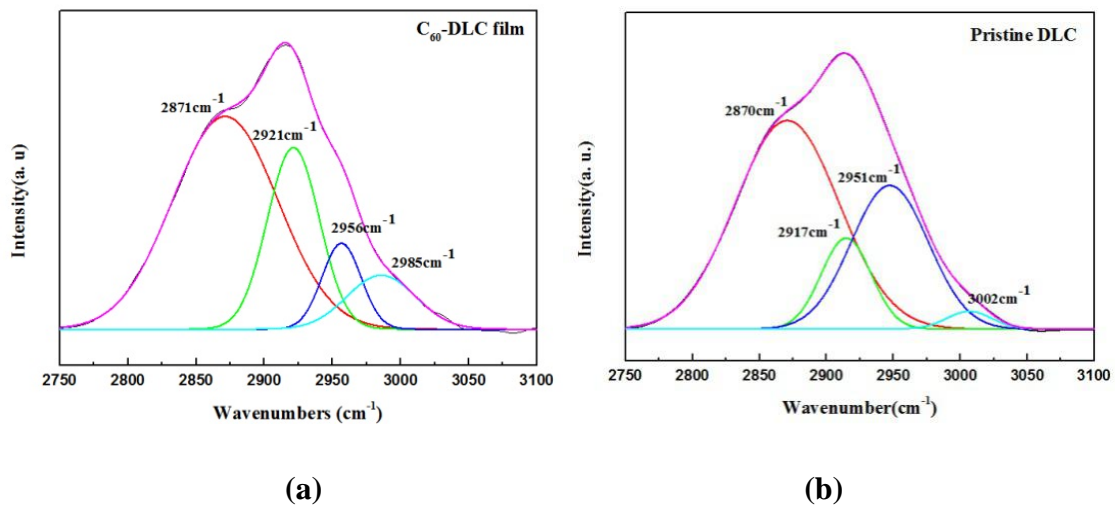


Figure 3.11 The FTIR spectrum (CH-stretching region) of (a) C_{60} +DLC co-deposited film and (b) pristine DLC film.

The Raman spectrum of the C_{60} -DLC co-deposited film after Gaussian-fitting is shown in **Figure 3.12**. This multiple peak of the diamond-like carbon is composed of the D and G peaks, the D peak corresponds to sp^3 centered at 1330 cm^{-1} , and the G peak corresponds to sp^2 centered at 1612 cm^{-1} . The ratio of sp^2/sp^3 can also be calculated using their peak areas. The areas ratio (I_G/I_D) of the D peak and G peak showed values around 0.11 . Raman spectrum of pristine DLC films (**Figure 2.7** in Chapter 2) also showed I_G/I_D very close to this value [51]. This finding, together with FTIR data, suggests that the main difference between C_{60} -DLC co-deposited film

and pristine DLC film is the concentration of CH bonds with sp² carbons. Since the optical constants are probably related with the concentration of sp² carbons more than CH bonds with sp² carbons, this result confirms the importance of popcorn-like nanostructure for the iridescence.

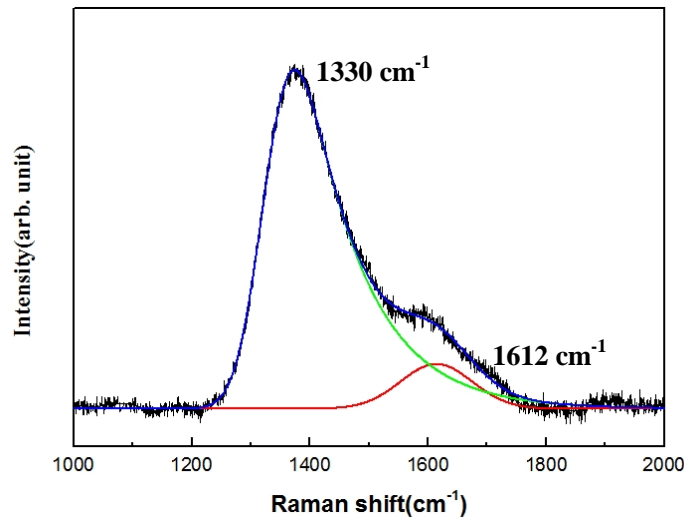


Figure 3.12 The main DLC Raman peak of a C₆₀-DLC co-deposited film and fitting.

The concentration of DLC is the same as chapter 2 of the rich-sp³ DLC.

We also measured broad band FTIR of C₆₀-DLC co-deposited film grown on IR-transparent KBr substrates and the FTIR spectra is shown in **Figure 3.13**. The typical pristine C₆₀ peaks are around 530 cm⁻¹, 580 cm⁻¹, 1180 cm⁻¹, 1430 cm⁻¹ [48, 52]. In **Figure 3.13**, no peaks characteristic to pristine C₆₀ were observed. It shows that the C₆₀ cage was chemically connected with carbon in the DLC network and/or hydrogen atoms or even become broken, which is reasonable in the plasma process.

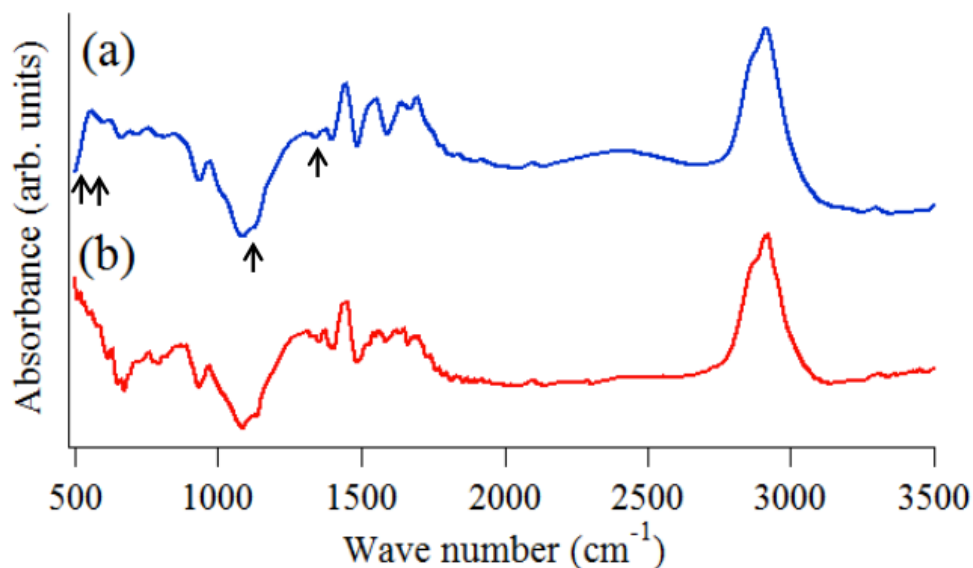


Figure 3.13 FTIR of (a) C_{60} +DLC and (b) DLC grown on KBr substrates. Peaks corresponding to C_{60} (indicated by arrows, 530 cm^{-1} , 580 cm^{-1} , 1180 cm^{-1} and 1430 cm^{-1} [48, 52])

3.3.4.2 Formations mechanism investigation of nano “popcorn”

In Chapter 1 and in the introduction part of this Chapter, I introduced recent researches on the carbon based materials. There are reports on iridescent carbon nanotube forests [15] and DLC coating fabricated by C_{60} ion bombardment that is not iridescent [29], the reaction of DLC-related material with water vapor to yield an iridescent material as shown here has not been reported to the best of my knowledge. Therefore I examined the nature of the reaction by two means: FTIR analysis after H_2O and D_2O gas exposure, and computational chemistry. Firstly, I designed the experiment to compare the effects of H_2O and D_2O exposure.

I made two of the closed boxes shown in **Figure 3.14** which was full of the N_2 gas (99.99%) with pressure of 1 atm. I confirmed that the N_2 and pressure would not

affect the film. These two boxes had the same environmental parameters such as the same pressure (1 atm) and temperature (Room temperature). All the samples were divided into two parts and placed into the closed boxes separately more than 12 hours to make sure the samples had a full contact with H_2O/D_2O vapor

After D_2O/H_2O experiment, FTIR (FTIR-6100, JASCO) was used for characterizing the different chemical bonds existed in these films treated by D_2O and H_2O separately.

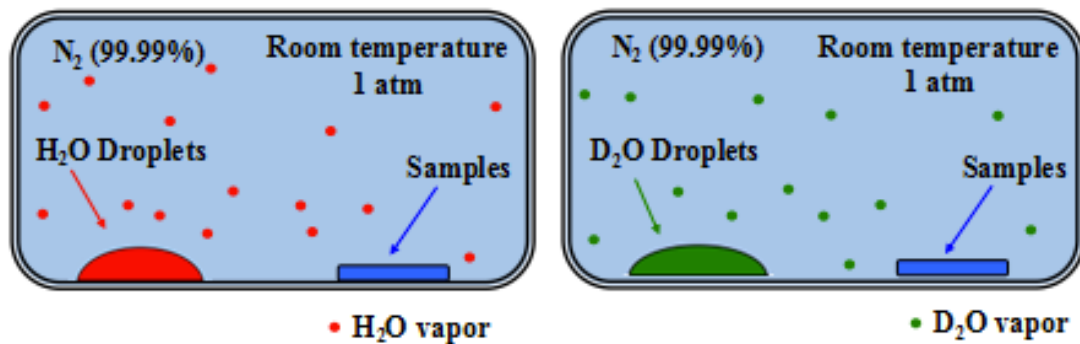


Figure 3.14 The H_2O and D_2O comparing experiment. These two closed boxes were filled with N_2 gas, and both of them had the same pressure of 1 atm and temperature of room temperature.

Figure 3.15 shows the FTIR spectrum of the C_{60} -DLC co-deposited film prepared on a Al_2O_3 substrate, which is transparent between 1500 cm^{-1} and 4000 cm^{-1} . I notice a broad peak around 3300 cm^{-1} that corresponds to OH stretching. The peak is broad probably because of the influence of hydrogen bonds. However, it is difficult to identify this as alcohol formation in $C_{60} + \text{DLC}$, because there is a peak corresponding to H_2O molecule at 1612 cm^{-1} . There is a possibility of physisorbed water. It was found that the C_{60} -DLC co-deposited films wet very well with water droplet. This

behavior is strongly different from pristine DLC that is hydrophilic. In order to clarify the nature of the reaction, we used D_2O instead of H_2O to vent the PACVD chamber and kept the sample adjacent to a D_2O droplet in a sealed box just prior to the FTIR measurement in air. The result of D_2O -exposed C_{60} -DLC co-deposited film is shown in **Figure 3.15(b)**. The broad peak at 2900 cm^{-1} (OH) was much weakened and H_2O peak at 1612 cm^{-1} almost disappeared. Instead, new peaks around $3600 - 3800\text{ cm}^{-1}$ appeared. These peaks correspond to isolated -OH stretching vibration. Also we notice that weak peaks corresponding to -OD stretching vibration appeared in the range between $2600 - 2750\text{ cm}^{-1}$ [53-54].

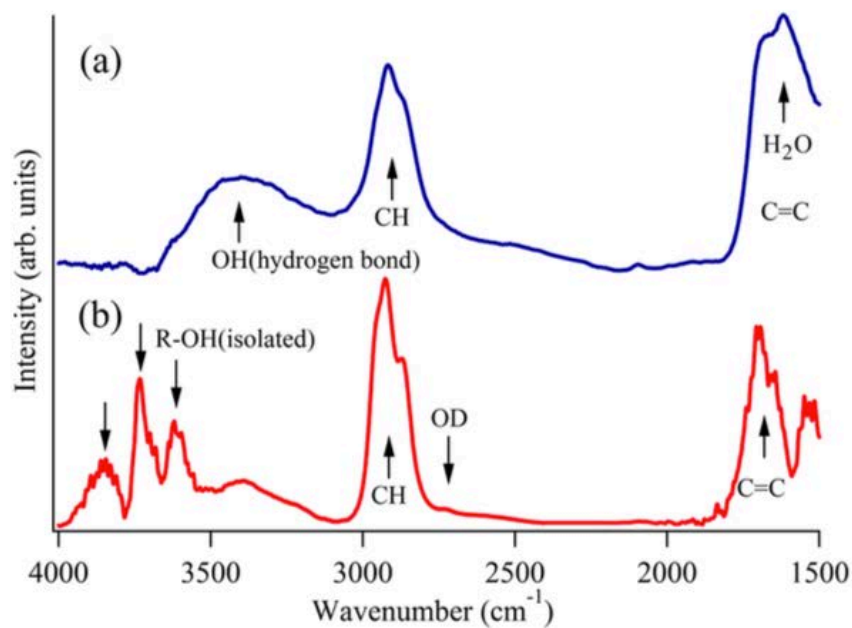


Figure 3.15 The FTIR spectra of C_{60} -DLC films exposed (a) to H_2O vapor and (b) to D_2O vapor.

Since the isotope exchange of OH and OD is very quick ($< \text{minutes}$) in some cases [53], the information obtained from **Figure 3.15** is rather limited. Nevertheless,

it clearly shows that the C₆₀-DLC co-deposited film reacted with H₂O (or D₂O) to make -OH (or -OD) bonds.

Now it is clear that the C₆₀-DLC co-deposited is metastable as prepared and reacts with water vapor to make -OH bonds. The film expands and makes nano-scale grain structures in the course of that reaction. It is presumable that the C₆₀ molecule co-deposited with DLC makes chemical bonds with surrounding carbon and hydrogen. Because the C₆₀ molecule is made of sp²-carbon atoms, additional one bond can be formed without breaking the cage. Although the cage has already been broken during the deposition, but complete decomposition is not presumable because such materials, for example, DLC made from C₆₀ ion bombardment, does not show iridescence [29]. It is reasonable to assume that partially reacted C₆₀ cages are important to explain the present findings.

3.3.5 The reaction simulations between C₆₀-DLC film and water

The question is whether this C₆₀ with extra bonds will react with H₂O molecules and whether the reaction causes expansion of the material. We conducted quantum chemical calculation of model systems to clarify the nature of the reaction. We will show one example: A fragment of C₆₀ (C₁₄H₈) was first connected randomly with 5 -CH to make C₁₉H₁₃ to mimic the C₆₀ embedded in DLC. The size of this model molecule was selected to finish a calculation within a reasonable time. The structure of the C₁₉H₁₃ molecule was optimized with DFT at 6-311++G level using B3LYP functional. This molecule is a neutral radical, which commonly exists even in ordinary DLC [55-59]. Then three H₂O molecules were placed close to (but about van der Waals distance) with the C₁₉H₁₃ molecule. The structure of the initial

configuration is shown in **Figure 3.16**. Then this configuration is again optimized with DFT at the same level of calculation. The result is shown in **Figure 3.17**. The molecule reacted with two H_2O molecules to make $-OH$ bonds. One molecule did not react and moved out from the system. It should be noted that the fused aromatic rings of part of C_{60} were rearranged to make larger rings and a new ring with a side chain. Since the compact fused rings became buckled larger rings and reacted CH and OH became a side chain, the size of the molecule became greater. This behavior, which can be said as cage breaking of C_{60} , can qualitatively account for the expansion of the films.

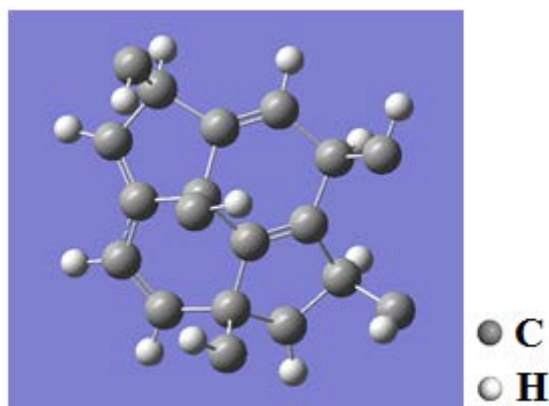


Figure 3.16 The optimized structure of $C_{19}H_{13}$ for the C_{60} fragment. The neutral radical was used for the next reaction simulation.

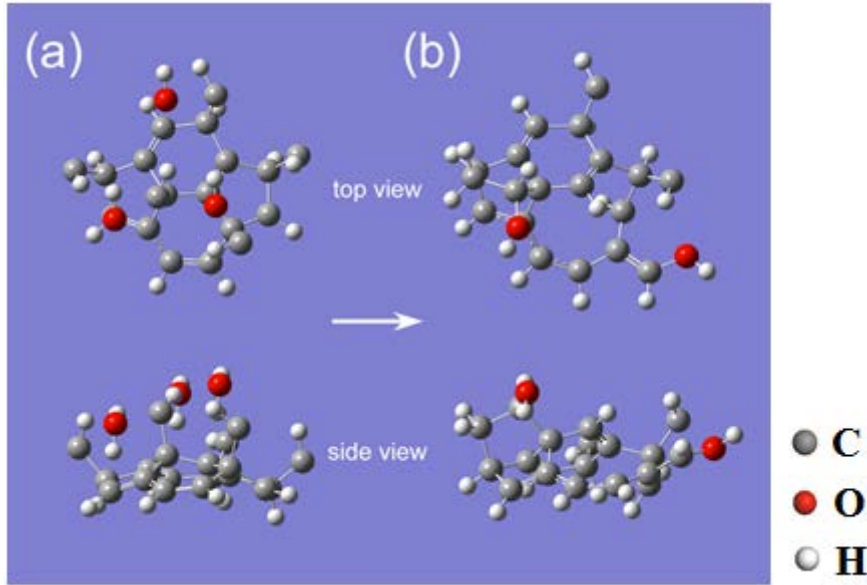


Figure 3.17 Quantum chemical calculation of a model system. (a) Before the reaction. Three H_2O molecules with optimized $C_{19}H_{13}$ (model of C_{60} embedded in DLC). (b) After the reaction. Optimized structure starting from (a)

The formation mechanism of the grain structure (10-100nm), which is by far greater than the size of a C_{60} molecule, is not clear from this calculation. We speculate that the distance between C_{60} molecules in C_{60} (1%) + DLC, which is roughly 5 nm, might be related with the size of the structure. The characteristic length of the local deformation to the mechanical stress induced by the chemical reaction around “ C_{60} ” will be important for the size of the grain structure. We stop this discussion by commenting that the concept of embedding the metastable reaction centers in carbon-based material will be useful for various purposes, for example, post-modification of the material as in the present experiment, sensor applications. The colorful carbon material obtained in the present work will find application as pigment and water sensor.

3.3.6 Thermal stability

Finally, I examined the thermal stability of C₆₀-DLC co-deposited films, which is useful information for the application. Since the iridescence comes from the nanostructures, the optical observation is a convenient and reliable measure of the stability. **Figures 3.18 (a)** and **(b)** show the optical image of the film heated in ambient condition and under vacuum (sealed under 1×10^{-2} Pa at RT), respectively. The film started to lose color at ~ 350 °C and gradually disappeared before 550 °C in atmosphere without observable flames. On the other hand, under vacuum conditions, the film maintained the colorful iridescence up to 550 °C and gradually lost color around 600 °C. This result shows that the carbon nano-structures can be used for optical applications up to this temperature if supplied with appropriate coating to shut out oxygen.

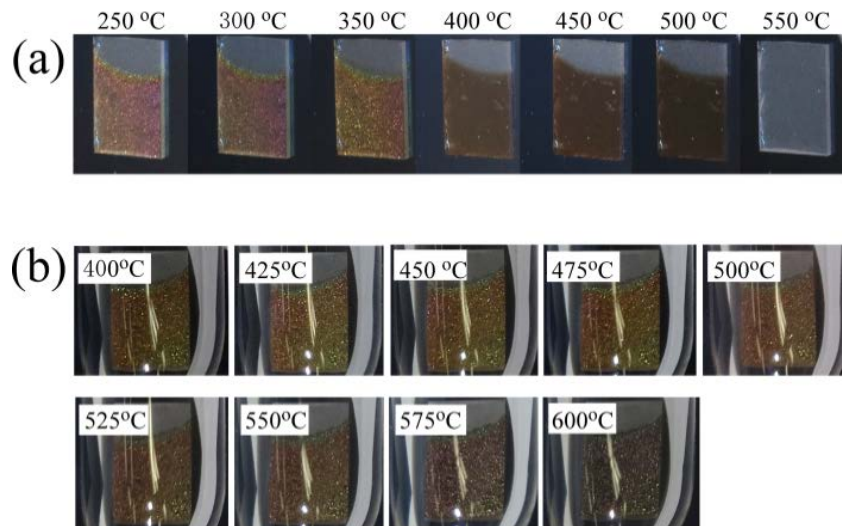


Figure 3.18 Optical images of the film during heating experiment in (a) atmosphere and (b) in vacuum (sealed in a quartz tube at 1×10^{-4} Pa at RT). The heating rate was 0.5 °C/min.

3.4 Conclusion

In conclusion of this chapter, I synthesized a new carbon film with an iridescence which can be tuned from blue to red by changing the thickness of the film. I found that “popcorn-like” structures in the film emerging like popcorn after exposure to air containing H₂O vapor. The infrared absorption and Raman spectra showed that C₆₀ was decomposed and produced sp² carbon clusters in the DLC. A strong iridescence appeared from the high refractive index (3.6), relatively low absorption and internal scattering caused by sub-wavelength structures of the material. I conducted detailed spectroscopic examination and quantum chemical calculation of model systems. This phenomenon occurs from the cage breaking of C₆₀, initially with extra chemical bonds with surrounding DLC, from the reaction with H₂O molecules. The present result shows the possibility of nano-structured carbons as optical functional materials.

Reference

1. R. Sanchez-Valencia, T. Dienel, O. Gröning, et al., *Nature*, **2014**, 512, 61.
2. F. Yang, X. Wang, D. Q. Zhang, et al., *Nature*, **2014**, 510, 522.
3. Z. M. Li, J. P. Zhai, H. J. Liu, et al., *Applied Physics Letters*, **2004**, 85, 1253.
4. P. Li, J. Zhang, *Progress in Chemistry*, **2013**, 25, 167.
5. S. Hitosugi, W. Nakanishi, T. Yamasaki, H. Isobe, *Nature Communications*, **2011**, 2, 492.
6. H. Omachi, T. Nakayama, E. Takahashi, Y. Segawa, K. Itami, *Nature Chemistry*, **2013**, 5, 572.
7. D. Ogrin, R. E. Anderson, R. Colorado, B. Maruyama, M. J. Pender, V. C. Moore, et al, *Journal of Physical Chemistry C*, **2007**, 111, 17804.
8. Y. Tao, C. Degen., *Advanced Materials*, **2013**, 25, 3962.
9. S. Yamanaka, N. S. Kini, A. Kubo, S. Jida, H. Kuramoto, *Journal of the American Chemical Society*, **2008**, 130, 4303.
10. X. A. Chen, S. Yamanaka, *Chemical Physics Letters*, **2002**, 360, 501..
11. F. Bonaccorso, Z. Sun, T. Hasan, and A. C. Ferrari, *Nature Photonics*, **2010**, 4, 611.
12. Qiaoliang Bao and Kian Ping Loh, *ACS Nano*, **2012**, 6, 3677.
13. Keun Soo Kim, Yue Zhao, Houk Jang, Sang Yoon Lee, Jong Min Kim, et al., *Nature*, **2009**, 457, 706.
14. Z. P. Yang, L. Ci, J. A. Bur, S. Y. Lin, and P. M. Ajayan, *Nano Letters*, **2008**, 8, 446.
15. P. Vinten, J. Lefebvre, and P. Finnie, *Applied Physics Letters*, **2010**, 97, 101901.

16. A. S. Loir, F. Garrelie, C. Donnet, F. Rogemond F, J. L. Subtil, B. Forest, et al., *Surface and Coatings Technology*, **2004**, 188-189, 728.
17. P. S. Banks, L. Dinh, B. C. Stuart, M. D. Feit, A. M. Komashko, A. M. Rubenchik, et al., *Applied Physics A*, **1999**, 69, 347.
18. A. S. Loir, F. Garrelie, C. Donnet, J. L. Subtil, M. Belin, B. Forest, et al., *Applied Surface Science*, **2005**, 247, 225.
19. A. H. Lettington, C. Smith, *Diamond and Related Materials*, **1992**, 1, 805.
20. B. Zhou, A. V. Rogachev, Z. B. Liu, X. H. Jiang, R. Q. Shen, A. S. Rudenkov, *Surface and Coatings Technology*, **2012**, 208, 101.
21. A. Grill, *Diamond and Related Materials*, **1999**, 8, 428.
22. J. Robertson, *Materials Science and Engineering: R: Reports*, **2002**, 37, 129.
23. A. Grill, *Thin Solid Films*, **1999**, 355- 356, 189.
24. C. Ronning, U. Grisemeier, M. Gross, H. C. Hofsass, R. G. Downing, G. P. Lameze, *Diamond and Related Materials*, **1995**, 4, 666.
25. J. Y. Jao, S. Han, C. C. Yen, Y. C. Liu, L. S. Chang, C. L. Chang, et al, *Diamond and Related Materials*, **2011**. 20, 123.
26. S. Gayathri, N. Kumar, R. Krishnan, S. Amirthapandian, T. Ravindran, S. Dash, et al, *AIP Advances*, **2013**, 12, 122113.
27. W. Xie, N. Muraya, T. Yanase, T. Nagahama, T. Shimada, *Japanese Journal of Applied Physics*, **2014**, 53, 010203.
28. F. Bernhardt, K. Georgiadis, L. Dolle, O. Dambon, F. Klocke, *MaterialWiss Werstofftech*, **2013**, 44, 661-6.
29. M. Kadem, O. V. Penkov, V. E. Pukha, M. V. Maleyev, D. E. Kim, *Carbon*, **2014**, 80, 534.

30. F. Piazza, D. Grambole, D. Schneider, C. Casiraghi, A. C. Ferrari, J. Robertson, *Diamond and Related Materials*, **2005**, 14, 994.
31. F. Guzman, M. Ruiz, E. Valderrama, M. Favre, H. Bhuyan, E. S. Wynham, H. Chuaqui, *Journal of Physics: Conference Series*, **2014**, 511, 012017.
32. W. Kratschmer, L. D. Lamb, K. Fostiropoulos, D. R. Huffman, *Nature*, **1990**, 347, 354.
33. M. R. Cerón, M. Izquierdo, A. Aghabali, J. A. Valdez, K. B. Ghiassi, M. M. Olmstead, A. L. Balch, F. Wudl, and L. Echegoyen, *Journal of the American chemical society*, **2015**, 137, 7502.
34. K. Wojciechowski, T. Leijtens, S. Siprova, C. Schlueter, M. T. Hörantner, et al, *J. Phys. Chem. Lett.*, **2015**, 6, 2399.
35. E. Pukha, E. N. Zubarev, A. N. Drozdov, A. T. Pugachov, S. H. Jeong, and S. C. Nam, *Phys. D: Appl. Phys.*, **2012**, 45, 335302.
36. Z. Thang, X. Cai, B. Ren, et al, *Journal of Chemical Society*, **1997**, 93, 3703.
37. H. Gaber, H. G. Busmann, R. Hiss, et al, *Journal of Physical Chemistry*, **1993**, 97, 8244.
38. S. Miyake, T. Shindoi, M. Miyake, *J. Nano.*, **2014**, 657619.
39. D. Sheeja, B. K. Tay, S. P. Lau, X. Shi, *Wear*, **2001**, 249, 433.
40. W. Dai, H. Zheng, G. Wu, A. Wang, *Vacuum*, **2010**, 85, 231.
41. Kern, *Journal of the Electrochemical Society*, **1990**, 137, 1887.
42. Gaussian 09w, M.J. Frisch, G.W. Trucks, H.B. Schlegel, G.E. Scuseria, et al.
43. P. J. Stephens, F. J. Devlin, C. F. Chabalowski, M. J. Frisch, *J. Phys. Chem.*, **1994**, 98, 11623.
44. M. J. Frisch, John A. Pople, and J. Stephen Binkley, *J. Chem. Phys.*, **1984**, 80,

3265.

45. H. Fujiwara, Spectroscopic Ellipsometry Principles and Applications, **2007**.
46. H. Tada, S. E. Mann, I. N. Miaoulis, P. Y. Wong, Optics Express, **1999**, 5, 87.
47. V. Sharma, M. Crne, J. O. Park, M. Srinvasarao, Science, **2009**, 325, 449.
48. A. M. Vassallo, L. S. K. Pang, P. A. Cole-Clarke, M. A. Wilson, Journal of The American Chemical Society, **1991**, 113, 7820.
49. A. Gril, V. Pate, Applied Physics Letter, **1992**, 60, 2089.
50. M. H. Ahmed, J. A. Byrne, J.A.D. McLaughlin., A. Elhissi, W. Ahmed, Applied Surface Science, **2013**, 273, 507.
51. M. Yoshikawa, G. Katagiri, H. Ishida, A. Ishitani, Journal of Applied Physics, **1988**, 64, 6464.
52. G.V. Andrievsky, V.K. Klochkov, A.B. Bordyuh, G.I. Dovbeshko, Chemical Physics Letters, **2002**, 364, 8.
53. T. Shimanouchi, Pure and Applied Chemistry, **1966**, 12, 287.
54. E. Libowitzky, Monoshaften fur Chemie, **1999**, 130, 1047.
55. H. Ahmed, J. A. Byrne, Applied Surface Science, **2012**, 258, 5166.
56. A. Nagaoka, N. Watanabe, A. Kouchi, Journal of Physical Chemistry A, **2007**, 111, 3016.
57. H. J. Sterling, E. R. Williams, Analytical Chemistry, **2010**, 82, 9050.
58. S. Schutte, S. Will, H. Mell, W. Fuhs, Diamond and Related Materials, **1993**, 2, 1360.
59. J. Robertson, Diamond and Related Materials, **1997**, 6, 212.

Chapter 4. Design of carbon-doped hexagonal boron nitride nanosheets by density functional theory

4.1 Introduction

Graphene is the one of the carbon allotropes with a flat monolayer structure with a two-dimensional (2D) hexagonal lattice. The spectacular optical, electronic, and mechanical properties of graphene make it receive great attentions from academia and industry [1-12]. A structural analogue to the graphene, monolayer hexagonal boron nitride (h-BN), which has B and N atoms to substitute the honeycomb carbon network of graphene, also has attracted much research interest. Like graphene, h-BN also has the outstanding properties, such as high chemical stability, superb thermal conductivity, and mechanical strength. Some applications of h-BN have already been developed in optics and optoelectronic devices [13-24]. In addition, h-BN is used in many unique electronics applications such as a substrate for semiconductors, microwave-transparent windows because of excellent dielectric properties [18]. Several technologies have been developed and reported for the monolayer h-BN synthesis, and the single or a few layers of the h-BN have been synthesized successfully by using thermal catalytic CVD [25], hot filament chemical vapor deposition (HFCVD) [26], and sonication-centrifugation technique [19]. However, it is still very difficult to synthesize a well-defined monolayer h-BN on a large scale, which limits the study of h-BN.

h-BN has a large band gap ($E_g = 4\sim 6\text{eV}$) while the graphene has a 0 eV band

gap at Dirac points. By combining these two materials, it is expected to obtain a customized semiconductor with a band gap value as designed. The development of hybrid materials between graphene and h-BN (h-CBN) is a promising research topic. Up to now, only a few studies have been reported from experimental [27-28] and theoretical [29] viewpoints. However, the systematic studies for h-CBN have not been performed yet. In the experiments, well-defined h-CBN is still hard to synthesize. In theoretical calculation, only a limited part of the structures have been analyzed in h-CBN, such as the “carbon nanoribbon” [29] and simple “molecules” (“benzene” or “coronene”) [30]. All the published theoretical works all deal with a h-CBN monolayer. The multi-layer structures have been ignored in the previous papers.

In this chapter, a DFT calculation study of carbon-doped h-BN is presented. Some of the boron and nitrogen atoms were substituted to carbon atoms to make various carbons “molecules” embedded in hexagonal boron nitride network. Various C_x -BN structures with different carbon contents (from 0% to 100%) were examined in my calculations for investigating the relationship between the band structure and carbon content. I also investigated the structural effect from different combinations of C, B and N under the same carbon content, based on the band structure, density of states, and electron localization functions.

4.2 Calculation details

All the simulations in this work were carried out on the Quantum-Espresso programs with the version of 5.1 which is based on density-functional theory (DFT), plane wave and pseudopotentials. In my calculations, DFT was carried out with the exchange-correlation energy treated by the Perdew - Burke - Ernzerhof (PBE)

functional based on the generalized gradient approximation (GGA) [31]. The ultrasoft pseudopotentials [32] were used to describe the ionic cores, and the electron wave function was expanded in plane wave with the cut-off energy of 50 Ry for the geometry optimization and properties calculations. The mono-layered hybrid structures of C_x-BN were modeled by a 4 x 4 h-BN supercell with 32 atoms, and the double-layered hybrid structures of C_x-BN were also modeled by a 3 x 3 x 2 h-BN supercell with 36 atoms in a space group of P63/mmc [33]. More than 10Å vacuum space as periodic boundary conditions avoids interactions between layers in two neighboring cells. The atom positions were optimized until the forces on each ions converged in 0.0001 a.u. and the energy was converged in 0.00001 a.u. Brillouin zone integration was calculated as a sum over special k points of 9 x 9 x 1 (mono-layers) and 9 x 9 x 3 (double-layers) using the Monkhost- Pack scheme [34] for geometry optimization and total energy calculations. A Brillouin zone path shown in **Figure 4.1 (a)** of Γ -K-M- Γ was used for band structure computations of the mono-layer while the other Brillouin zone path of the Γ -K-M- Γ -H-K'-M'-H- Γ was used for properties calculations of the double layers shown in **Figure 4.1 (b)**. Cohesive energy [35], which was used for searching the most stable doping structures, was calculated with the following equation:

$$E_{cohesive} = \frac{N_C E_C + N_B E_B + N_N E_N - E_{C-BN}}{N_{atom}}$$

The N_C, N_B, and N_N are the numbers of the C, B, and N atoms, respectively. The E_{C-BN} is the total energy of carbon-doped structure while the E_C, E_B, and E_N are the energies of free carbon, boron, nitride atoms, respectively. The N_{atom} is the total number of atoms in the C-BN structure, and in my case, it is 32. The structure with

largest value of cohesive energy in same carbon content was the most stable structure. The most stable structure in each carbon content was used to calculate the properties unless otherwise stated.

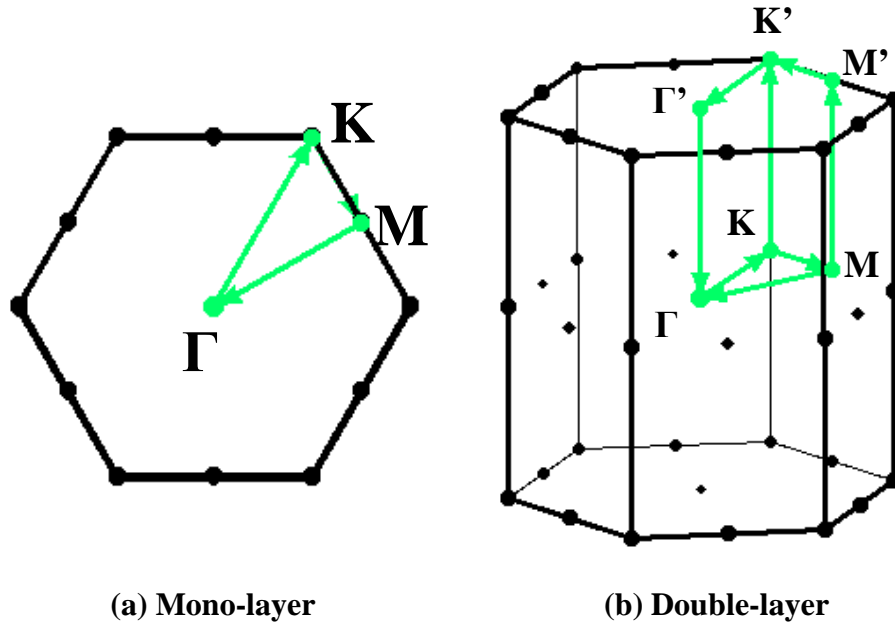


Figure 4.1 A Brillouin zone path for the band structure in hexagonal lattice (a) path of Γ -K-M- Γ used for the monolayer. (b) path of Γ -K-M- Γ - Γ' -K'-M'- Γ' used for the double layers.

4.3 Results and discussions

4.3.1 Graphene and hexagonal boron nitride monolayers (h-BN)

The structures of graphene, mono-layered hexagonal BN (h-BN) and double-layered hexagonal BN were calculated and optimized to check the correctness of my calculation. The geometric parameters of the optimized structures of mono-layer hexagonal BN and the graphene are listed in **Table 4.1** and **Figure 4.2**. From **Table 4.1**, the calculated C-C bonding length in graphene is 1.419 Å, which is

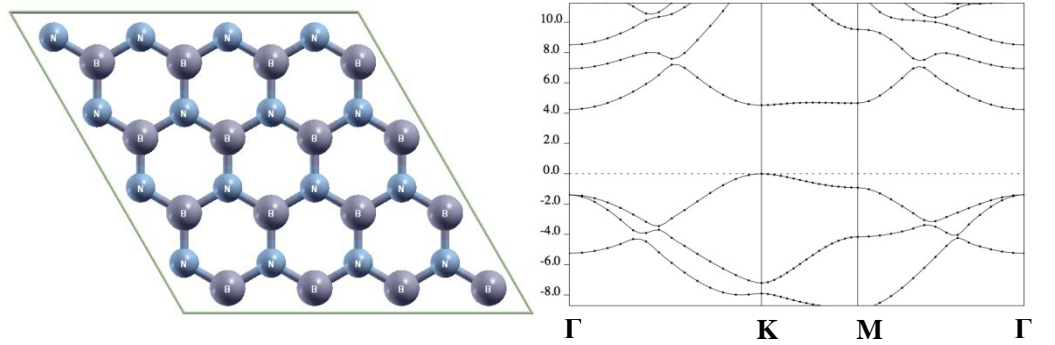
consistent to the reported result of 1.420 Å [35]. The calculated B-N bonding length with the value of 1.448 Å also shows the high consistency to reported results of 1.45 Å [29]. The cohesive energies of graphene and mono-layered h-BN are 8.98eV and 8.56eV, respectively. These values are consistent with the previous report [29] and proved the high stability of graphene and h-BN. Furthermore, the band structure of graphene and h-BN were calculated and are shown in **Figure 4.2 (a)** and **(b)**. The calculated band gap of mono-layer h-BN is 4.17eV, which is in agreement to the earlier reports [29]. In addition, the band structure of graphene also agrees well with the published results [1-12] with a contact point at Fermi level which is located at high symmetry K-point. In summary, the calculated result of graphene and h-BN fitted well to earlier reports which proved the accuracy of my calculations.

Table 4.1 Geometric Parameters and band gaps of hexagonal boron nitride and graphene calculated in this work, including the results in previous reports of experiment and theory

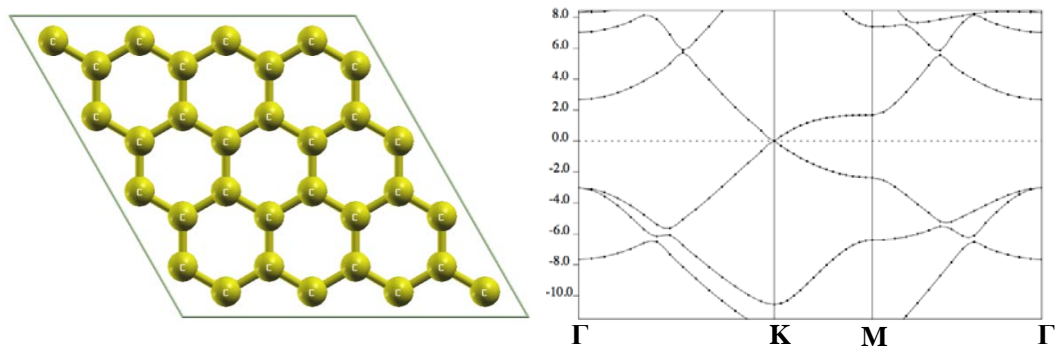
		C-C or B-N(Å)	Band gap (eV)
Graphene	this work	1.419	0
	Experimental ¹	1.420	0
	Theoretical ²	1.420	0
h-BN	this work	1.448	4.23
	Experimental ¹	1.450	4.1~6
	Theoretical ²	1.443	4.20

1. Reference 35

2. Reference 29



(a) Optimized structure of mono-layer hexagonal BN and its band structure



(b) Optimized structure of graphene and its band structure

Figure 4.2 (a) Hexagonal BN and (b) Graphene and their band structures

4.3.2 Mono-layer Carbon doped hexagonal BN nanosheet

4.3.2.1 h-BN doped with two carbon atoms

Many doping structures in atomic scales can exist even if we fix the content of carbon atoms in h-BN. I used a 32-atoms cell and changed the carbon number X doped into the cell. First I examined the case of $X = 2$ to find the most stable structures in the given carbon content. In this $\text{h-C}_2(\text{BN})_{15}$ structures, I optimized three structures which are shown in **Figure 4.3**: (a) two doped carbon atoms bonding

together, **(b)** and **(c)** carbon atoms separately doped structure with different distances.

The optimized geometry, cohesive energy and band gap are exhibited in **Table 4.2**.

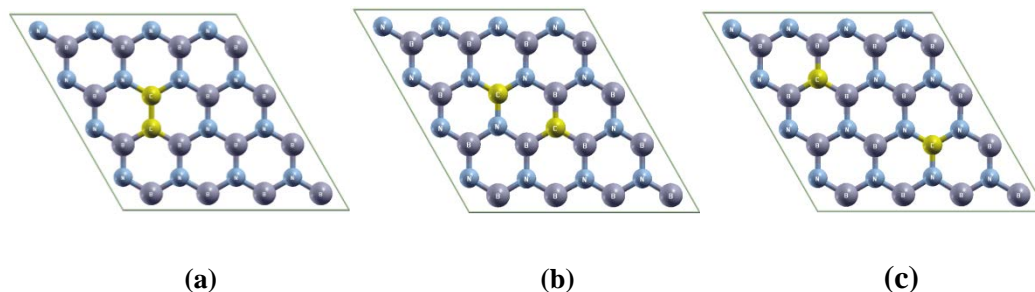


Figure 4.3 The 2/32 carbon content h-CBN. **(a)** Doping carbon atoms bonding together. **(b)** and **(c)** are the structures with carbon atoms separately doping structure with different distances.

Table 4.2 The geometrical parameters and cohesive energy of the three 2/32-carbon doping structure in Figure 4.3.

Structure	C-C bonds	C-N bonds	C-B bonds	Neighboring B-N bonds	Cohesive energy
(a)	1.36Å	1.38Å	1.47Å	1.45	8.53eV/atom
(b)	-	1.36Å	1.44Å	1.46	8.49eV/atom
(c)	-	1.35Å	1.44Å	1.46	8.46eV/atom

In **Figure 4.3 (a)**, the doped two carbon atoms formed four C-N, C-B bonds with the neighboring boron and nitrogen atoms, the bond lengths are 1.38 Å and 1.47 Å, respectively. C-C bond has the smallest bond length in these three with the value of 1.36 Å which means the C-C bonds probably formed double bonds (1.34 Å [36]) . In **Figure 4.3 (b)**, there are three C-N bonds and three C-B bonds with the average bond

length of 1.36 Å and 1.44 Å, respectively. In **Figure 4.3 (c)**, there are also three C-N bonds and three C-B bonds but with a different average bond length of 1.35 Å and 1.44 Å. In **Table 4.2**, the bond length of C-B and C-N is getting smaller from 1.47 Å to 1.44 Å of C-B bonds and 1.38 Å to 1.35 Å of C-N bonds, which indicated that carbon atoms in the structure **(a)** are more separated from the BN network than those of structures **(b)** and **(c)**. It leads to an electron distributions around carbon more localized in the structure **(a)**. In the structure **(b)**, the B and N which are in the same six membered ring with doped carbon have totally different B-N bond length compared to the other B-N. This is because doping of the carbon atom changed the electron density distribution in its surroundings, one unpaired electron belonging to the $2p_z$ -orbital of the doped carbon is dispersed into the nearby six-membered rings. Furthermore in the structure **(c)**, the above effect from the doped carbon was enhanced. The delocalization of electron caused the increase of the B-N bond length.

The separately doped structure of **(b)** and **(c)** make B-N bonds more unstable or activated than those in the structure **(a)** which will greatly affect the stability of the whole h-CBN structures. The structure **(a)** has the minimum number of C-B and C-N bonds and have the largest cohesive energy (8.53 eV/atom compared to 8.49 and 8.46 eV/atoms). This result is in agreement of the earlier study [29] of the minimum number of C-B and C-N bonds lead to a stable structure. It is noted that the energy difference is rather small even compared with the thermal energy at room temperatures. All of the three structures may exist when the material is synthesized by high energy processes.

Based on the stability analysis shown above for the 2/32 carbon content, we can expect that the most stable structure has the minimal number of C-B, C-N bonds

or maximum number of C-C bonds. This condition leads to carbon “molecules” embedded in h-BN as the stable structures. In the next sections, I studied the structures satisfying this condition.

4.3.2.2 h-C_X (BN)_{16-X/2} structure with low carbon content (X= 2, 4, 6)

I optimized all the structures with minimum C-B and C-N bonds with different carbon contents. First, I will discuss the low carbon content structures. **Figure 4.4** shows the optimized structure with the doped carbon numbers of 2, 4, and 6.

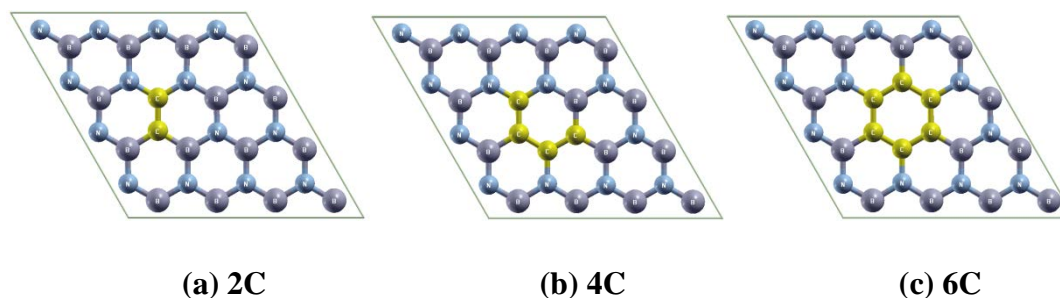


Figure 4.4 Optimized h-CBN structure with low carbon content (X=2, 4, 6, labeled as “XC” in the figure) doping structure. (a) is the same as the **Figure 4.3 (a)** with X=2 / 32 carbon content. (b) X=4. (c) X=6.

Table 4.3 The geometry information, cohesive energy and band gaps of low carbon content doping structures (2/32, 4/32, 6/32)

	Carbon content	C-C bonds	C-N bonds	C-B bonds	Cohesive energy	Band gap
(a)	2/32	1.36Å	1.38Å	1.47Å	8.52eV/atom	3.51eV
(b)	4/32	1.38Å	1.38Å	1.46Å	7.02eV/atom	2.92eV
(c)	6/32	1.41Å	1.42Å	1.50Å	8.47eV/atom	3.23eV

The geometry information, cohesive energy, and band gaps are listed in Table 4.3. **(b)** 4C structures has a smallest band gap with the value of the 2.92 eV in these three doping structure. However, the smallest cohesive energy (7.02eV/atom) of 4C indicated 4C structure is unstable. The 2C and 6C doping structures, had a higher cohesive energies (8.52eV/atom, 8.47eV/atom) than 4C which means they are more stable than 4C. This makes an interesting contrast with hydrocarbon molecules because cis-butadiene is not a very unstable molecule compared with ethylene and benzene.

All the geometrical information of the three structures including the average bond length of C-C, C-B and C-N are shown in **Table 4.3**. Based on the geometrical information, I noticed that the geometrical structure of the carbon doped h-BN changed following a certain way: The C-C bonds length increase and the C-N, C-B bonds length decrease with the carbon content increase. In **(a)** 2C structure, bond length is 1.35 Å which is classified as double bonds with strong interaction between two doped carbon atoms. However in **(b)** 4C structures, the average bond length of C-C had increased to 1.38 Å. The C-C bonds of **(c)** 6C all had same length of 1.41 Å. The increase of C-C bonds length can be explained by the different size of π -electron systems located at the doping carbon system. In 2C case, C-C bonds formed as a double bonds. In 4C case, the C-C bond lengths have different length of 1.36 Å, 1.38Å, and 1.41Å (average bond length is 1.38 Å). It means that these three C-C bonds do not form a unified π -bond which extends over the C-C bonds. In 6C case, the same bond length of all the C-C bonds means the conjugated π -electron structure is extended over the whole carbon system. Furthermore, the C-C bond length (1.41Å) is close to those in graphene (1.42 Å), which suggests that the electronic

structure of the six carbon atoms are similar to that of graphene. The bond length of C-N and C-B shown in **Table 4.3** increased from 1.38Å and 1.47Å to 1.42Å and 1.50Å, respectively, which indicated that the doped carbon structures became more “independent” from the BN network structure.

I expected that the conjugated π -electrons located on doped carbon structures would contribute the narrowing of the band gap. In order to investigate the electronic effect from doped carbon atoms, I calculated the band structure and density of states (DOS), including the partly density of states (PDOS) of the three low carbon content doping structure. The calculated band structures are shown in **Figure 4.5**, DOS and PDOS of doped carbon were shown **Figure 4.6** and the band gaps had been listed in **Table 4.3**. It should be noted that the band structures exhibit substantial band dispersion (0.5 ~ 1 eV) in the HOMO and LUMO levels although the carbon clusters are separated by the surrounding BN lattice. This is a striking difference from hydrocarbon system in the vacuum, in which separated molecules will not interact and very flat bands will be observed.

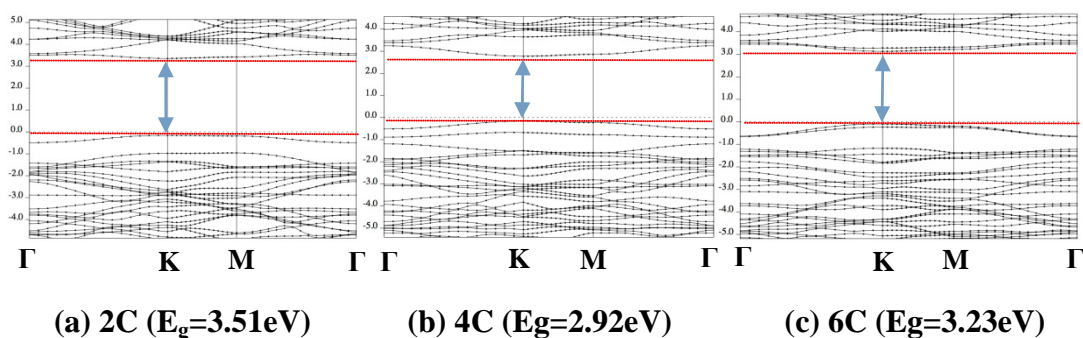


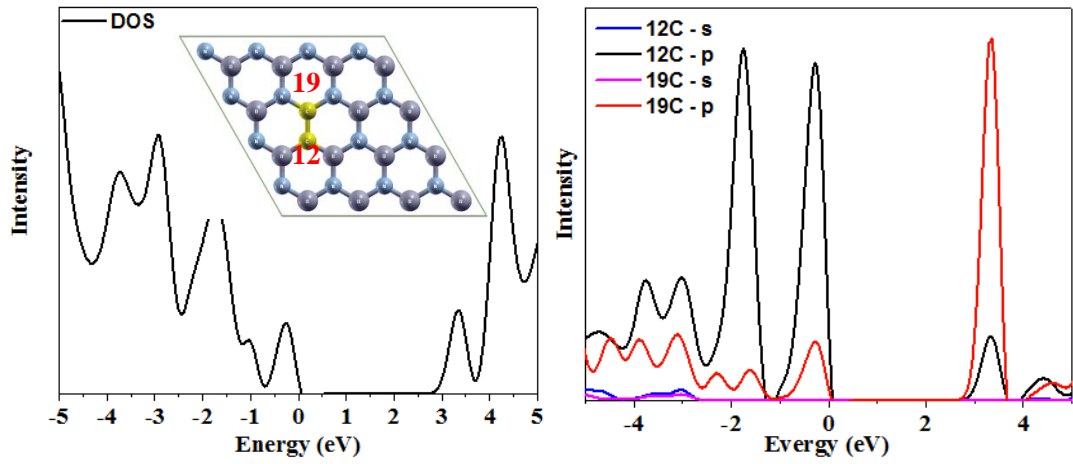
Figure 4.5 The band structure of the low carbon content doping structures of 2C, 4C and 6C. (a) 2/32 carbon content doping structure. (b) 4/32 carbon content doping structure. (c) 6/32 carbon content doping structure.

In the band structures shown in **Figure 4.5**, after the carbon doping, the electronic states of all the three carbon-doped structures had significant changes near the Fermi level with a closing band gap. It means the doped carbon had greatly affected the band structure and the carbon content determined the degree of narrowing band gaps. I noticed that these are direct band gap materials with the smallest gaps located at the K-point. Other reported theoretical studies of carbon doped h-BN with different structures also presented similar direct gap nature located at K-point [29]. I speculate that this is the common feature of carbon doped h-BN.

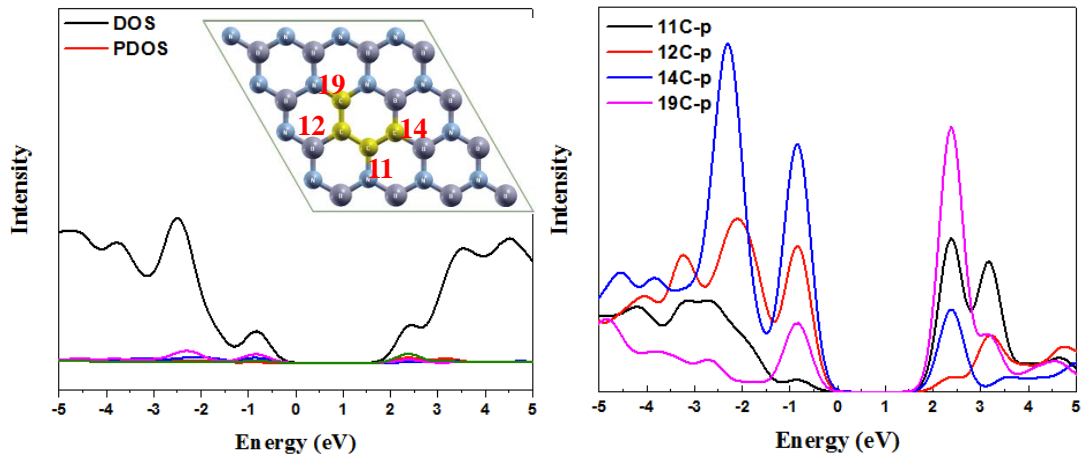
The band gap of 2C, 4C, and 6C doping structure are 3.51eV, 2.92eV and 3.23eV, respectively. The 4C doping structure had the smallest band gap among these three. However, 4C doping structure is the most unstable with the smallest cohesive energy of 7.02eV/atoms. In order to investigate the electronic structure in each carbon atom, PDOS was calculated.

In the **Figure 4.6** of the DOS and carbon PDOS results, the most part of the highest occupied molecular orbitals (HOMO) and the lowest occupied molecular orbitals (LUMO) comes from doped carbon atoms. In 2C (**Figure 4.6(a)**), the two doped carbon atoms have highly-symmetric (anti-symmetric) PDOS near the HOMO and LUMO. The carbon PDOS figure shows that just the p-orbital of the doped carbons contributed to the HOMO and LUMO.

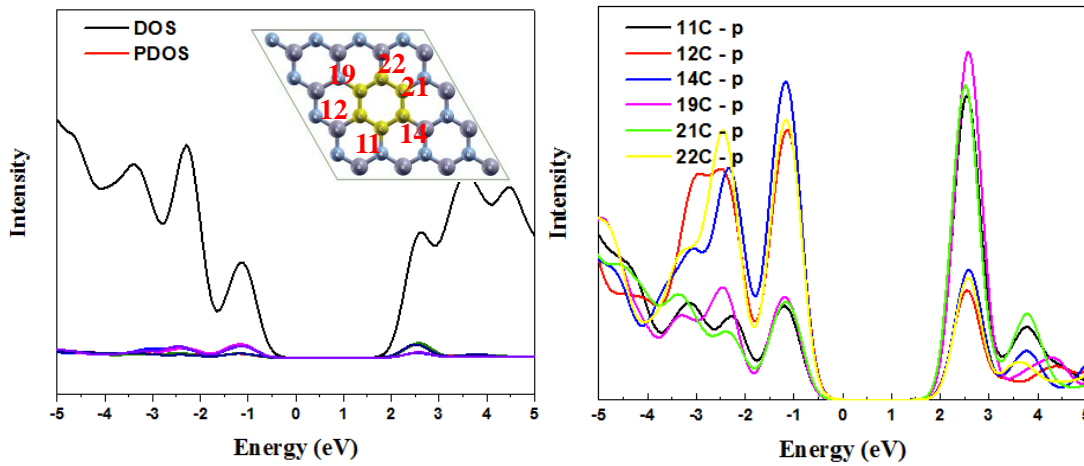
In 4C (**Figure 4.6 (b)**), the PDOS of carbon atoms are very different from each other without any symmetry with means these carbon atoms are in different electronic states. This is the striking difference from ordinary cis-butadiene molecule and probably from the contribution of surrounding B and N atoms. It is consistent with the analysis described above that the carbon bonds in 4C are different.



(a) DOS and PDOS of the 2C doping structure



(b) DOS and PDOS of the 4C doping structure



(c) DOS and PDOS of the 6C doping structure

Figure 4.6 The DOS and PDOS of carbon content h-BN with the value of (a) 2/32, (b) 4/32, (c) 6/32.

In 6C (**Fig. 4.6 (c)**), the PDOS of carbon atoms have two types. They correspond to C bonded to a B atom and C bonded to an N atom. Nevertheless, all C atoms contribute to HOMO and LUMO. This indicates that an extended π -electron conjugated structure is formed with covering whole doping carbon atoms.

4.3.2.3 Monolayer h-BN with high carbon content

Doping four carbon atoms to h-BN resulted in an unstable structure. Therefore in this section we start from the 6C and add “benzene” rings to increasing the carbon content. I optimized the carbon doped h-BN monolayer with the carbon content from the 6/32 to the 22/32 shown in **Figure 4.7**.

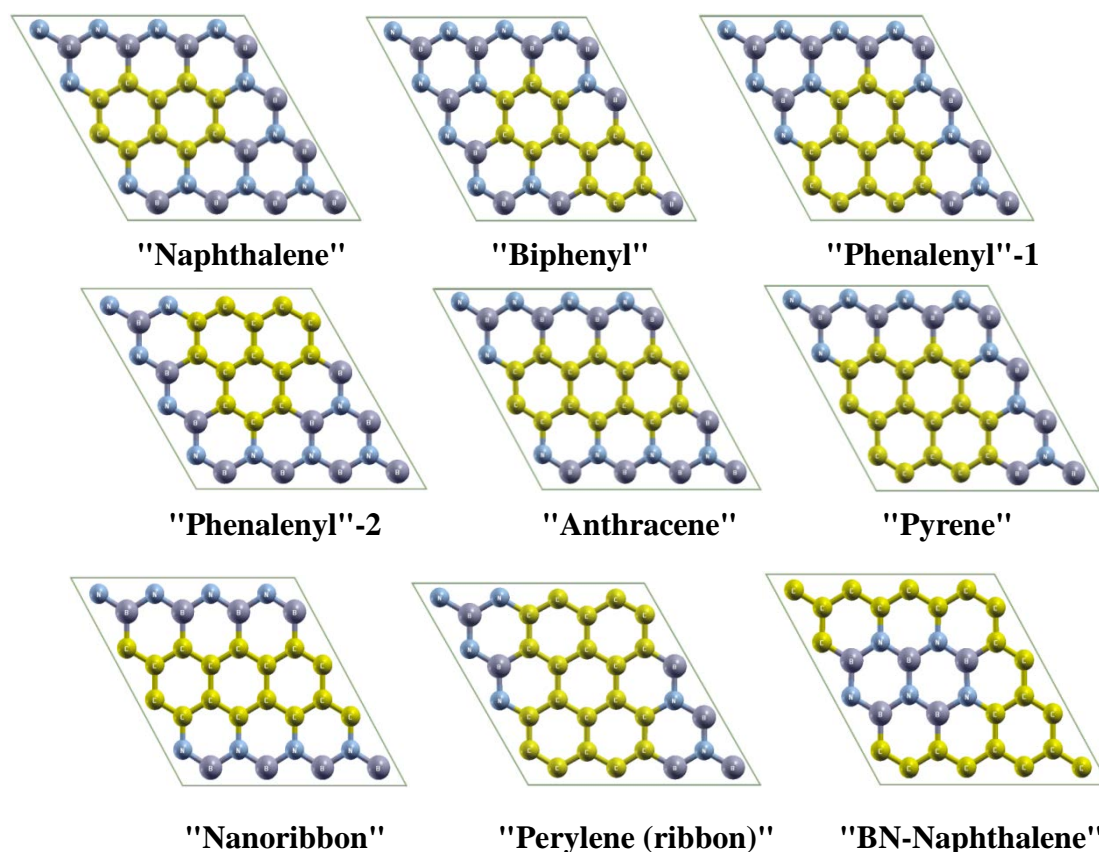


Figure 4.7 The optimized structure of high carbon content h-BN monolayer. Names of hydrocarbon molecules in analogy are indicated beneath the figures.

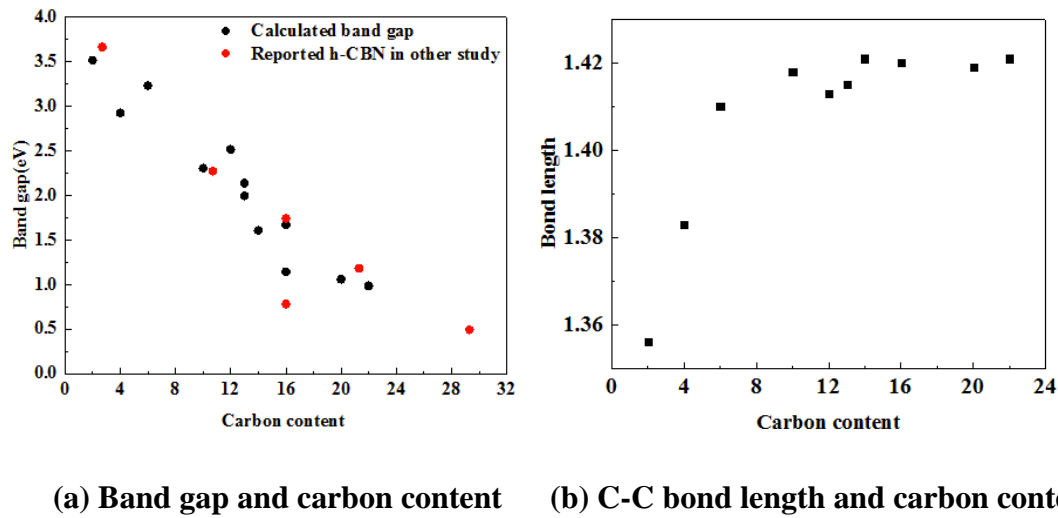


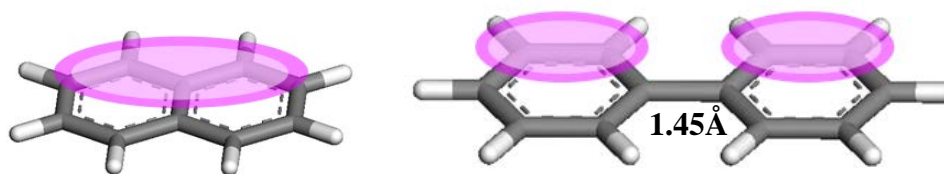
Figure 4.8 The relationship of carbon content to the band gap and C-C bond length. **(a)** The relationship of carbon content to the band gap. **(b)** The relationship of carbon content to the C-C bond length.

The relationships between the carbon content and the bond length and the relationship between the carbon content and band gap are shown in **Figure 4.8 (a)** and **(b)**, respectively. In **Figure 4.8 (a)**, the band gaps obtained a significant decrease from the 3.23 eV of 6C (“benzene”) (**Figure 4.4 (c)**) to the 0.983 eV of “BN-Naphthalene” shown in **Figure 4.7**, which is a smaller value of band gap than bulk silicon (1.17 eV). This result propose a theoretical possibility of replacing the silicon in some applications in which band gap values are important. Furthermore, these carbon- doped h-BN structures had direct band gap, which would be an advantage for optical applications by comparing with the bulk silicon. With carbon content increasing, the band gap keeps decreasing, which means the electronic structure of carbon-doped ones became close to the graphene with the carbon content increase. The relationship between carbon content and C-C bond length shows the

same tendency as shown in **Figure 4.8 (b)**. With the carbon content increase, the C-C bond length increase and keep stable around 1.42 Å that is the same as graphene. The carbon content played an important role in adjusting the band gap of the carbon doped h-BN. However, the large carbon content such as 22/32 with the band gap of 0.983 eV, have the large carbon area in the whole nanosheet, which make the doping structure might suffer from the oxidation problem like graphene.

4.3.2.4 “Naphthalene” and “Biphenyl” doping structure

As I discussed above, the different carbon doping structure can greatly affect the band structure. In this section, I will choose some of the carbon structures doped in h-BN for detailed discussion to explain the effect. One is “naphthalene” (**Figure 4.7, Figure 4.9 (a)**), with 10 C atoms, its band structure showed a direct band gap located at K-point with the value of 2.13eV. The other is “biphenyl” (**Figure 4.7, Figure 4.9 (b)**), with 12 C atoms, the band gap was also located at K-point with a direct band gap, but the value increased to 2.53eV. The band gap increased with the carbon content increased, which is opposite to the general tendency. In the “biphenyl” case, the only C-C bond which connected two “benzene rings” had a large length with the value of 1.45 Å, which means there is little interaction between two large π -electron structures (**Figure 4.9 (b)**). The geometrical parameters analysis shows that every single “benzene ring” had a very similar C-C bond length to the 6C structure (**Figure 4.4 (c)**) with an average value of 1.41 Å. The average C-B bond length and average C-N bond length also are similar to the 6C structure (**Figure 4.4 (c)**) with the value of 1.50 Å to C-B, 1.41 Å to C-N, respectively.



(a) “naphthalene” doping structure

(b) “biphenyl” doping structure

Figure 4.9 The delocalized conjugated π system of the two doping structures (a) “naphthalene” had a large delocalized conjugated π system. (b) “biphenyl” had two separated delocalized conjugated π systems.

On the other hand, in “naphthalene”, a larger π -electron structure was located on the two neighbored “benzene rings”. These differences between “biphenyl” and “naphthalene” are similar to their hydrocarbon analogues.

4.3.2.5 Different doping structure with the same carbon content

The doping structure and the carbon content both can affect the band structure of carbon doped h-BN [29-30]. Further evidence for this issue is supplied by comparing "Pyrene", "Nanoribbon" and "BN-Nanoribbon", "Nanoribbon-larger size", the former two are calculated for the first time in this work, shown in **Figure 4.10**. All of them had the same carbon content of 50%. In **Figure 4.10 (a)** of "BN-Nanoribbon", doping carbon atoms were separated by a BN nanoribbon. **Figure 4.10 (b)** of "Pyrene" also had separated carbon atoms by a half size BN nanoribbon. In **Figure 4.10 (c)**, a narrow carbon nanoribbon have been doped into the h-BN, and finally, in **Figure 4.10 (d)**, a broader carbon nanoribbon doped into the h-BN. The calculated band gaps of these structures were 1.74eV, 1.67eV, 1.61eV, and

0.78eV, which have been marked in **Figure 4.8(a)** at the ordinate value of X=16.

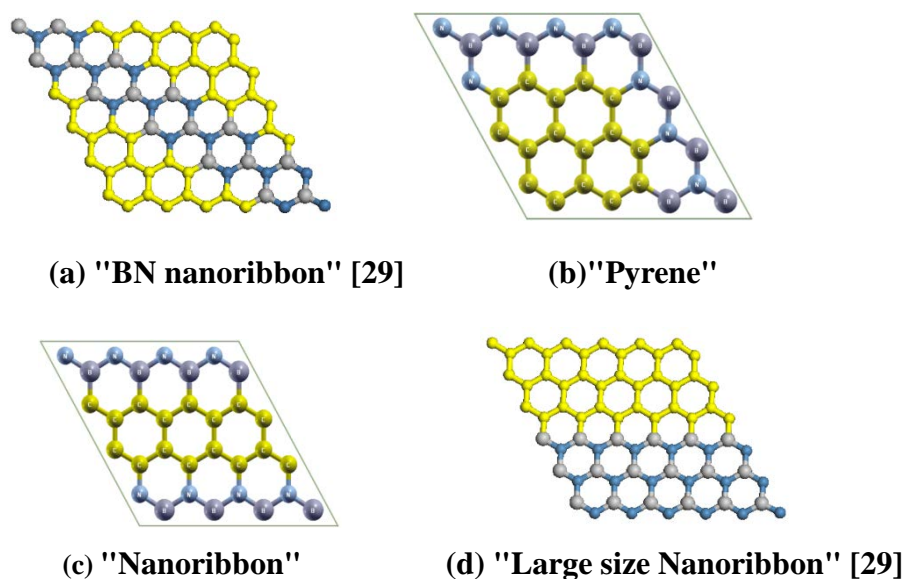


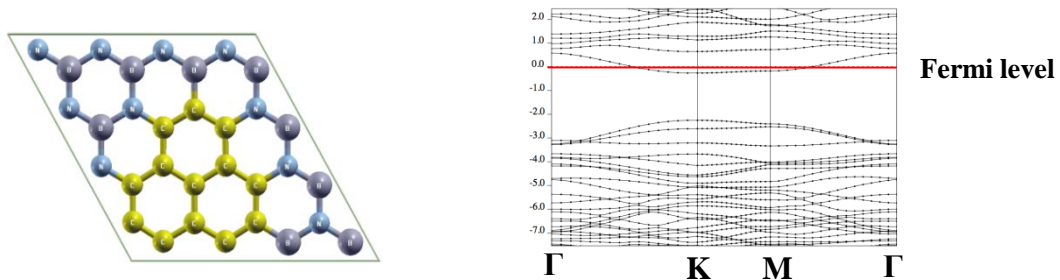
Figure 4.10 Four different carbon-doped BN structure. (a) "BN ribbon"[29] with the band gap of 1.74eV, (b) "Pyrene" with the band gap of 1.67eV, (c) "Nanoribbon" with the band gap of 1.14eV, (d) "Large size Nanoribbon" [29] with the band gap of 0.78eV.

When the carbon atoms were separately doped into h-BN as in Fig. 4.10 (a) and (b), the structures have large band gaps (1.74 and 1.67 eV, respectively). On the other hand, if the carbon atoms are connected in one dimension as a carbon nanoribbon as in **Figure 4.10** (c) and (d), the structures show smaller band gaps (1.14 and 0.78 eV, respectively). Increasing the width of the carbon nanoribbon also can decrease the band gaps. This result is also a consequence of the delocalization of the conjugated π system. This result shows similar tendency with the analysis above about "Naphthalene" and "Biphenyl". The size of the delocalized π -conjugated system is the key factor to influence the electronic structures of the carbon-doped

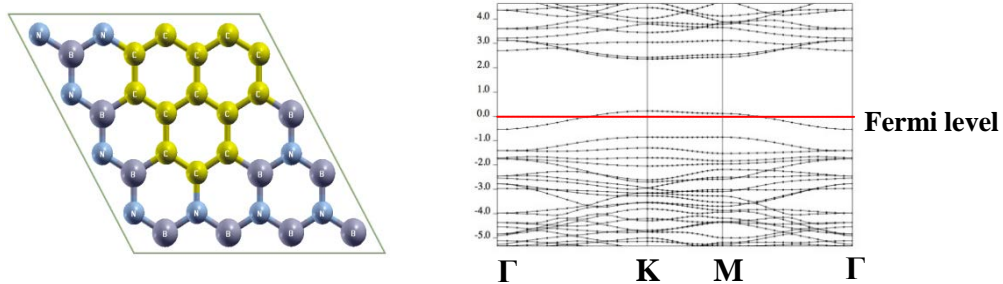
h-BN.

4.3.2.6 Odd-number carbons: study of two kinds of "Phenalenyli"

I studied the effect of doping odd number of carbon atoms. There are two possibilities in the stoichiometry of the doped structures for odd number carbons: B-rich or N-rich. I compared the B-rich and N-rich "Phenalenyli" structures and found an interesting result about the band structures. The two kinds of "Phenalenyli" structures and their band structures have shown in the **Figure 4.11**.



(a) The optimized "N-rich phenalenyli" structure and its band structure



(b) The optimized "B-rich phenalenyli" structure and its band structure

Figure 4.11 The "Phenalenyli" doped BN structure and their band structure. (a) "N-rich phenalenyli", 7 boron atoms and 6 nitrogen atoms were replaced by carbon atoms. (b) "B-rich phenalenyli", 6 boron atoms and 7 nitrogen atoms were replaced by carbon atoms.

In the **Figure 4.11(a)** and **(b)**, I noticed that the band structures of both "N-rich

phenalenyl" and "B-rich phenalenyl" had one energy level crossing the Fermi level. In "N-rich phenalenyl", LUMO (conduction band) crossed the Fermi level while in "B-rich phenalenyl", HOMO (valence band) crossed the Fermi level. In other words, "N-rich phenalenyl" and "B-rich phenalenyl" are n-type and p-type, respectively. Both of them are metallic.

These unique band structures can be understood as follows. In pristine h-BN, empty p_z -orbitals of B atoms make conduction band (LUMO) while filled p_z -orbitals of N atoms make valence bands. A carbon atom has one electron more than a B atom and one electron less than a N atom. When one more B atom is replaced by a C atom in "N-rich phenalenyl", one electron will be left in the conduction band to make "n-type" band structure. The opposite reasoning is applied for "B-rich phenalenyl", in which one more N atom is replaced by a C atom, to make "p-type" band structure.

The atomic orbital expansions of the HOMO and LUMO bands were analyzed and shown in **Figure 4.12**. The upper panel of **Figure 4.12** shows the (a) HOMO and (b) LUMO of "N-rich phenalenyl". The LUMO band, which crossed the Fermi level, was almost localized at C, N atoms except for the C-N bonds. The LUMO figure indicated that the effect from free electrons supplied by C atoms was dispersed into the carbon and nitrogen atoms. HOMO band of "N-rich phenalenyl" was localized among the whole p_z -orbitals of C atoms and contributions from surrounding B and N are small.

The lower panel of **Figure 4.12** shows the (c) HOMO and (d) LUMO of "B-rich phenalenyl". Unlike the "N-rich phenalenyl", the HOMO band of "B-rich phenalenyl", which crossed the Fermi level, was almost come from the π -bonds

between outermost C and surrounding B atoms. B atoms in pristine h-BN usually bonded with nearest three N atoms with σ -bonds and without π -bonds. When an N atom is replaced by a C atom, because the energy of p_z -orbital of C atom is lower than that of N atom, and one electron from C will become delocalized among outermost C and surrounding B atoms. The fact that C-B bond length is the longest can be explained in this scheme. On the other hand, LUMO is localized among C atoms.

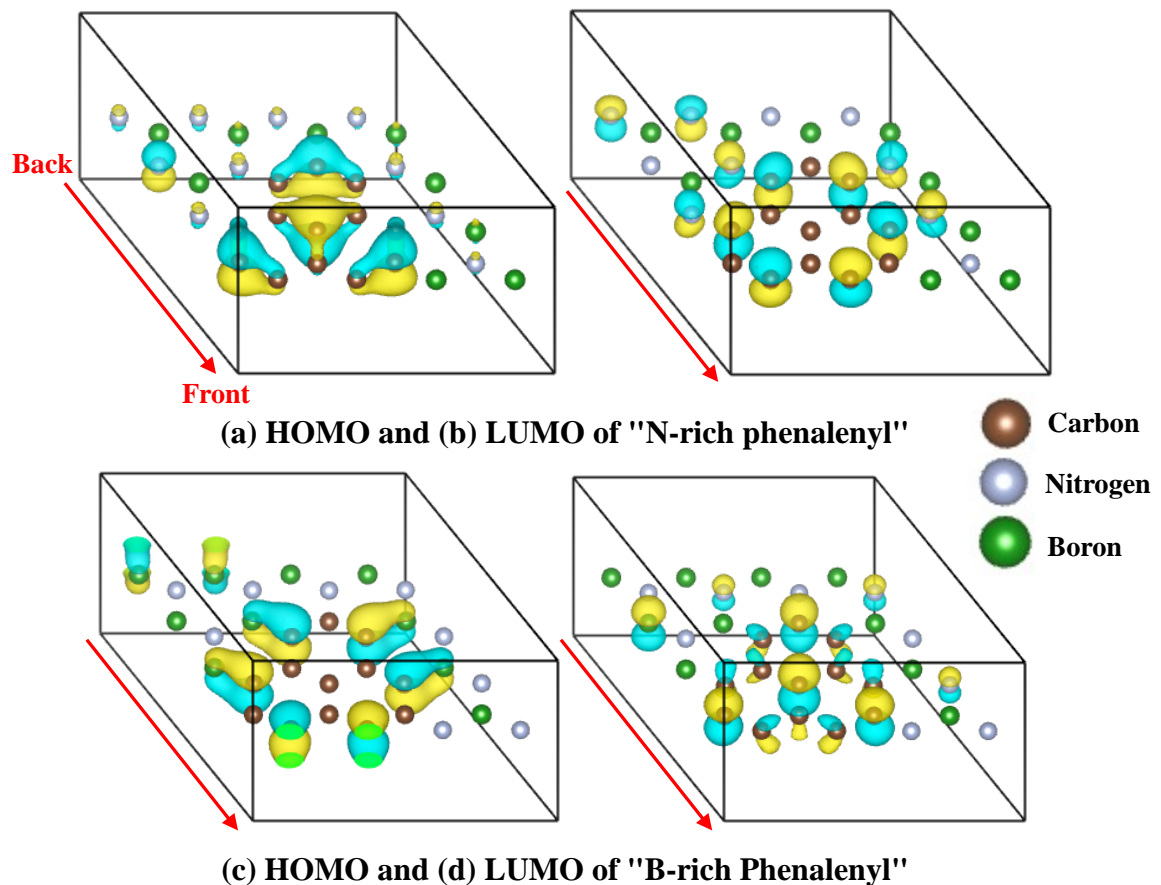


Figure 4.12 The atomic orbitals of the HOMO and LUMO for "Phenalenyl" doping structure. The red arrow clarity the direction of the cell from back to front.

The electronic structures of these "Phenalenyl" doping h-BN structure were

analyzed further by using the total DOS as shown in **Figure 4.13**. A DOS peak crossed Fermi level. HOMO and LUMO are denoted in the figure for the clarity. HOMO and LUMO were mainly contributed by the p_z -orbital of carbon as discussed above.

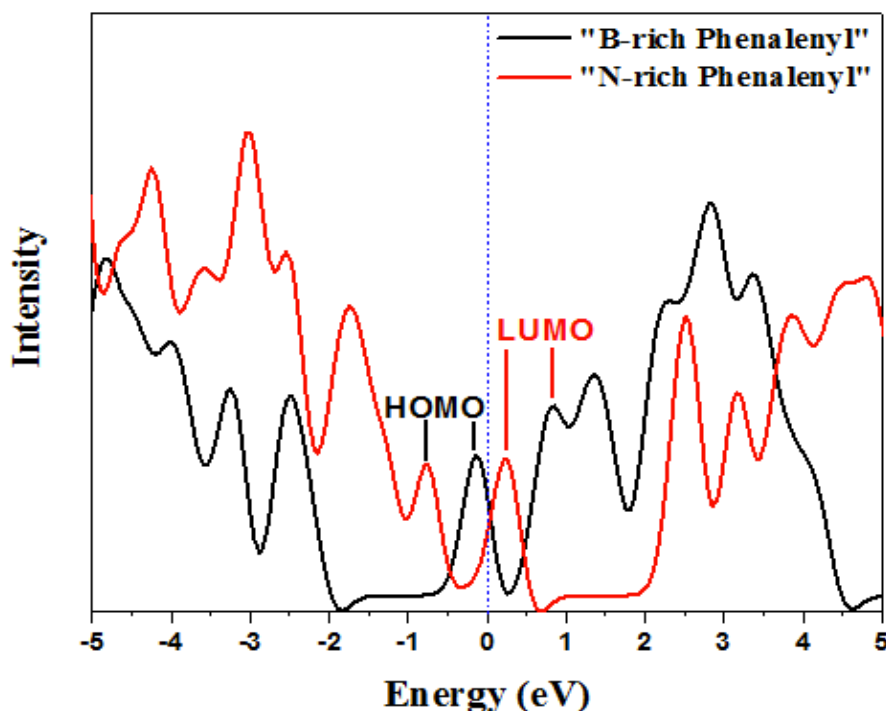


Figure 4.13 The DOS of the "B-rich Phenalenyl" (black curve) and "N-rich phenalenyl"(red curve).

4.3.3 Double-layered carbon doped structure

4.3.3.1 The double-layered h-BN

Replacing different atoms of h-BN can lead to the carbon doped h-BN with totally different types band structures. As I discussed in the previous section, "N-rich Phenalenyl" (**Figure 4.11(a)(b)**) and "B-rich Phenalenyl" (**Figure 4.11(c)(d)**), that were doped with odd numbered carbon atoms, exhibited the metallic properties.

It should be noted that the Fermi energies are located on HOMO band or LUMO band depending upon which of N or B are replaced more by C atoms. Since the energy levels of HOMO and LUMO bands are much different, the work functions of these metals are different. These results have made me to consider the behavior when these N-rich and B-rich metallic layers are stacked. It will open a way to obtain small band gap semiconductors which will be important in applications such as in solar cells. In this section, I will describe the computational results and analysis of double layers of odd-number C-doped h-BN.

Although a few theoretical studies on h-CBN have been reported, no literatures can be found on multilayered h-CBN, to the best of my knowledge. It is probably because the layers are considered to be weakly bound by van der Waals forces and strong electronic modification is not expected. Since the layers have unpaired electrons when odd numbers of C atoms are doped, strong interactions can be expected.

I combined a N-rich layer and a B-rich layer to make a double layer for the DFT calculations. Based on the simulations results, the double-layered h-CBN structures can be divided into three types: (i) all the doped C atoms shifted out of layers to get close to each other (ii) some of the C atoms deviated from the layers (iii) C and B atoms deviated from the layers with significant changes from the monolayer structures. In next three sections, I will discuss the interlayer interaction in these three types of h-CBN structures.

4.3.3.2 Double-layered h-CBN, type (i)

Figure 4.14 shows the h-CBN double layers with strong interaction (type (i)).

They are shown after the structure optimization. The two structures in the figure have different carbon content of (a) 2/36, (b) 6/36, which are named (a) 2C-i, and (b) 6C-i, where “i” stands for type (i). Note that the numbers are that of carbon in two layers. It is noticed that the interlayer C-C distance is closer than the separation of the layers (3.30 - 3.50 Å [37-42], my result is $3.40 \pm 0.02 \text{ \AA}$, the interlayer distances in graphite is 3.33-3.35 Å [43-45]). The shortest interlayer C-C distance in 2C-i, 6C-i have 1.67 Å and 1.47 Å, respectively. I calculated the electronic structure of the optimized structures.

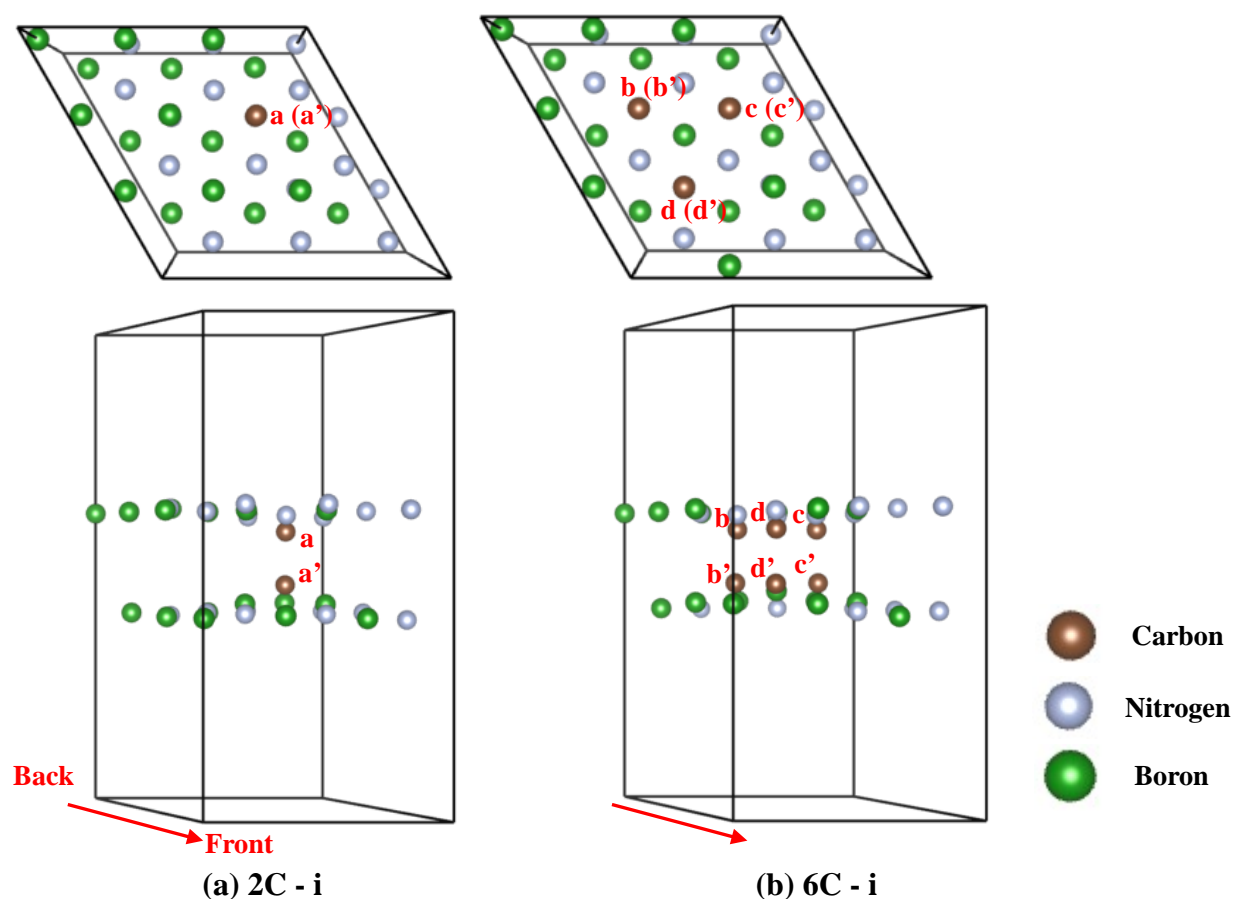


Figure 4.14 The optimized double-layered structures shown from the top view (first line) and from side view (second line). (a) 2C - i, (c) 6C - i.

The band gaps are 3.75 eV and 3.25 eV, respectively. In these structures, we can observe the general tendency of decreased band gaps by increasing carbon content, but the decrease is slower than in the mono-layer cases (**Figure 4.8 (a)**). The band structures shown in **Figure 4.15** also had a great difference from the mono-layered structures. The band structures of 6C-i shown in **Figure 4.15 (b)** still has direct band gap while the band structure of 2C-i shown in **Figure 4.15 (a)** has a indirect band gap. 2C - i and 6C - i are not metallic because neither of the two structures have the energy levels (HOMO or LUMO) crossing the Fermi level. This result means that by stacking the two kinds of metallic layers (B-rich h-CBN layer and N-rich h-CBN layer, discussed in section 4.3.2.6), the free electrons will pair together.

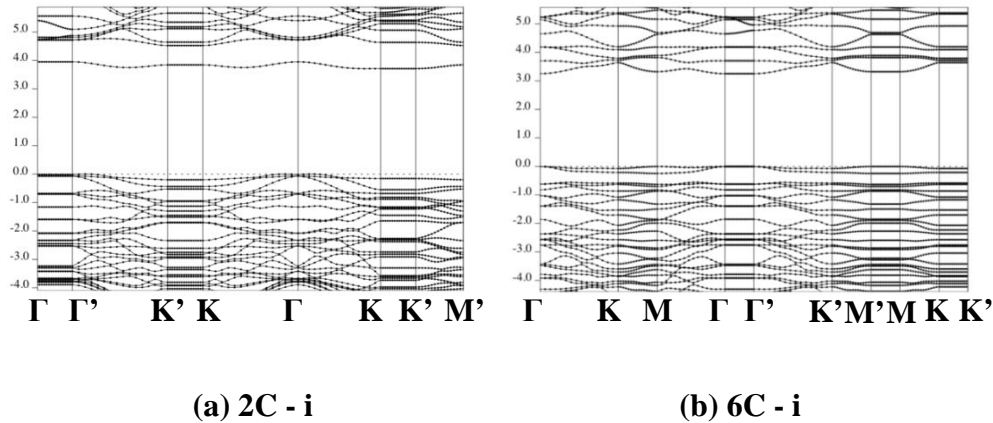


Figure 4.15 The band structure. (a) 2C - i with indirect band gap, the band gap is 3.75 eV. (b) 6C - i with direct band gap, the gap location was shifted to Γ -point, the band gap is 3.25 eV.

In order to investigate the distributions of electrons, especially the free electrons, electron localization function (ELF) figure was calculated. The ELF figure of the 2C - i is shown in **Figure 4.16**. The two C atoms have different electron

distribution around them. In the bottom layer (B-rich layer), the carbon atom shows similar ELF distribution to surrounding N atoms. The counterpart situation is observed in the top layer: the doped carbon had the same ELF distribution as B atoms. A large ELF cloud can clearly be observed between two doped carbons along the C-C direction (**Figure. 4.16**). It is the typical electron distributions in σ -bonds, which means that in this structure 2C-i the carbon atoms exist as sp^3 carbon.

In 2C-i, both doped C atoms have a single electron at first. These single electrons are active and they can easily bond together. In N and B cases of the pristine h-BN, all the electrons around N and B atoms have paired, which means that they are stable and they would not form sp^3 bonds spontaneously. It should be noted that the B and N in h-BN can be rearranged to form the sp^3 bonds during the transformation from h-BN to c-BN (cubic-BN, similar with diamond) under extreme conditions [46].

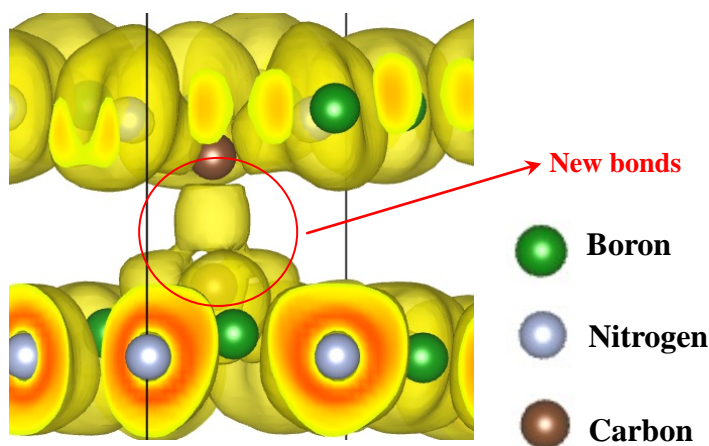


Figure 4.16 The electron localization functional figure (ELF) of the 2C - i. The two doping carbon atoms shifted from their layers and get close. The ELF cloud can be observed between these two doping carbon along the C-C direction which means the C-C bonds formed and it is the σ -bonds.

Figure 4.17 (a) and **(b)** exhibit the HOMO and LUMO of 2C-i structure, respectively. HOMO of 2C-i is located on N atoms. LUMO is mainly located on the B atoms while a small part is located on C atoms. The HOMO and LUMO are almost contributed by B and N atoms near the C atoms. It means that the C atoms change the electronic structure of neighboring B and N atoms, and make them more active than other B and N atoms which are far away. In the monolayers HOMO and LUMO are located on the C atoms, while in type (i) the contribution of C atoms is weak. This result can be explained by considering that the sp^3 carbon atoms have more stable electronic structures. In this double-layered h-CBN, the B and N atoms will act as electron acceptors and donors, which might make this material attractive as catalysts.

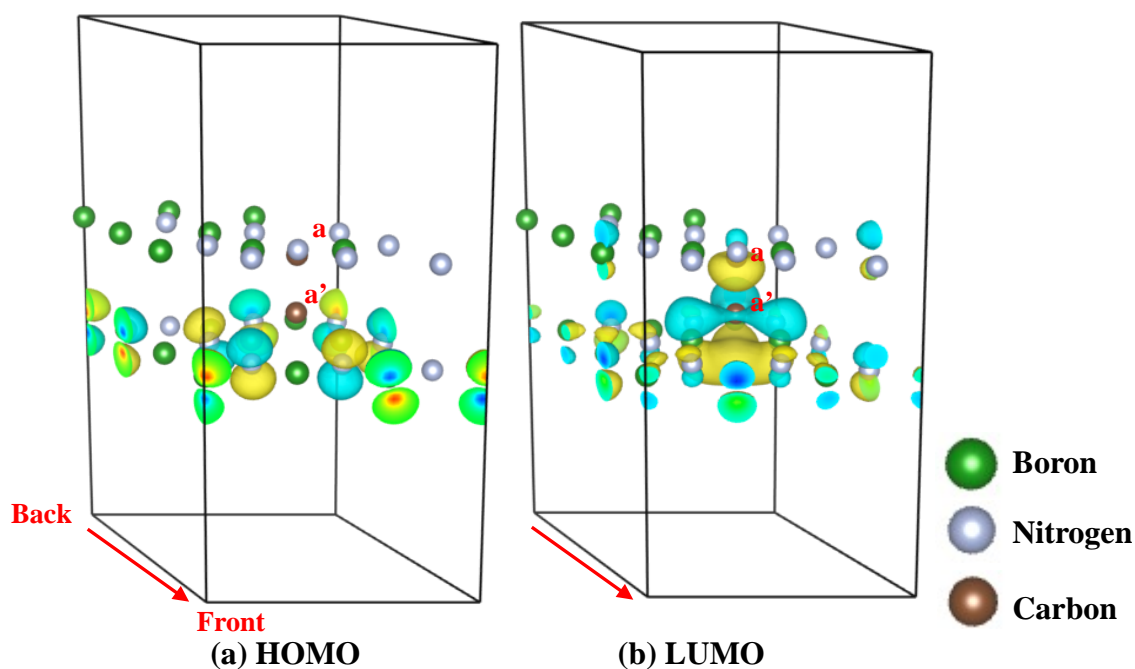


Figure 4.17 The atomic orbitals of 2C-i (a) HOMO and LUMO

4.3.3.3 Double-layered h-CBN, type (ii)

Figure 4.18 shows double-layered h-CBN structures of type (ii): (a) 2C-ii and (b) 6C-ii. All the C atoms are labeled in **Figure 4.18**. In 2C-ii structure, C atom “a” deviates from the top layer while the C atom “a’” is not. In 6C-ii structure, the C atoms “b”, “c”, “d” also deviate from the top layer, but the deviations are not so significant as that of C atom “a” in 2C-ii. The value of the deviation (C atom “a”) from the layer is 0.69 Å in 2C-ii. The C atoms “b”, “c”, “d” are all 0.10 Å in 6C-ii. The C atoms in different layers have large distances (more than 3 Å). It is difficult to consider that there is a chemical bond between layers. In addition, the interlayer distances of these two structures (2C-ii and 6C-ii) are coincide with each other with the value of 3.40 ± 0.02 Å.

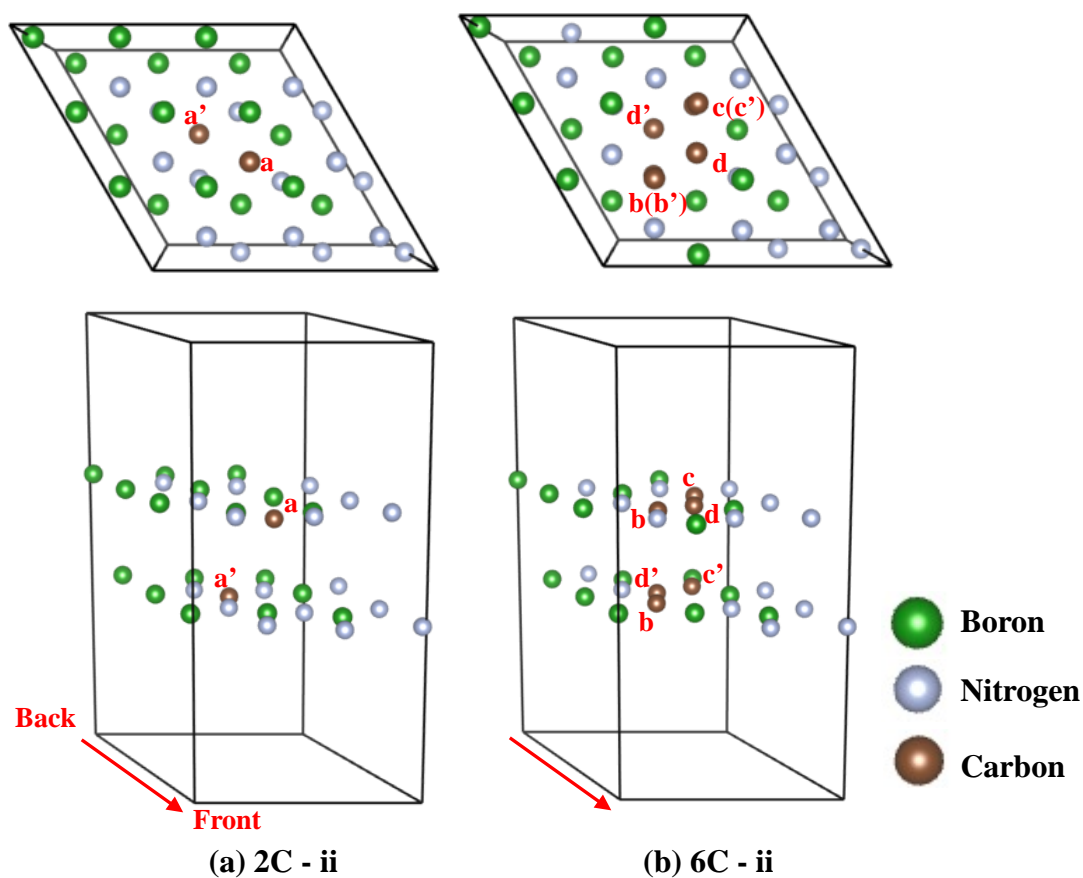


Figure 4.18 The optimized double-layered doping structures shown from the top view (first line) and side view (second line). (a) 2C - ii, (b) 6C - ii.

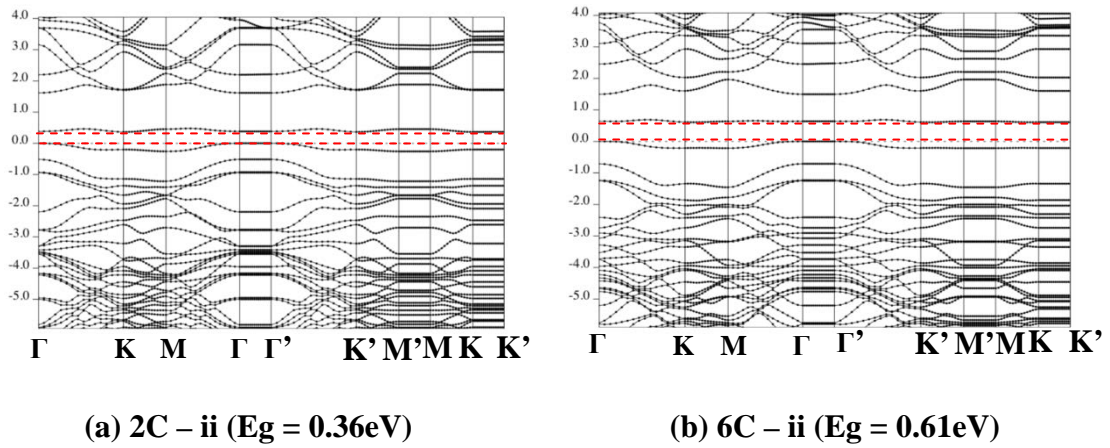


Figure 4. 19 The band structure of double doping structure (ii). The different band gaps of the 0.36eV and 0.61eV with different carbon content.

The band structures of 2C-ii and 6C-ii are shown in **Figure 4.19**, both of them show interesting results. The 2C-ii and 6C-ii have small band gaps with the value of 0.36eV and 0.61eV, respectively. The band gaps are much smaller than that of type (i) with the same carbon content (2C-i is 3.75eV, 6C-i is 3.25eV, discussed in section 4.3.3.2). Although the carbon content was increased from 2 to 6, the band gap increased, which is different from the general tendency of monolayers or type (i) double layers. Both of 2C-ii and 6C-ii are not metallic because neither of the two structures have the energy levels (HOMO or LUMO) crossing Fermi level. It means the same as type (i) structure, the free electrons from the two different metallic layers have paired.

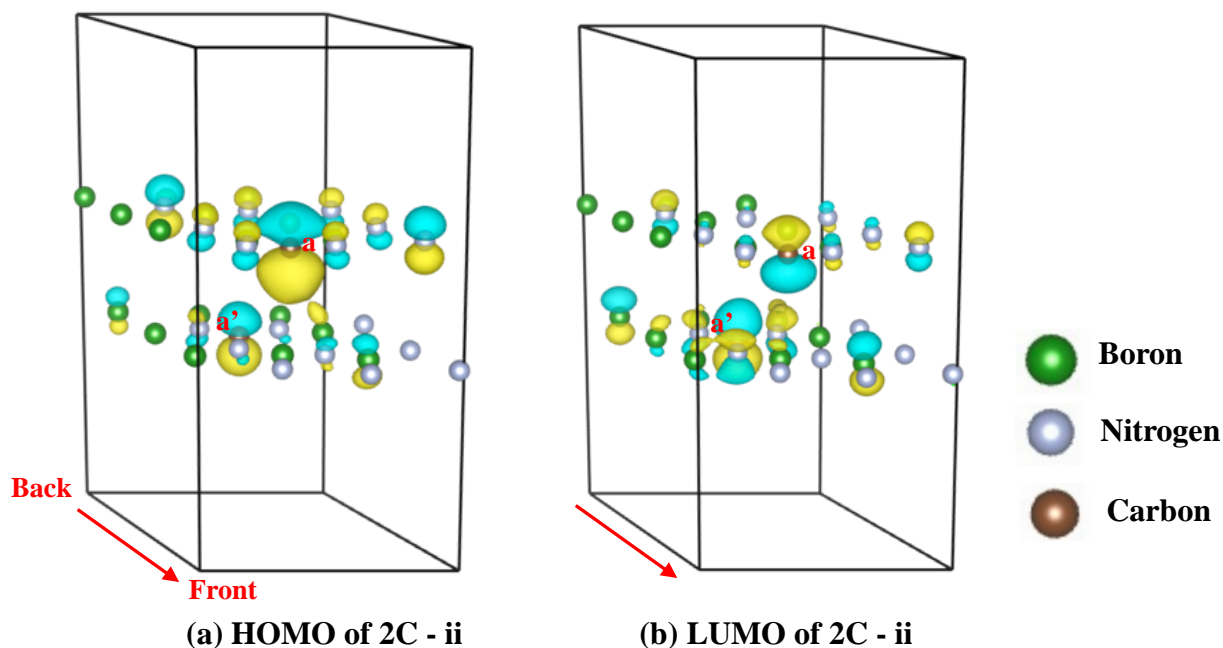


Figure 4.20 The HOMO and LUMO of 2C - ii

The HOMO and LUMO of 2C-ii and 6C-ii are shown in **Figure 4.20** and **Figure 4.21**, respectively. In 2C-ii structure, the HOMO and LUMO are mainly contributed by the C atoms **a**, **a'**. Both of C atoms of **a**, **a'** contribute to both of HOMO and LUMO, which means that the C atoms in types (ii) are active unlike those in type (i). They can be both electron donor and acceptor. In 6C-ii structure, the HOMO and LUMO are mainly contributed by the C atoms **b**, **b'**, **c**, **c'**. Similar to 2C-ii, the C atom of **b**, **b'**, **c**, **c'** all contributes to both HOMO and LUMO, which also means that the C atoms **b**, **b'**, **c**, **c'** are active and they can be both electron donors and acceptors. This mixed contribution of C atoms to both of HOMO and LUMO seems important as the mechanism of narrowing band gaps with low carbon content.

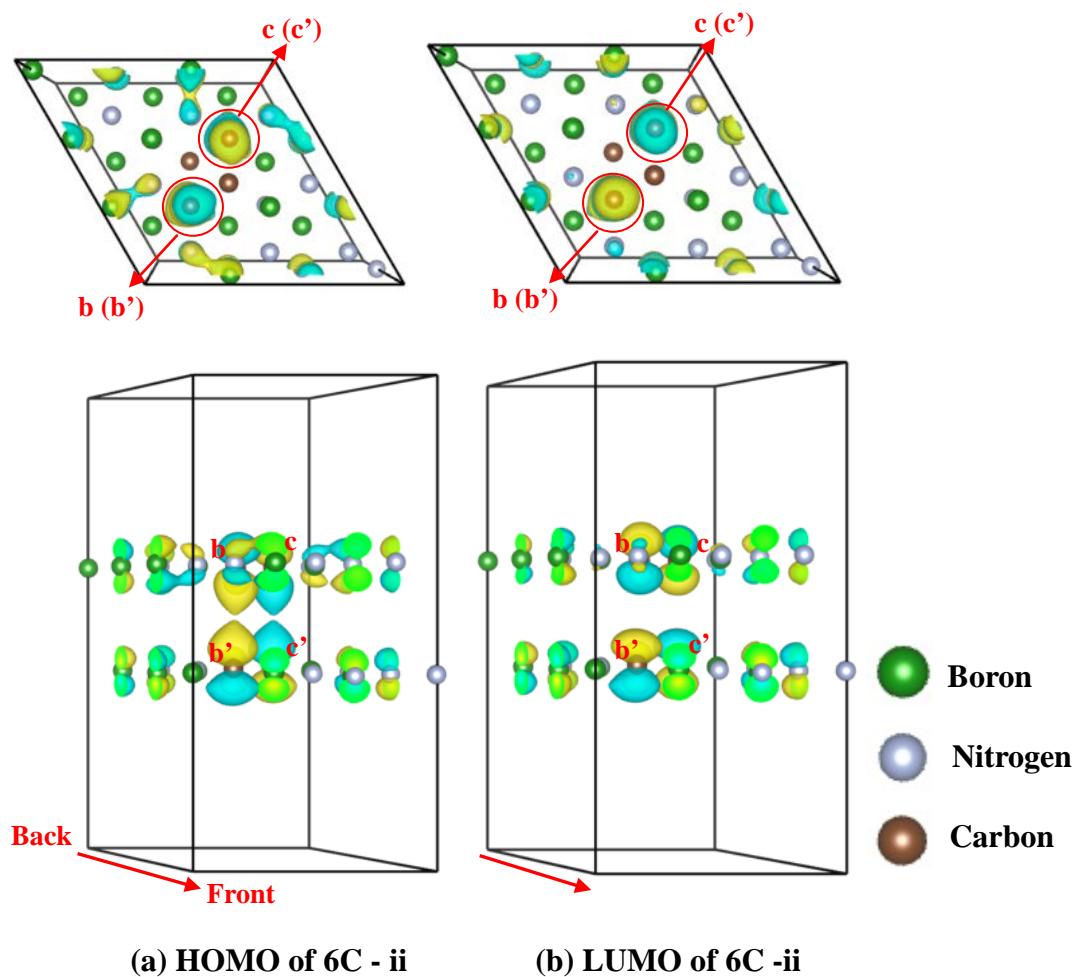


Figure 4.21 The HOMO and LUMO of 6C - ii

ELF were also used to analyze the electron distributions of type (ii) structure. **Figure 4.22** shows the ELF of 2C-ii while **Figure 4.23** shows the ELF of 6C-ii. In 2C-ii structure, around the C atoms **a'** in the bottom layer, the electron distribution is similar to that around the B atoms. The C atoms **a'** is bonded with neighboring N atoms by three σ bonds. There are no electrons located on the p_z -orbital of C atom **a'**, which means the new electron pair is not located on **a'**, C atom **a'** is an electron donor. Around C atom **a** in the top layer, besides the three σ bonds, a electron cloud localized on the p_z -orbital. It means that a new electron lone pair is located on **a**, and C atom **a**

is an electron acceptor. In other words, one electron is transferred from \mathbf{a}' in the bottom layer to \mathbf{a} in the top layer. This spontaneous electron transfer behavior proves that the 2C-ii is a kind of charge-transfer complex (CT complex), and the narrow band gap is one of the important features of the CT complex. [47-49]

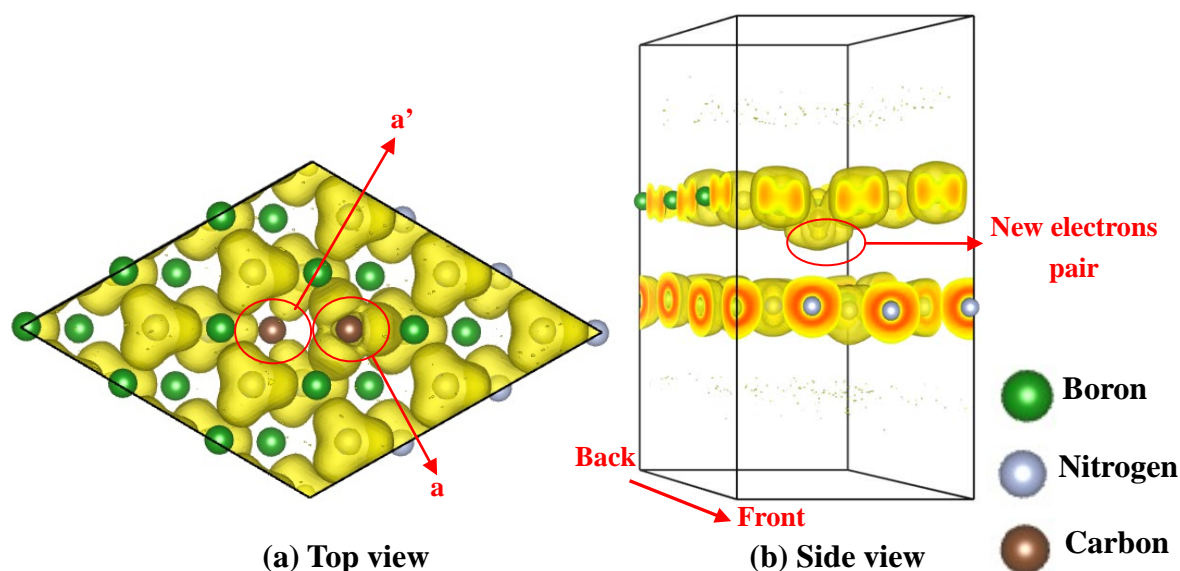


Figure 4.22 The electron localization function (ELF) distribution of 2C - ii.

Figure 4.23 exhibits ELF figure of 6C-ii structures. In 6C-ii, the shape of the electron distributions between C-C (**Figure 4.23(a)**) means that beside the σ bonds, C-C is also contributed from π -electron structures. The doped carbon atoms form two π -electron structure separately in different layers. From this ELF figure, it is hard to tell where the new electron pair is located and the direction of the electron transfer. In 6C-ii, the electrons around C atoms are delocalized. The new electron pair contributes to π -electron structures among the three carbons in the same layer. By the close analysis, it was found that the electron transfer was from the bottom layer to the top layer (N-rich layer to B-rich layer) and the amount was $0.32 e^-$ in this extended unit cell. This charge difference indicates that the spontaneous electron transfer

behavior still exists in 6C-ii structure, but it is weakened. It is consistent with the bandgap of 6C-ii larger than 2C-ii. Doping multiple (odd numbered) C atoms tend to form more stable electronic structures in their own layers than isolated C atoms do.

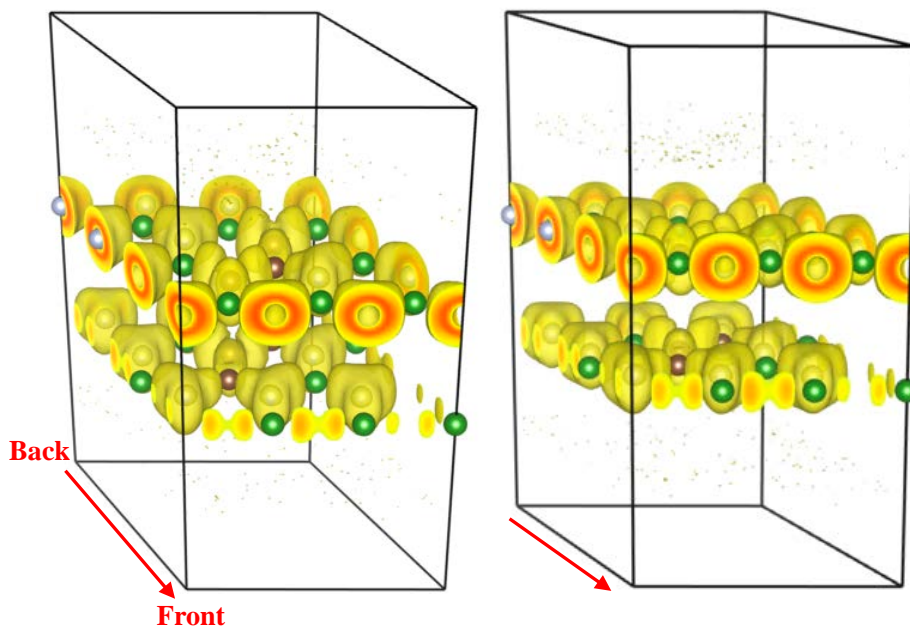
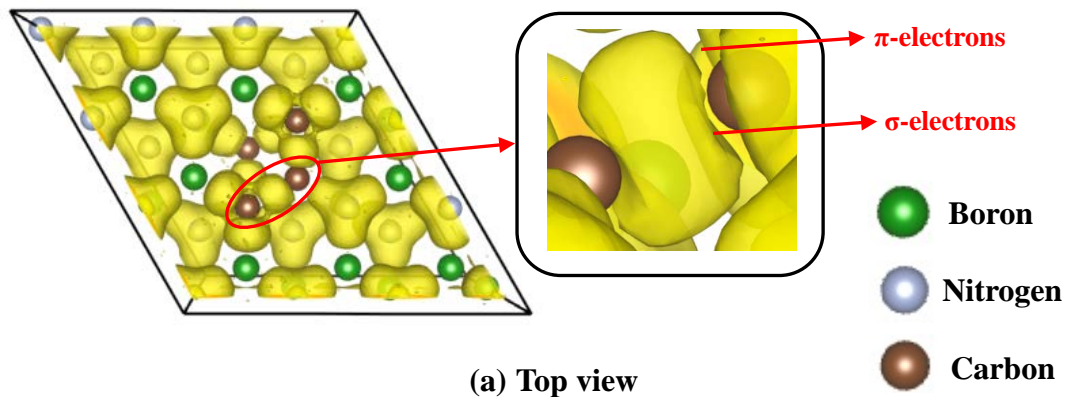


Figure 4.23 The electron localization functional (ELF) distribution of 2C - ii. In the bottom layer, the doping three carbon gathered more electron than the top layer.

4.3.3.4 Double-layered h-CBN, type (iii)

Figure 4.24 shows double-layered h-CBN structures of type (iii), 2C-iii. In the

same way as the type (i) and type (ii), the deviated atoms (C atoms and B atom) are labeled in **Figure 4.24**. In 2C-iii structure, C atom “a” deviates from the top layer while the C atom “a’ ” in the bottom layer does not. Unlike the other two types of h-CBN ((i) and (ii)), a B atom “b” deviated from the bottom layer. The C atom “a” and B atom “b” are getting close. The displacement of C atom “a” from the top layer is 0.82 Å and that of B atom “b” is 0.67 Å. The distance of the two displaced atoms “a” and “b” is 1.76Å. This small distance means they interact each other. In addition, the interlayer distance of the structure 2C-iii coincide with other types (i) and (ii) and pristine h-BN with the value of 3.40 ± 0.02 Å.

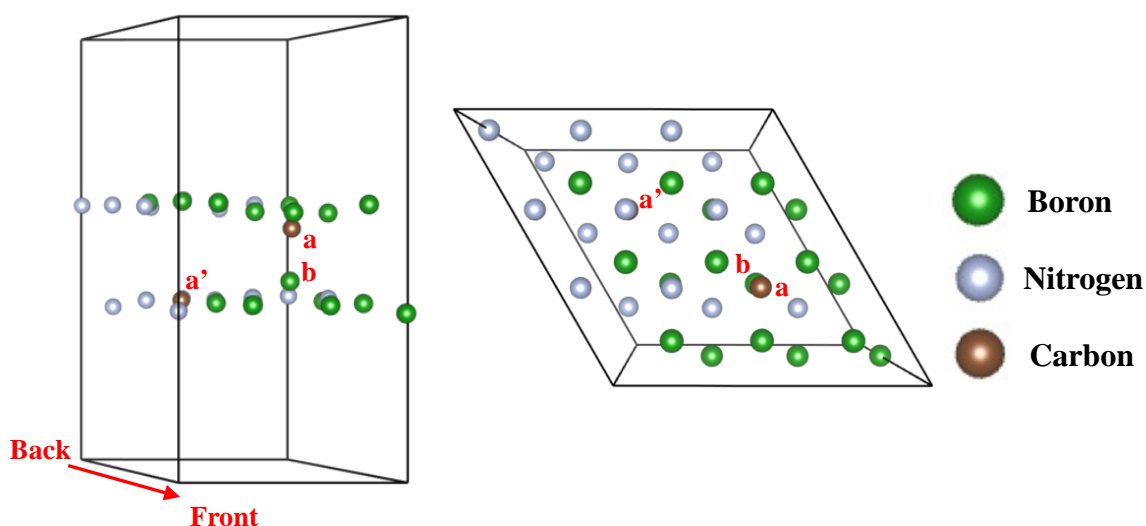


Figure 4.24 The optimized double-layered structure of 2C-iii shown from the side view and top view

The band structure of 2C-iii is shown in **Figure 4.25**. It shows a different band structure form the type (i) and (ii). In 2C-iii case, the band gap is indirect. The HOMO-band top is located at Γ -point while LUMO-band bottom is located at K-point. The value of the band gap is 2.69 eV. This band gap is much smaller than that of 2C-i

(3.75 eV, discussed in section 4.3.3.2), and much larger than that of 2C-ii (0.32 eV, discussed in section 4.3.3.3) with the same carbon content of 2C. In the band structure of 2C-iii, the HOMO crosses the Fermi level, which means that structure 2C-iii is metallic in the same way as “Phenalenyl” (Monolayer, discussed in section 4.3.2.6). Unpaired electrons exist in these structures. Based on the analysis of band structure, the electron transfer behavior does not seem to exist in 2C-iii. I will discuss it by using ELF figure in the following.

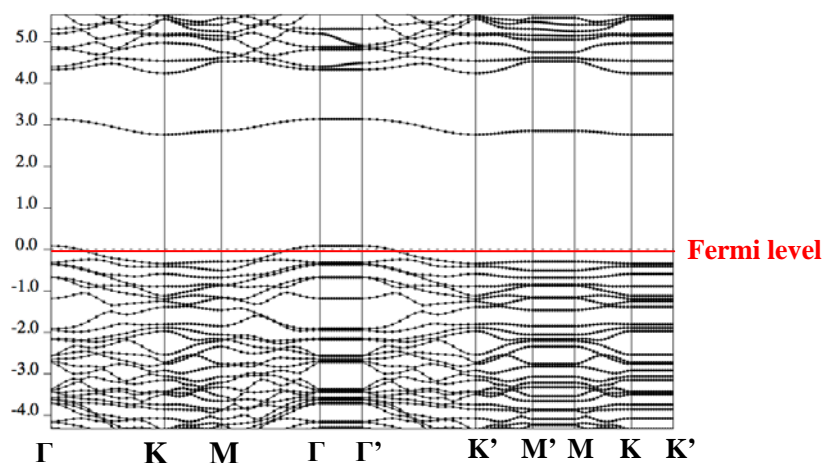


Figure 4.25 The band structure of double doping structure (iii), 2C-iii. HOMO crosses the Fermi level. The band gap is 2.69 eV.

The HOMO and LUMO are shown in **Figure 4.26**. In 2C-iii structure, HOMO is contributed by the N atoms adjacent to C atom “a”. The LUMO is contributed by the C atom “a” and two types of N atoms, those adjacent to C atom “a” and those around the displaced B atom “b”. The separated distribution of HOMO and LUMO indicates that interaction between two layers is weak. In the top layer, the C atom “a” neither contributes to the HOMO nor LUMO. Considering the deviation of the C atom “a”, this carbon has sp^3 configuration, which has deep levels.

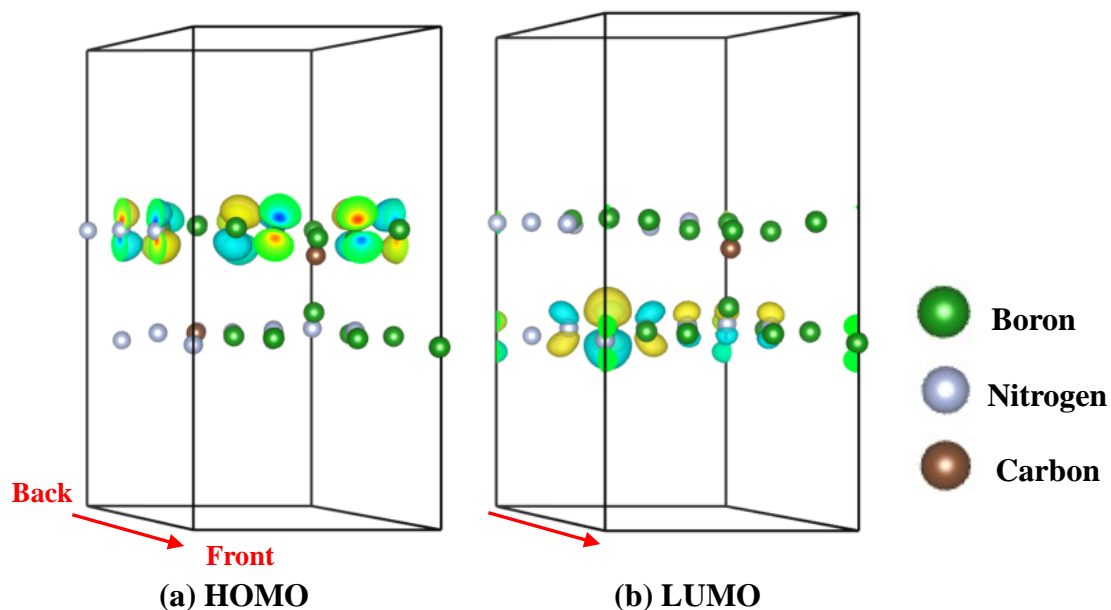


Figure 4.26 The HOMO and LUMO of 2C - iii

Figure 4.27 exhibits ELF figure of 2C-iii structures. In 2C-iii, the existence of the electron cloud between C atom “a” and B atom “b” means these two atoms directly bond together. Both of C atom “a” and B atom “b” exist in the 2C-iii with the stable sp^3 state. It is the reason of C atom “a” does not contribute to the HOMO or LUMO. The B atom “b”, as a new electron donor, forms covalent bond with C atom “a”. However C atom “a” in bottom layers(N-rich layer), a unpaired electron still located at C atom “a”, which makes C atom “a” more active than “a”. This is the reason of the metallic features. The interlayer charge transfer exist in 2C-iii, but the amount was $0.17 e^-$, which is much smaller than type (ii).

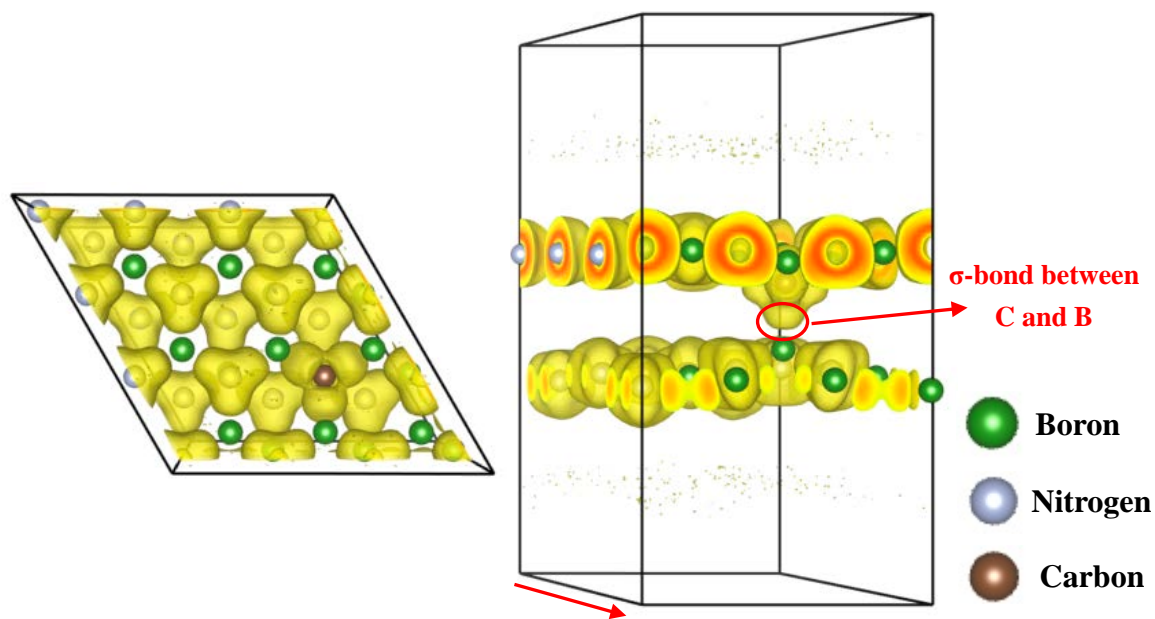


Figure 4.27 The electron localization functional (ELF) distribution of 2C - iii. σ -bond forms between C atom “a” and B atom “b”.

4.3.3.5 Double-layered even-number C h-CBN

I also calculated some of the even numbered double-layered h-CBN. Three structures can be categorized as type (iv).

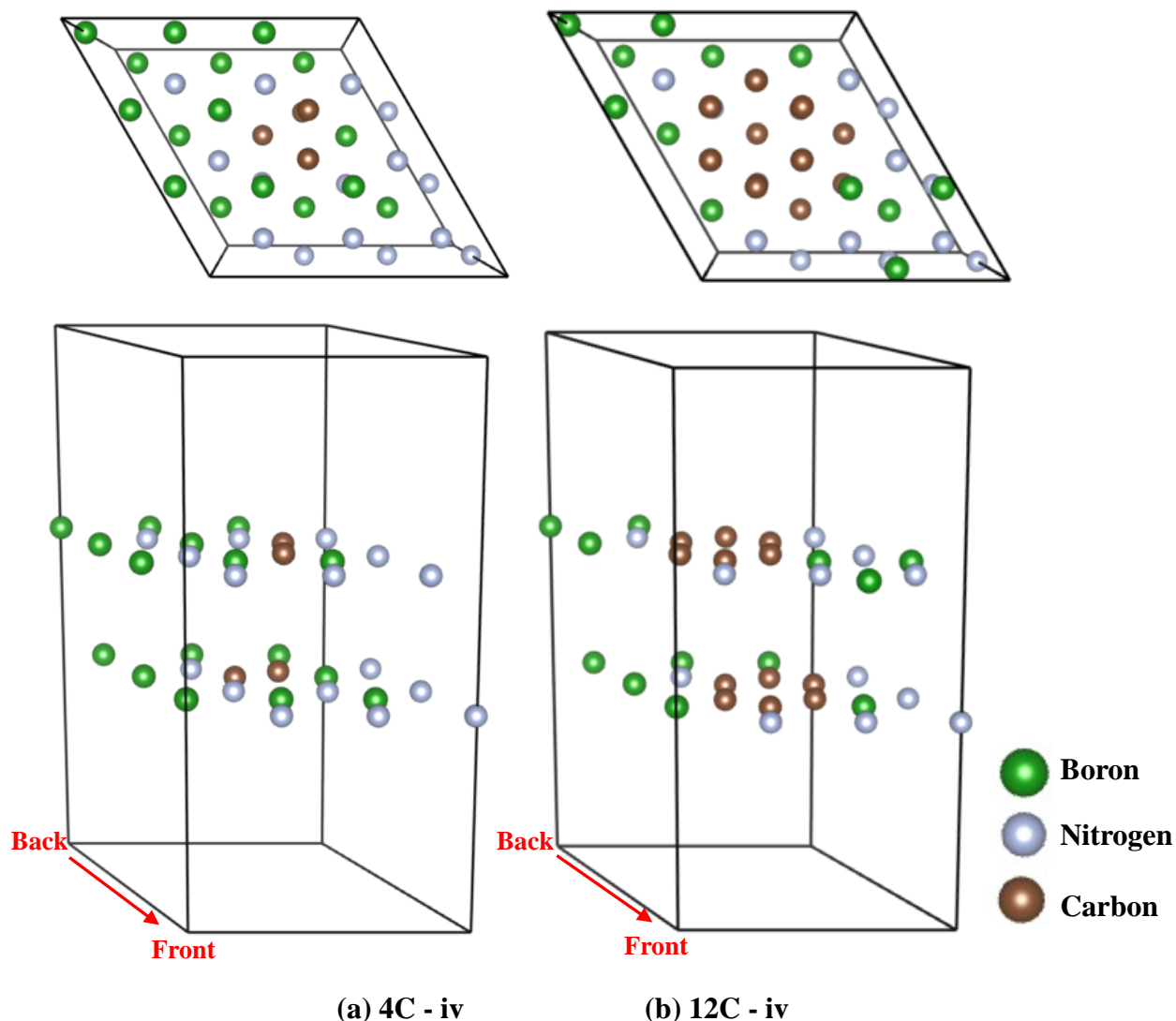


Figure 4.28 The optimized double-layered doping structures including the top view (first line) and side view (second line). (a) 4C - iv, (b) 12C - iv.

Figure 4.28 shows optimized structures of type (iv): 4C-iv, 12C-iv. the distance of the two layers was 3.4 Å without any changes in vertical direction from pure double-layered h-BN. The doped carbon atoms also did not show a significant position shift. Based on the optimized structures, the two layers are independent. In the band structures shown in **Figure 4.29**, the band gap was direct and located at

Γ -point. The band gap was similar to 2C (**Figure 4.4 (a)**) of mono-layered structure with the value of 3.09eV which means that the separately doped carbon atoms in different layers had no direct chemical interaction. It is noticed that all the band dispersion curves are made of almost parallel two curves. It means that two layers have small but not zero interactions.

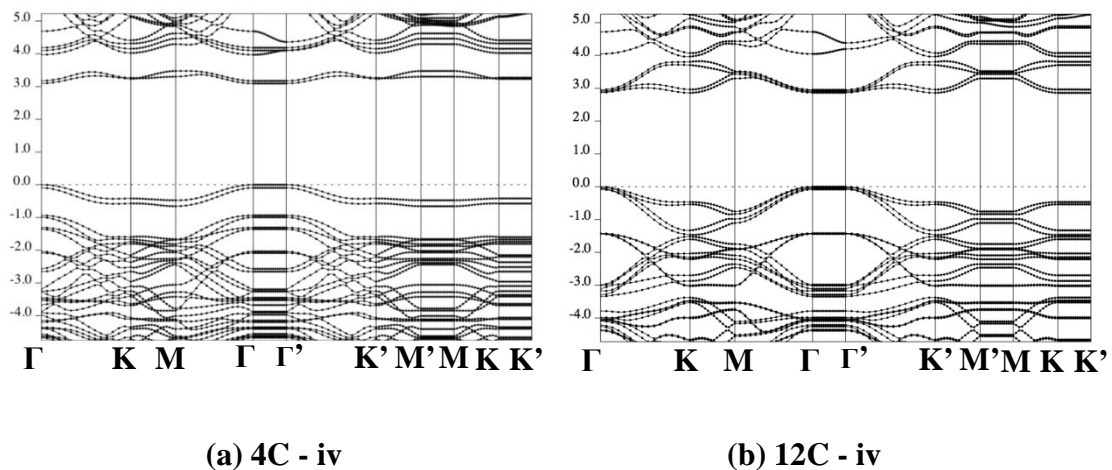


Figure 4.29 The band structure of double doping structure (iv). All of them had a similar band gaps to the mono-layered carbon doped structure.

4.3.3.6 Comparison with the experiments

Now I will discuss the comparison with the experiments. h-CBN can be synthesized by CVD or plasma CVD but the electronic structures are sensitive to the growth conditions [25]. In this Chapter, I found that the electronic structures are very sensitive to the geometry of the doping (C numbers, arrangements, etc.). It can account for the difficulty to control the electronic structures of the materials.

In the future, some methods will be found to synthesize h-CBN as designed in the atomic level, then it will open a way to variety of physical properties of this group of materials. I hope my work will stimulate further experiments on the electronic

structure of h-CBN system as well as their applications.

4.4 Conclusions

In conclusion, electronic structure calculations were carried out for the investigation of the effect of C doping to the electronic states and band structure of mono- and multi-layered h-BN by using generalized gradient approximation (GGA) of Perdew-Burke-Ernzerhof (PBE) functional by density functional theory (DFT) with plane wave and pseudopotentials. In mono-layered carbon doped structure, the band gap first decreased and saturated at around 3.00 eV with the number of dope atoms was increased from two to six. After the carbon content increased to make one “benzene ring”, the band gap decreased with the benzene ring number increasing. When the “benzene ring” number increased to five with 20 doped carbon atoms, the band gap decreased to 0.83eV which is very close to that of bulk silicon. This material has an advantage of having a direct band gap. The band dispersions of these materials are sufficiently large to be used as semiconductors. Another interesting finding is that the geometry of carbon arrangement greatly affects the band gap, just as in hydrocarbon molecules. For example, adding one “benzene ring” in connection to the pre-existing “benzene ring” to make “Naphthalene”, can achieve a smaller band gap than the separately existing “benzene ring” as “Biphenyl”. Odd number doping of carbon atoms lead to a metallic properties. One more boron replaced structure left one electron in conduction band which caused the LUMO crossing the fermi level. In contrast, one more boron replaced structure made one hole in valance band which caused the HOMO crossing the fermi level.

The odd numbers lead to a different type (n- and p- type) band structure,

which made me to consider the double layered doping structure. With a certain arrangement of the layers, the doping structures show narrow band gaps such as 0.37eV of 2C-ii structures. ELF figure proves that electron transfer happened between the two layers.

References

1. K. S. Novoselov, D. Jiang, F. Schedin, et al., Proc. Natl Acad. Sci. USA, **2005**, 102, 10451.
2. K. S. Novoselov, A. K. Geim, S. V. Morozov, et al., Science, **2004**, 306, 666.
3. Y. Zhang, J. P. Small, M. E. S. Amori, and P. Kim, Physical Review Letters, **2005**, 94, 176803.
4. C. Berger, Z. H. Song, T. B. Li, et al., J. Phys. Chem. B, **2004**, 108,19912.
5. K. S. Novoselov, A. K. Geim, S. V. Morosov, et al, Nature, **2005**, 438, 197.
6. Y. Zhang, Y. W. Tan, H. L. Stormer, et al., Nature, **2005**, 438, 201.
7. K. S. Novoselov, E. Mccann, S. V. Morosov, et al, Nature Phys., **2006**, 2, 177.
8. Y. Zhang et al., Appl. Phys. Lett., **2006**, 86, 073104.
9. N. M. Peres et al., Physical Review B, **2006**, 73, 125411.
10. K. Wakabayashi, Physical Review B, **2011**, 64, 125428.
11. K. Nakada, M. Fujita, G. Dresselhaus, and M. S. Dresselhau, Physical Review B, **1996**, 54, 17954.
12. J. Scott Bunch, Arend M. van der Zande, Scott S. Verbridge, et al, Nano Lett., **2005**, 315, 490.
13. K. Watanabe, T. Taniguchi, H. Kanda, Nature Materials, **2004**, 3, 404-409.
14. Y. Kubota, K.i Watanabe, O. Tsuda, T. Taniguchi, Science, **2007**, 317, 932.
15. D. Golberg, Y. Bando, Y. Huang, T.i Terao, M. Mitome, C. C. Tang, and C.i Zhi, ACS Nano, **2010**, 4(6), 2979–2993.
16. D. P., J. C. Meyer, C. O. Girit, and A.. Zettl, Appl. Phys. Lett., **2008**, 92, 133107.

17. C. Lee, Q. Y. Li, W. Kalb, X. Z. Liu, H. Berger, R. W. Carpick, James Hone, *Science*, **2010**, 328, 76.
18. G. Giovannetti, P. A. Khomyakov, G. Brocks, P. J. Kelly, and J. van den Brink, *Physical Review B*, **2007**, 76, 073103.
19. C. Y Zhi, Y. Bando, C. C. Tang, H. Kuwahara, D. Golberg, *Adv. Mater.*, **2009**, 21, 2889.
20. J. C. Meyer, A. Chuvilin, G. Algara-Siller, J. Biskupek, and U. Kaiser, *Nano Letters*, **2009**, 9, 2683.
21. A. Nag, K. Raidongia, K. P. S. S. Hembram, R. Datta, U. V. Waghmare, and C. N. R. Rao, *ACS Nano*, **2010**, 4, 1539.
22. A. Nagashima, N. Tejima, Y. Gamou, T. Kawai, and C. Oshima, *Physical Review Letters*, **1995**, 75, 3918.
23. M. Corso, W. Auwärter, M. Muntwiler, A. Tamai, T. Greber, and J. Osterwalder, *Science*, **2004**, 303, 217.
24. W. Auwärter, H. U. Suter, H. Sachdev, and T. Greber, *Chem. Mater.*, **2004**, 16, 343.
25. L. Ci, L. Song, C. H. Jin, Deep Jariwala, et al, *Nature Materials*, **2010**, 9, 430.
26. W. L. Wang , X. D. Bai , K. H. Liu , Z. Xu , D. Golberg , Y. Bando, and E. G. Wang, *J. Am. Chem. Soc.*, **2006**, 128, 6530.
27. Q. Tang, Z. Zhou, and Z. F. Chen, *J. Phys. Chem. C*, **2011**, 115, 18531.
28. X. B. Wang, C. Y. Zhi, L. Li, et al, *Advanced Materials*, **2011**, 23, 4072.
29. P. P. Shinde and V. Kumar, *Physical Review B*, **2011**, 84, 125401.
30. H. Park, A. Wadehra, J. W. Wilkins, and A. H. Castro Neto, *Appl. Phys. Lett.*, **2012**, 100, 253115..

31. Q. B. Wang, C.i Zhou, J. Wu, et al, Computational Materials Science, **2015**, 102, 196.
32. M. Etienne, A. Quach, D. Grosso, L. Nicole, C. Sanchez, and A. Walcarius, Chem. Mater., **2007**, 19, 844.
33. H. J. Monkhorst and J. D. Pack, Physical Review B, **1976**, 13, 5188.
34. E. Knittle, R. M. Wentzcovitch, R. Jeanloz, and M. L. Cohen, Nature, **1989**, 337, 349.
35. D. R. Cooper, B. D'Anjou, N. Ghattamaneni, B. at el, ISRN Condensed Matter Physics (International Scholarly Research Network), **2012**, 1–56. doi: 10.5402/2012/501686. Retrieved February 2015.
36. G. Trinquier, J. Am. Chem. Soc., **1990**, 112 , 2130.
37. V. L. Solozhenko, G. Will, F. Elf, Solid State Communications, **1995**, 96, 1.
38. W. Paszkowicz, J. B Pelka, M. Knapp, T. Szyszko, S. Podsiadlo, Applied Physics A: Materials Science & Processing, **2002**, 75, 431.
39. A. Marini, P. Garcia-Gonzalez, A. Rubio, Physical Review Letters, **2006**, 96, 136404.
40. G. Kern, G. Kresse, J. Hafner, Physical Review B, **1999**, 59, 8551.
41. R. Pease, Acta Crystallographica, **1952**, 5, 356-361.
42. Y. Shi, C. Hamsen, X. Jia, K. K. Kim, A. Reina, M. Hofmann, A. L. Hsu, K. Zhang, H. Li, Z. Y. Juang, M. S. Dresselhaus, L. J. Li, J. Kong, Nano Letters, **2010**, 10, 4134.
43. J. D. Bernal, Proceedings of the Royal Society of London. Series A, **1924**, 106, 749.
44. D. Chung, Journal of Materials Science, **2002**, 37, 1475.

45. Y. Baskin, L. Meyer, *Physical Review*, **1955**, 100, 544.
46. H. Sachdev, R. Haubner, H. Nöth, B. Lux, *Diamond and Related Materials*, **1997**, 6, 286.
47. S. Horiuchi, K. Kobayashi, R. Kumai, N. Minami, F. Kagawa, and Y. Tokura, *Nature Communications*, **2015**, 6, 7469.
48. V. Murugesan, M. Saravanabhavan, and M. Sekar, *Journal of Molecular Structure*, **2015**, 1084, 95.
49. G. Kim, Sang-Hyup Lee, Wonyong Choi, *Applied Catalysis B: Environmental*, **2015**, 162, 463.

Chapter 5. Overall summaries and prospect

This PhD thesis mainly consists of two parts. One is the experimental part of novel DLC synthesis with nanostructured components originating molecules (Chapter 2 and 3). The other is the theoretical part of h-CBN design with molecule-resembling carbon arrangements (Chapter 4).

In Chapter 2, I co-deposited CuPc and PTCDA molecules with DLC film by using a newly-developed PACVD equipment. Both of the CuPc molecules and PTCDA molecules were incorporated into the film by thermal evaporation. In the case of CuPc, the co-deposited film showed an optical absorption profile similar to the pristine molecular film, but still, minor changes were observed. However, in PTCDA case, a substantial destruction of the π -electron structure has been observed in the optical absorption spectra and Raman spectra. Further analysis based on the Raman spectrum, it was concluded that the carboxylic dianhydride (C-O-C) moiety remains intact in PTCDA-DLC co-deposited film.

In the Chapter 3, the PACVD with molecular co-deposition was used for synthesizing the mixture of DLC and C₆₀. To my surprise, the grown film changed the color after exposure to the air, and showed angle depend iridescence, which can be tuned from blue to pink by changing the thickness of the film. It was found that the appearance of the iridescence was due to the reaction between C₆₀-DLC co-deposited film and H₂O vapor. By using SEM and TEM, I found that nanoscale grain structures in the film emerged like popcorn. The infrared absorption and Raman spectra showed that C₆₀ was decomposed and produced sp² carbon clusters in the

DLC. A strong iridescence appeared from the high refractive index (3.6), relatively low absorption and internal scattering caused by sub-wavelength structures of the material. I conducted detailed spectroscopic examination after D₂O exposure and quantum chemical calculation of model systems to understand the reaction. It was concluded that this phenomenon occurs from the cage breaking of C₆₀, initially with extra chemical bonds with surrounding DLC and followed by the reaction with H₂O molecules. The present result shows the possibility of nano-structured carbons as optical functional materials. It is also proposed that the inclusion of reaction centers (in this case C₆₀) with a vapor in solids for the synthesis of new materials.

Chapter 4 shows the theoretical work on h-CBN design with “molecular” arrangement of carbon atoms. All the calculations were carried out for the investigation of the effect of C doping to the electronic state and band structure of multi-layered h-BN. In mono-layered carbon doped structure, the band gap decreased with the carbon content increasing. The h-CBN with the carbon content of 20/32 achieved a narrow band gap of 0.83eV, which is very close to that of bulk silicon. This material has an advantage of having a direct band gap. The band dispersions of these materials are sufficiently large to be used as semiconductors. Odd number doping of carbon atoms lead to a metallic properties. One more boron replaced structure makes a n-type metal, while one more boron replaced structure makes a p-type metal.

The odd numbers lead to a different type (n- and p- type) band structure, which made me to consider the double layered doping structure. With a certain arrangement of the layers, the doping structures show narrow band gaps as low as 0.37eV. ELF figure proves that electron transfer happened between the two layers.

These results, which were not reported previously especially on double layers, point out that there are rich materials chemistry in h-CBN systems.

As the future prospect of the materials based on carbon, this thesis has given a tiny part of the huge variety of chemistry and physics in them. Just pursuing an idea of incorporating “molecules” in DLC has made a new materials of carbon nanopopcorn which was created by unexpected reaction with water vapor in atmosphere. Interaction of layers in h-CBN also provides rich features from charge transfer complex formation to sp^3 interlayer bonding, as well as van der Waals interaction of tunable bandgap layer. I hope that we human will be able to discover various useful features and properties of carbon based materials and find the new chemistries to synthesize atomically designed structures, then improve the universe.